Measurement of Fragmentation Functions in DIS at HERA

Jane Talyth Bromley

Department of Physics & Astronomy
University of Glasgow
Glasgow

Thesis submitted for the degree of
Doctor of Philosophy

September 1998

Abstract

The production of charged particles produced in Deep Inelastic Scattering (DIS) events at HERA has been studied using the ZEUS detector. Measurements have been made of the fragmentation variables x_p and $\ln\left(\frac{1}{x_p}\right)$ in the current region of the Breit frame of the interaction in the ranges $10 < Q^2 < 5120$ GeV^2 and $0.6 \; 10^{-3} < x < 0.25$. Evidence is found for scaling violations in the scaled momentum, x_p, as a function of Q^2, and the data are shown to be well described by Next-to-Leading order calculations. The description of the $\ln\left(\frac{1}{x_p}\right)$ distributions by the Modified Leading Log Approximation (MLLA) is studied, and its predictions for their evolution with energy are investigated. The data are compared with results from e^+e^- annihilation experiments.

Preface

Studies of scaling violations in structure functions in deep inelastic scattering have helped to establish quantum chromodynamics (QCD) as the theory of strong interactions and have led to measurements of the strong coupling constant, α_s. Similar scaling violations are predicted in the fragmentation functions of quarks and gluons [1]. The fragmentation function $D^h(x_p, Q^2)$ for a parton represents the probability that it fragments to form a hadron h carrying a fraction x_p of the parton's momentum. As with structure functions, the fragmentation function cannot be calculated in perturbative QCD but can be evolved as a function of the appropriate energy scale. In hadroproduction experiments the final-state hadrons originate from the fragmentation of the initial quarks and gluons. QCD radiation varies logarithmically with the energy scale of the interaction, due to the increase in the available phase space with increasing energy and the running of α_s. These effects lead to variations in the scaled momentum spectra of the final-state hadrons as a function of the energy scale.

Studies of the scaled momentum spectra, $x_p = 2p/\sqrt{s}$, of charged final-state hadrons, where p is the momentum of the hadron and $\sqrt{s}$ is the centre-of-mass energy, have been performed by experiments at LEP [2, 3, 4]. Measurements made at LEP were combined with lower energy data from PETRA to show scaling violations in the single particle density, $\frac{1}{\sigma_{tot}} \frac{d\sigma}{dx_p}$ (where σ_{tot} is the total cross-section for the interaction), as a function of $\sqrt{s}$. A value for α_s was determined by fitting these data. By studying the final state in neutral current deep inelastic scattering (DIS) interactions at HERA, fragmentation functions can be measured at different energy scales in a single experiment. Also, HERA offers a unique ability to scan through the moderate and small Q^2 range in order to shed light onto the transition between hard and soft

phenomena.

In DIS the single particle density is a convolution of a parton density (f) with the hard scattering cross-section ($\hat{\sigma}$) and a fragmentation function ($\mathcal{D}$): $\sigma = f \otimes \hat{\sigma} \otimes \mathcal{D}$. The strong coupling constant enters through each of these components. The aim of the study undertaken for this thesis has been to measure fragmentation functions in the current region of the Breit frame in DIS and to compare the results with those from the e^+e^- annihilation experiments. The feasibility of using a HERA measurement of scaling violations in fragmentation functions to extract a value of α_s has been investigated. Also, the properties of quark fragmentation at low momentum have been tested via the measurement of $\ln\left(\frac{1}{x_p}\right)$ and the mean charged multiplicity. These distributions are expected to be sensitive to the phenomenon of QCD coherence. The structure of the thesis is described below.

In chapter 1 an overview of the theoretical context of HERA and e^+e^- measurements is given. An introduction is given to the properties of the Breit frame of reference.

In chapter 2 the operation of the HERA accelerator and the ZEUS detector are discussed, with particular emphasis on the detector components pertinent to the analysis. Chapter 3 contains a description of an algorithm designed to investigate the calibration of the ZEUS Central Tracking Detector (CTD), one of the most important components for this analysis. Calibration results are presented and compared with those from other methods.

The kinematic quantities employed to characterize DIS interactions are introduced in chapter 4 and an account is given of the methods by which they are reconstructed experimentally. The important backgrounds to the DIS process are described along with the event selection criteria by which they are excluded from the data. The results of an acceptance study of the kinematic regions covered by the analysis are shown.

The use of Monte Carlo models to simulate DIS events is discussed in chapter 5. A summary is given of the Monte Carlo models used in this analysis.

The reconstruction of the transformation to the Breit frame and of the fragmentation variables is reviewed in chapter 6. The factors which limit the precision of measurement of the fragmentation variables are discussed and the resolutions of the variables are determined.

The raw data distributions are presented in chapter 7. A description is provided of the technique by which they are corrected for acceptance and detector effects and the corrected data distributions are shown. The main sources of systematic uncertainty are investigated.

In chapter 8 the corrected data are compared with theoretical predictions and with results from e^+e^- annihilation experiments. The conclusions are summarised in chapter 9. Results from the analysis described in this thesis have been published [5], and have been presented in preliminary form at the Chicago DIS97 conference; the conference write-up is included as an appendix.

Acknowledgements

I would like firstly to extend my deeply heartful thanks to Drs Doyle and Brook, without whom this PhD would have been immeasurably more difficult. Tony has been consistently enthusiastic against the odds and has never failed with advice, encouragement or explanation. Nick has been a pleasure to work with - I couldn't have asked for better - and a complete star. Both of them have been endlessly patient in answering the same questions over and over again and rewarding to work with. I only hope I'm so lucky with future colleagues.

I am very grateful to the theorists whose work has contributed to this thesis, Dirk Graudenz and Janko Binnewies; Dirk in particular has answered numerous questions and cries for help.

To the people I've shared offices with over the years - Allan, Martin, Esther, Rob, Laurel, Neil, Gavin & Sung-Won: it's been fun. Thankyou for the jokes, for the help, and for putting up with my occasional grumpiness. Thanks also to Ian for, at the end,

reminding me what the point was.

There are many people in the ZEUS Collaboration to whom I'm indebted for help and small kindnesses over the years. I'd particularly like to mention the members of the Jets and High E_T working group, and also John Lane and Norman McCubbin for their contributions to my understanding of the CTD.

Many thanks to the people in Glasgow who've left me with so many splendid memories, especially Esther, Martin, Drew & Jacqui, to Catherine MacIntyre, and a special mention to Richard. Similarly, a big thankyou to all those who added so much to my quality of life in Hamburg: the desy women (Molly, Kirstee, Vicki and Rachel), Ben, the Bleicherstrasse crowd, and all the folk from ZEUS, H1, HERMES and outside DESY (too many to name) who made it so enjoyable.

Thanks to the friends - particularly Michele and Jason - who have put in outstanding support by email and phone and visits and by not being particle physicists. It kept me going when I needed it, and was equally as welcome when I didn't.

And more thanks than I can say to my family, who have always been there for me.

Thesis-writing tends to induce tunnel-vision, so there are bound to be people I would like to thank who I have forgotten to name. Thankyou, whoever you are.

Contents

vii

List of Figures

List of Tables

Chapter 1

Theory

1.1 Fundamental Forces

The study of high energy physics is motivated by the drive to understand the fundamental nature of matter and the laws governing its behaviour. The present understanding of these fundamental building blocks is built on a theoretical framework where all matter is made up of elementary, indivisible, particles - the quarks and leptons. Their interactions are ruled by four fundamental forces: the gravitational, electromagnetic, weak and strong forces. The operation of the forces is modelled by theories based on the interchange of force-carrying particles, known as bosons. A general overview of the present understanding of the fundamental forces and the fashion in which they fit together within the Standard Model of particle physics can be found in several textbooks (e.g. [6]).

Everything with mass or energy is subject to the gravitational force, but it is too weak a force to have observable effects in high energy interactions.

Electromagnetism, which affects anything with an electric charge, was the first fundamental force for which a complete theory was formulated. The theory of quantum electrodynamics (QED) is a quantum field theory which describes electromagnetic interactions as an exchange of photons, γ, between the interacting charged particles. The probability of photon exchange is governed by the coupling constant for QED, α. In order to absorb perturbative corrections to QED vertices and loops in the propagation

of particles, the coupling constant is allowed to run, so that its value depends on the energy of the interaction. QED is not exactly soluble: calculations rely on perturbative expansions in terms of α. However, the value for α is sufficiently small that reasonable accuracy can be obtained with only a few terms of the expansion.

The first observed weak interactions were those of nuclear β-decay, where the decay of bound nucleons gives sufficient energy to create leptons, for instance

$$p \rightarrow n + e^+ + \nu_e \qquad \text{or} \qquad n \rightarrow p + e^- + \bar{\nu}_e$$

and the reverse processes. Weak interactions take place via the exchange of a $W^\pm$ (as in the above reactions) or Z^0 boson. The interactions were observed to take place only over very short ranges - hence the name of the weak force - this was later shown to be a result of the large masses of the exchanged bosons which suppress the operation of the force. More recently the electroweak theory was formulated [7, 8, 9], which unifies the electromagnetic and weak forces via a single coupling constant α_W.

The subject of this thesis is the study of the strong force which binds nucleons together to form nuclei, and governs the interactions of the consituents of the nucleons, the quarks. The existence of quarks as the constituents of hadrons was proposed in the early 1960s by Gell-Mann in order to describe the groupings observed in baryon and meson resonances. At that time the model consisted of only 3 quarks: up, down and strange. The discovery of the Ω^-, Δ^-, and Δ^{++}, each composed of three like quarks with spin $\frac{1}{2}$, whilst supporting the general structure of the theory appeared to violate Fermi statistics. An additional degree of freedom was suggested - known as colour - with three possible values: red, blue or green. Hadrons would then be composed from colourless combinations of quarks and the Pauli principle would be unassailed. Only particles which possess this colour charge are affected by the strong force. Quantum chromodynamics (QCD) is the formal gauge theory of the strong interaction. The force is mediated by coloured gluons. In a similar way to QED, calculations are not exactly soluble and rely on perturbative techniques in terms of the coupling constant, α_s.

1.2   The QCD description of Deep Inelastic Scattering

A history of the development of QCD with support from deep inelastic scattering (DIS) results can be found in, for instance, reference [10]. The Quark Parton Model (QPM) pictures the proton as three non-interacting point-like valence quarks (uud) surrounded by a sea of $u\bar{u}$, $d\bar{d}$, $s\bar{s}$ pairs, and assumes that any interaction - such as an electron scattering off one of the quarks - takes place on a time-scale much shorter than that with which interactions between individual quarks take place. This ensures that the partons behave like free particles during a collision. Each parton i carries a momentum fraction x_i of the proton's momentum and is assumed to be massless. This picture of neutral current deep inelastic scattering (NC DIS) where an electron interacts with a parton inside the proton via exchange of a virtual boson with no electric charge is illustrated in figure 1.1.
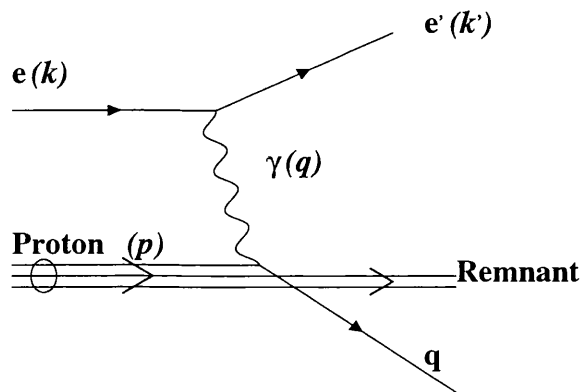
Figure 1.1: QPM description of a DIS event

If the four-momenta of the incoming positron, incoming proton, exchanged photon and outgoing positron are denoted by k, p, q and k' respectively, then DIS interactions can be characterised using the Lorentz scalars Q^2, x and y, where

- $Q^2 \equiv -q^2 = -(k - k')^2$, is the negative square of the four-momentum carried by the exchanged boson;

- $x = -q^2/2p.q$, is the Bjorken scaling variable, equivalent to the fraction of the proton's momentum carried by the struck quark-parton; and

- $y = p.q/p.k$, represents the fraction of the electron's energy transferred to the proton in the proton's rest frame.

DIS events have been detected by ZEUS with values of Q^2 ranging up to $Q^2 \sim 4 \times 10^4$ GeV^2 and with values of x between $\sim 10^{-5}$ and 0.7. In principle the exchanged boson could be a γ or a Z^0 or, in charged current DIS, a $W^{\pm}$. However, the $W^{\pm}$ and Z^0 bosons are suppressed because of their large masses so that, for instance, Z^0 exchange represents a 1% contribution to the cross-section for NC DIS at $Q^2 \approx 1000$ GeV^2. Thus, within the range of energies accessed in the analysis described in this thesis, only photon exchange is considered significant.

The differential cross-section for DIS can be expressed in terms of two[1] dimensionless structure functions, F_2 and F_L, as

$$\frac{d^2\sigma}{dQ^2 dx} = \frac{2\pi\alpha^2}{xQ^4} \left\{ [1 + (1-y)^2]F_2(x, Q^2) - y^2 F_L(x, Q^2) \right\}$$

In general, the $1/Q^4$ dependence means that the largest cross-section at HERA is for the lowest Q^2 interactions. F_L is the structure function for the case where the mediating photon is longitudinally polarised. The structure function F_2 can be interpreted in terms of the quark and antiquark densities q_i and $\bar{q}_i$ and their charges e_i:

$$F_2(x, Q^2) = x \sum_i e_i^2 (q(x, Q^2) + \bar{q}(x, Q^2))$$

over all quark flavours i. Clearly, if the QPM were an accurate picture of the interior of the proton, then $\int_0^1 F_2(x, Q^2) \frac{dx}{x} = 1$.

However, measurements of F_2 have shown that quarks do not account for all of the proton's momentum. The remaining momentum is ascribed to the charge-neutral, spin 1, coloured particles called gluons. These gluons are the mediating bosons of QCD. The QCD-improved QPM then portrays the proton as a composite particle containing the 3 valence quarks surrounded by a multitude of gluons interacting with the quarks and with each other. The gluons fluctuate to produce $q\bar{q}$ pairs of all flavours, known as sea-quarks. The largest contributions to the sea are from $u\bar{u}$, $d\bar{d}$ and $s\bar{s}$, although the strange contribution is suppressed by a factor of ~ 0.2 relative to the u or d contributions due to the larger mass of the s quarks.

---

[1]since for Q^2 values $\ll m_Z^2$ the parity violating structure function xF_3 is negligible.
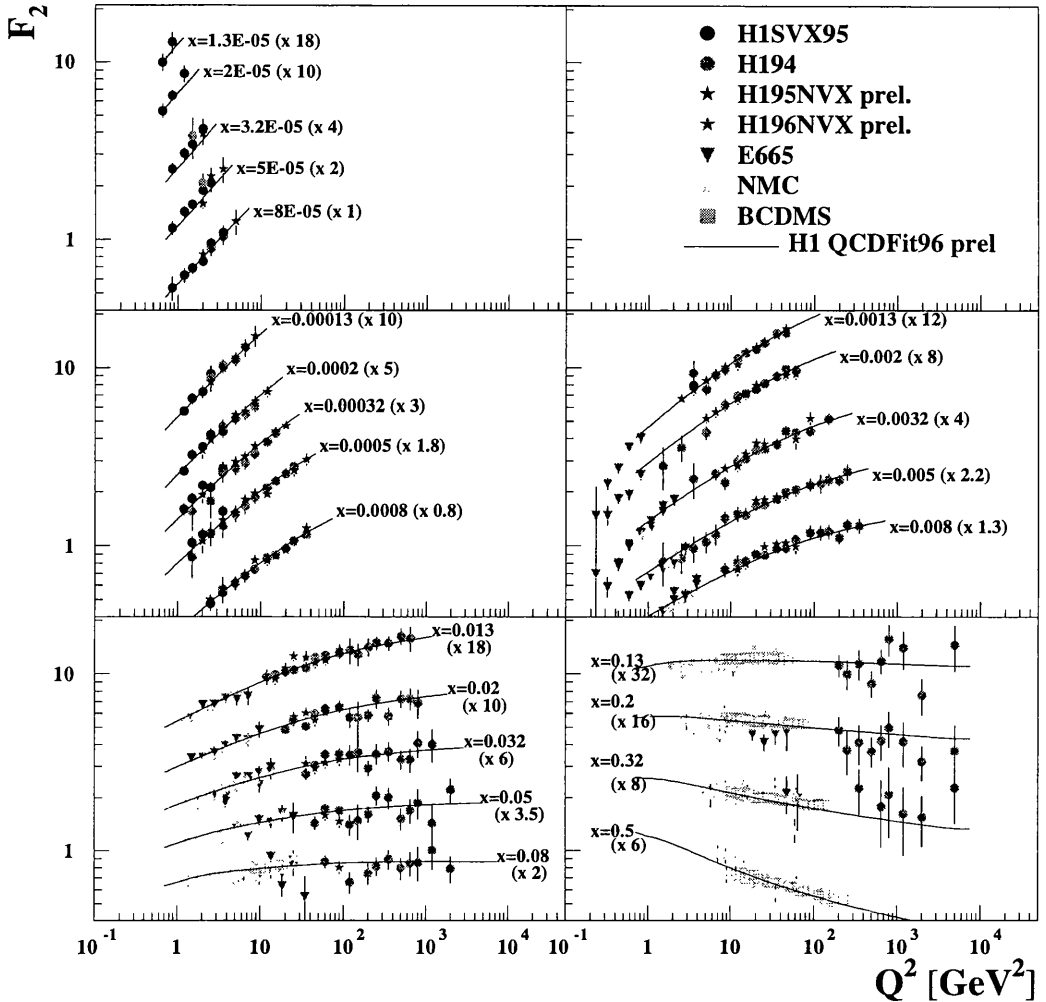
Figure 1.2: $F_2(Q^2)$ measurements at different values of x.

The gluon interactions not only modify the overall contents of the proton, but also the measurement of individual parton momenta. Studies of the structure function $F_2(x, Q^2)$ led to the observation that it has a logarithmic dependence on Q^2, first experimentally observed at SLAC. This failure to scale with Q^2 (i.e. failure to be independent of Q^2) - known as a scaling violation - follows directly from QCD. As the proton is probed at higher Q^2, the quarks are resolved with fewer of their attendant cloud of gluons. Thus at higher energies there appear to be fewer partons carrying a large fraction of the proton's momentum, and more carrying a small fraction. Recent measurements of F_2 are shown in figure 1.2 (courtesy of reference [11]). The data for $x \lesssim 0.1$ rise with Q^2 due to the dominance of the gluon at small x. In addition, the

data at high x ($\gtrsim 0.2$) fall with Q^2.

F_2 cannot be calculated in perturbative QCD (pQCD) but, if known at one value of Q^2, can be evolved to any other Q^2 using the DGLAP evolution equations [12, 13]. A number of different parametrisations exist for the structure functions in terms of parton density functions (PDFs). A thorough, wide-ranging and up-to-date review of the measurement and parametrisation of nucleon structure can be found in reference [14].
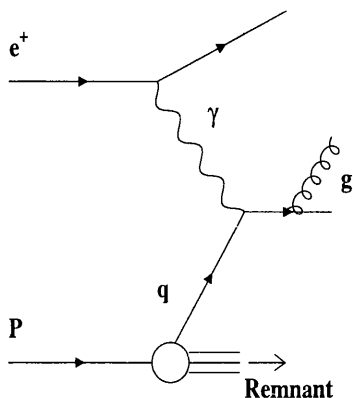
Figure 1.3: QCD-Compton diagram.
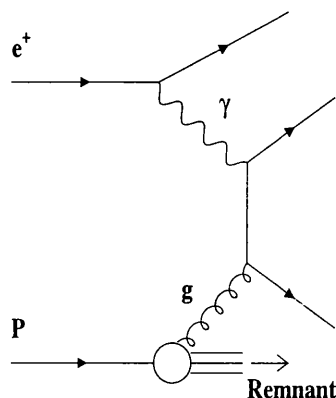
Figure 1.4: Boson-Gluon Fusion diagram.

Once gluon interactions are allowed into the QPM, further processes can contribute to the DIS cross-section. The leading order α_s (LO) processes - that is, processes with one QCD vertex - are: a) initial- or final-state QCD Compton (QCDC), where a gluon is radiated by the quark before or after it interacts with the photon; and b) Boson Gluon Fusion (BGF), where one of the gluons inside the proton interacts with the virtual photon via a $q\bar{q}$ pair. The Feynman diagrams for these processes are shown in figures 1.3 and 1.4 respectively. The processes are known collectively as (2+1) processes, i.e. processes which produce two partons and one proton remnant. The (2+1) cross-section is currently calculated to $\mathcal{O}(\alpha_s^2)$.

One of the most significant aspects of QCD is the ability of gluons to interact with one another - unlike, for instance, QED where photons carry no electric charge. Since

gluons carry approximately twice the colour charge of quarks, self-interactions tend to dominate. Therefore, in order to describe the running of the strong coupling constant, there must be not only terms for the screening of the colour charge (where a gluon fluctuates into a $q\bar{q}$ pair) but also for antiscreening (where a gluon fluctuates into a pair of gluons). To leading order, the scale dependence of the strong coupling constant can be expressed as

$$\alpha_s(Q^2) = \frac{12\pi}{(33 - 2N_f)\ln(Q^2/\Lambda^2)}$$

where N_f is the number of active quark flavours and Λ^2 can be thought of as representing the boundary value of Q^2 separating the perturbative and non-perturbative regimes in a specified renormalisation scheme. The value for Λ is not predicted by theory but is a free parameter to be determined by experiment. In next-to-leading order (NLO) the definition of Λ is further prescribed by its scheme dependence, conventionally chosen to be $\overline{MS}$ (see, for instance, reference [15] and references therein).

The result is a coupling constant which tends to zero at large energies (or short distances). This property is known as *asymptotic freedom*, and guarantees that partons inside a hadron behave as though they are alone and free, so that interactions can be calculated using perturbative techniques. For $Q^2 \gg \Lambda^2$, α_s is small and we are in the world of quasi-free quarks and gluons, while for $Q^2 \sim \Lambda^2$ the quarks and gluons interact to form bound hadronic states. The growth of α_s at large distances is responsible for the total *confinement* of quarks inside colourless hadrons.

Thus, in DIS, α_s grows as the struck quark moves away from its parent proton, and the escaping quark radiates gluons under the influence of the colour field between it and the proton remnant. As it radiates, its virtuality decreases and the strength of α_s increases. The strength of the colour field increases until there is sufficient potential energy to create a $q\bar{q}$ pair out of the vacuum. The new quark pairs and the radiated gluons interact with one another and the struck quark generates a shower of partons. As this process continues, α_s continues to grow and rapidly crosses the boundary beyond which interactions can no longer be described perturbatively. In the non-perturbative region the parton showering process continues until the individual partons reach a sufficiently low virtuality, at which stage the quarks and gluons combine

to form colourless hadrons in a process known as hadronization.

1.3 Fragmentation Functions
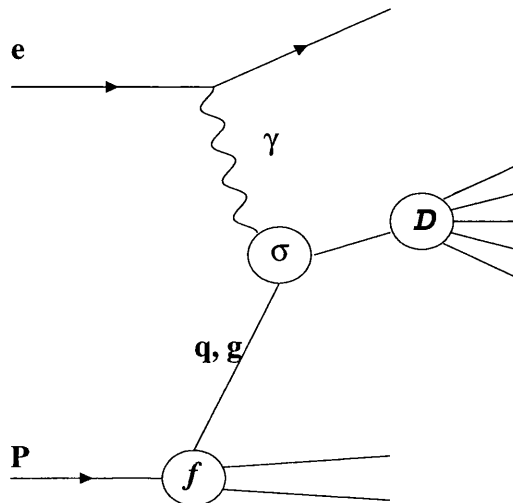
Figure 1.5: Schematic diagram showing the factorization of a DIS interaction into different processes.

According to the factorization theorem of QCD [16], the cross-section for any hard process can be written as a convolution of a perturbatively calculable hard scattering cross-section with a non-perturbative phenomenologically-defined PDF. The soft (long-distance) part is predicted to be universal, i.e. all soft phenomena can be factorized into universal PDFs, irrespective of the hard process which spawned them.

The non-perturbative fragmentation of partons into hadrons can be treated with a similar approach to that of PDFs to describe the embedding of partons inside hadrons; that is, by parameterising the ignorance about the confinement into phenomenological functions. A parton fragmentation function, $\mathcal{D}_q^h(z, Q^2)$, is defined which represents the probability that a hadron h will be found in the debris of a quark q carrying a fraction z of the quark's energy. The factorization of the DIS process is illustrated in figure 1.5: the interaction can be ordered in time and represented as a convolution of a parton density with the hard scattering cross-section and a fragmentation function:

$$\sigma = f(x, Q^2) \otimes \hat{\sigma}(Q^2) \otimes \mathcal{D}(z, Q^2).$$

The hard scattering cross-section, $\hat{\sigma}$, is perturbatively calculable to a defined order in α_s. The proton parton densities, f, cannot be calculated perturbatively but are derived phenomenologically and evolved to the requisite value of Q^2. The fragmentation function, $\mathcal{D}$, is also not perturbatively calculable but is derived from phenomenological fits and evolved using DGLAP evolution. The strong coupling constant enters through the Q^2 dependence of each of these components.

In a similar way to structure functions, the fragmentation functions are expected to fail to scale with Q^2. The amount of gluon radiation from a quark varies logarithmically with the energy scale, Q^2, of the interaction, due to the increase in the available phase space with increasing energy as well as the running of α_s. These effects lead to variations in the momentum spectra of the final-state hadrons as a function of the energy scale, even if the momenta are scaled to that energy. This can be pictured again as an effect of the increase of resolution obtained by increasing Q^2: there is an increased probability of finding a quark at small z and a decreased probability of finding one at high z because high-momentum quarks lose momentum by radiating gluons. Therefore, a measurement of the single particle density, $1/\sigma_{tot}\ d\sigma/dz$, as a function of Q^2 would be expected to find scaling violations [1].

Experimentally it is often more practical to measure the scaled momentum of a particle,

$$x_p = \frac{2p_h \cdot q}{Q^2} \quad \text{rather than its scaled energy} \quad z = \frac{2E_h \cdot q}{Q^2} :$$

the variables are equivalent over most of the spectrum of x_p, x, and Q^2, only diverging where the mass of the particle h becomes important. Studies of the scaled momentum spectra, $x_p = 2p/\sqrt{s}$, of charged final-state hadrons, where $\sqrt{s}$ is the centre-of-mass energy, have been widely performed by e^+e^- annihilation experiments [2, 3, 4]. By combining data measured to high accuracy at LEP with lower energy data from PETRA (and recently with higher energy data from LEP1.5 and LEP2) scaling violations have been found in the single particle density, $\frac{1}{\sigma_{tot}} \frac{d\sigma}{dx_p}$ (where σ_{tot} is the total cross-section for the interaction), as a function of $\sqrt{s}$. A value for α_s was determined by fitting these data. The aim of the analysis presented in this thesis is to carry out a similar study of the final state in NC DIS interactions at HERA, where fragmentation functions can be

measured over a range of energy scales in a single experiment.

The theoretical tools for such a study are now available in NLO. Although progress in the field of fragmentation functions has lagged behind that of parton density functions, great strides forward have been made in the last five years and various sets of next-to-leading order fragmentation functions have been made available. We shall concentrate on some of the most recently presented [17, 18, 19] which have direct relevance to this thesis. Inclusive and exclusive fragmentation functions for charged hadrons have been derived from e^+e^- annihilation data with next-to-leading order (NLO) fits at a number of different values of $\Lambda^4_{\overline{MS}}$ [19]. In particular, the availability of data where the different quark flavours are distinguished has enabled a great step forward in this area. The theoretical paradigm treats all partons and hadrons as massless, and the non-negligible masses of the c and b quarks are taken into account via thresholds in the evolution of the fragmentation functions. The gluon fragmentation function can be constrained using 3-jet data.

In the massless approximation what is actually calculated for each hadron is the energy fraction z where $0 < z \leq 1$. This is equivalent to calculating x_p as long as the values are large: threshold effects become important for $x_p \sim 2m_h/\sqrt{Q^2}$. The theoretical framework loses viability for small x_p, since DGLAP evolution of the fragmentation function involves the summation of logarithms in $1/x_p$, therefore data with $x_p < 0.1$ are discarded. Data with $x_p > 0.8$ are also disregarded, due to poor statistics and to the complication of the phenomenological picture at high x_p by products of weak decays which cannot be separated experimentally from the products of strong interactions. Particles and antiparticles are not discriminated, so that $\mathcal{D}^h_{q_i} = \mathcal{D}^h_{\bar{q}_i}$, and additional symmetry constraints are made use of, e.g. $\mathcal{D}^{\pi^\pm}_u = \mathcal{D}^{\pi^\pm}_d$. The procedure followed is, starting at a low scale $\mu^2_0 = 2$ GeV^2 with 3 flavours of quarks plus the gluon, to parametrise the fragmentation function of parton a to fragment into hadron h in the standard form [20]

$$\mathcal{D}^h_a(x, \mu^2_0) = N_a x^{\alpha_a}(1-x)^{\beta_a}.$$

The quark and gluon fragmentation functions are then evolved up to the centre of mass energy Q, adding in parametrisations of the charm and bottom quarks in the same form

as their respective mass thresholds are passed. The DIS single particle cross-sections are then calculated by convoluting the parton distribution functions with the evolved set of parton fragmentation functions via the NLO matrix elements. The results are compared with the data and the fit optimized by varying the values of N_a, α_a and β_a.

The phenomenological description provided by these functions is predicted to be universal, that is, to be the same whatever the interaction. Thus, on interfacing them to CYCLOPS [21], which implements the matrix elements for processes contributing to DIS up to next-to-leading order and with NLO PDFs, a description of the hadronic final state in DIS at large x_p can be obtained.

The massless simplification fails in areas where a hadron's momentum is small enough that its mass is no longer negligible. This tends to occur in the small x_p region where the evolution of the fragmentation functions is already vulnerable due to the summation of large logarithmic terms in $\frac{1}{x}$. The fragmentation process at intermediate x_p is better described by another approach, which is discussed below.

1.4   Fragmentation at low x_p

Study of the fragmentation variable, x_p, perforce concentrates attention on the larger values of x_p where scaling violation effects can be expected to be seen. However, particles with large momenta make a small contribution to the overall final hadronic state. An alternative method of studying fragmentation is instead to measure the variable $\ln\left(\frac{1}{x_p}\right)$, and thus to observe the properties of the bulk of the particles contributing to the parton shower. These are the partons with intermediate energies which are dominated not by the quarks in the shower but rather by their accompanying soft gluon radiation.

In the relativistic limit the probability for an individual parton to radiate another parton is predicted at $\mathcal{O}(\alpha_s)$ by the Altarelli-Parisi splitting functions [13] where, for instance,

$$P_{qq}(z) = \frac{4}{3}\left(\frac{1+z^2}{1-z}\right)$$

relates to the probability that a quark with momentum p will radiate a gluon to become a quark with momentum zp. Early attempts to predict the hadronic final state used

the Leading Log Approximation (LLA), where the splitting functions were evolved in the parton shower and combined with a hadronization coefficient. The results, however, failed to reproduce the experimentally observed distributions. The approach omitted the consideration that the bulk final state is not just a sum of the parts: the individual partons in the shower do not act independently of one another and in fact interfere destructively. The concept of destructive interference in parton cascades is described in terms of colour coherence.
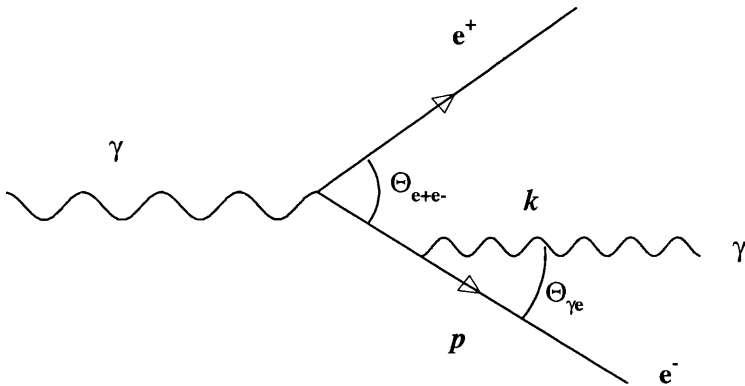
Figure 1.6: Bremsstrahlung radiation of a photon k after e^+e^- pair production.

The physical origin of colour coherence can be described by analogy with a similar electromagnetic effect seen in the radiation pattern of soft photons produced by a relativistic e^+e^- pair in a QED shower - the "Chudakov effect" [22] (see [23] and references therein). Figure 1.6 shows Bremsstrahlung from an e^+e^- pair formed by pair-production. The opening angle between the e^+ and e^- is $\Theta_{e^+e^-}$; the Bremsstrahlung photon is emitted with four-momentum k at an angle $\Theta_{\gamma e}$ relative to the e^- direction. In order to establish to what extent Bremsstrahlung can occur independently it is instructive to consider the formation time t_{form}, that is, the time needed for the photon to be emitted from one of the lepton legs. Using the uncertainty relation to estimate the lifetime of the virtual electron in the "laboratory frame", one finds

$$t_{form} \approx \frac{1}{M_{virt}}\frac{p}{M_{virt}} \approx \frac{1}{k\Theta_{\gamma e}^2}$$

where the electron has three-momentum p and virtual mass M_{virt}.

Now $k\Theta_{\gamma e^-} = k_T = \lambda_T^{-1}$, where λ_T represents the transverse wavelength of the radiated photon. So one can write the formation time as

$$t_{form} \approx \frac{\lambda_T}{\Theta_{\gamma e}}$$

During this period of time the $e^+ e^-$ pair separates transversely by a distance

$$\rho_T^{e^+ e^-} \approx \Theta_{e^+ e^-} t_{form} \approx \lambda_T \frac{\Theta_{e^+ e^-}}{\Theta_{\gamma e}}$$

Evidently for large angle photon emissions, where $\Theta_{\gamma e^-} \approx \Theta_{\gamma e^+} \gg \Theta_{e^+ e^-}$, the separation of the two emitters, e^+ and e^-, proves to be smaller than λ_T. In this case the emitted photon cannot resolve the internal structure of the $e^+ e^-$ pair and probes only its total electric charge, which is zero. Thus, for $\Theta_{\gamma e^-} \gg \Theta_{e^+ e^-}$ it is expected that the emissions of photons will be strongly suppressed. A similar picture can be drawn for QCD cascades where soft gluon radiation is governed by the conserved colour currents, although it becomes more complicated as the predominantly gluon cascade develops. Nevertheless, the final result of negative interference is maintained.

Coherence appears as a limitation in the phase space available for soft gluon radiation: successive final state emissions are emitted with decreasing transverse momentum, p_T, i.e. at smaller angles relative to the parton which emits them. It effectively restricts successive gluon emissions to decreasing smaller angles, an effect known as angular ordering. This leads to a slower rise in the gluon multiplicity within a parton jet and to a change in the shape of the gluon momentum distribution relative to the case of incoherence. The suppression of soft gluon emissions at wide angles modifies the inclusive momentum spectrum of partons within the cascade to give the so-called "hump-backed plateau" [23]. The result is an approximately Gaussian distribution of $\ln(1/x_p)$, which is predicted to evolve with energy in a well-defined manner. Coherence effects assume great importance in studies of the final hadronic state, since the soft particles which are most affected are the particles which at the same time make up the bulk of the multiplicity.

The Modified Leading Log Approximation (MLLA) of pQCD provides a quantitative description of the properties of particles radiated from high energy quarks and gluons. It takes account of the coherence effects implicit in parton showering

and is based on a probabilistic picture of the shower development. The MLLA gives an equation for the evolution of the momentum spectrum of the parton shower associated with a high energy parton; it is also linked with a hadronization model. This hadronization hypothesis, Local Parton-Hadron Duality (LPHD) [24], stems from the preconfinement properties of QCD cascades; it corresponds to a local phase space colour blanching and hadronization of the partons into hadrons. The assumption is that parton spectra can be transformed into hadron spectra simply by the application of a normalization constant. It is important to mention that there is no implication of one-to-one correspondence between partons and hadrons event-by-event, merely that their average behaviour (and the fluctuations around that average) coincide. The normalization factor is the only arbitrary parameter resulting from this hypothesis and must be experimentally determined. To date, experimental studies have shown that LPHD works rather well. A comprehensive review of the analytical pQCD approach, largely involving the MLLA and LPHD, to multiparticle production in jets in the semisoft region can be found in [25].

The application of LPHD to the MLLA hump-backed plateau allows the prediction of the behaviour of experimentally-observed hadrons. Since the transformation of partons into hadrons is predicted to be independent of the CM energy, the analysis of the evolution of the hadron spectrum with E_{CM} should be insensitive to hadronization effects and provide information on the energy evolution of the underlying gluon spectrum.

1.5 The Breit Frame

One of the crucial questions in the study of physics at HERA is the identification of the most appropriate reference frame in which to observe the final state particles. Since DIS involves a hard interaction between the intermediate boson and the struck quark within the target proton - rather than directly between the incident electron and the proton - the laboratory frame is not a logical choice of frame in which to study the process.

A more natural frame of reference is the Breit ("brickwall") frame of reference [26],

Electron-positron Annihilation   DIS in the Breit Frame
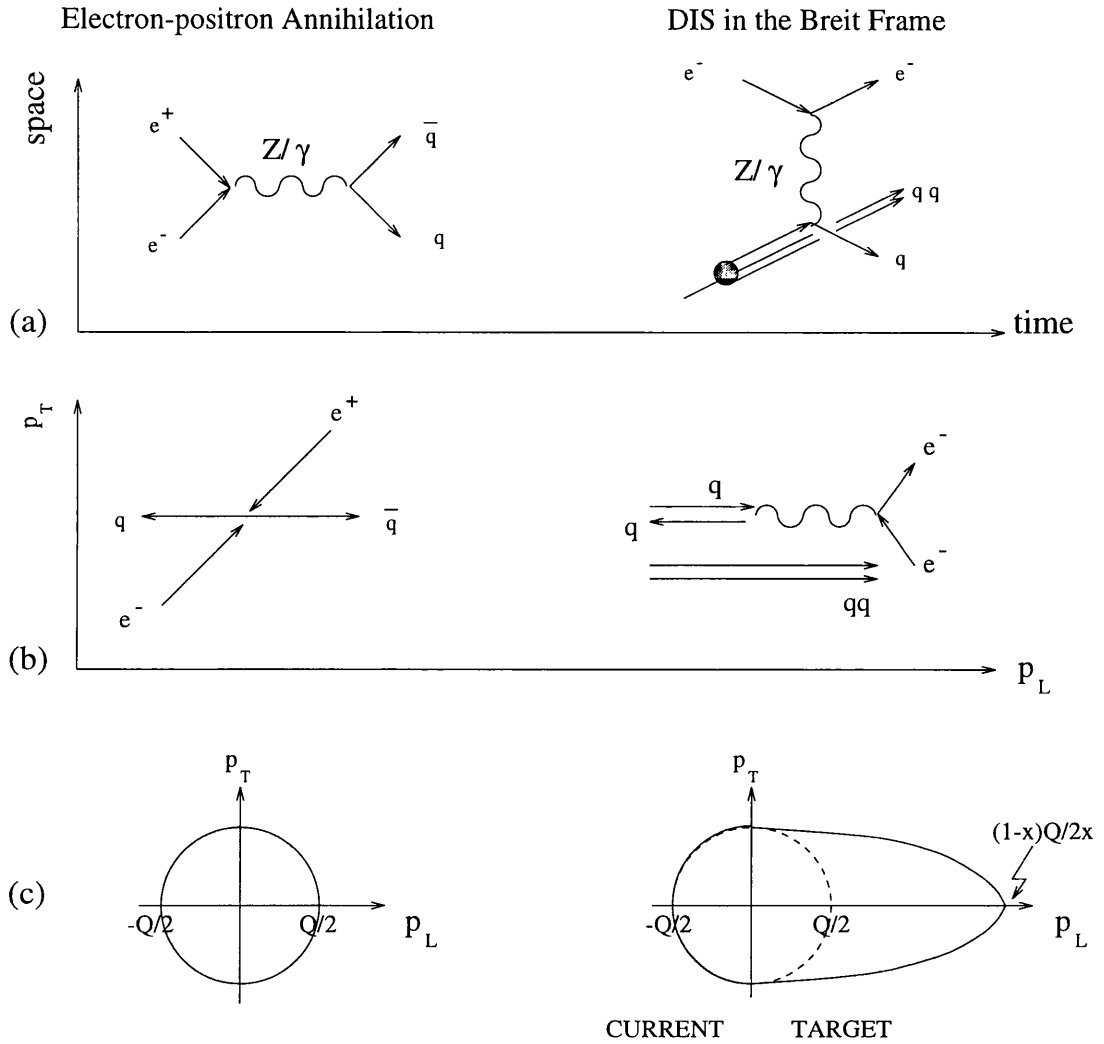
Figure 1.7: e^+e^- annihilation compared with DIS in the Breit frame

in which the exchanged boson is completely spacelike, i.e. in DIS the exchanged boson has four-momentum $q = (0,0,0,-Q)$. This is in direct analogy with e^+e^- collisions in their centre of mass, where the photon is purely timelike, but with the additional benefit that the exchanged boson conveniently provides a natural axis. Figure 1.7 depicts a QPM DIS interaction in the Breit frame: the struck quark is incident with z-momentum $p_z = Q/2$ and rebounds from the the intermediate boson as if from a brick wall, to leave with $p_z = -Q/2$. The frame separates naturally into two parts: the current region containing the struck quark, and the target region containing the proton remnant. In the target region, $p_z > 0$, the proton remnant develops with

momentum $p_z = (1-x)Q/2x$. This region is not well understood. In the current region, $p_z < 0$, the struck quark evolves with $p_z = Q/2$. Working in this frame maximises the spatial and momentum separation of the struck quark and proton remnant, so that the clearest possible separation can be made for the study of the single particle inclusive distributions.

For a DIS event, the velocity of the Breit frame with respect to the laboratory frame is given by $\vec{\beta} = (\vec{q} + 2x\vec{P})/(q_0 + 2xP_0)$, where $(q_0, \vec{q})$ and $(P_0, \vec{P})$ are the 4-momenta of the exchanged boson and the incident proton beam respectively. DIS events are boosted and then rotated so that the virtual photon is along the negative z axis and the plane of the incoming and outgoing positron contains the $\phi = 0$ direction.

The current region closely resembles a single hemisphere of an e^+e^- annihilation event, enabling comparisons to be made between LEP measurements and DIS. The outgoing struck quark carries momentum $Q/2$, compared with e^+e^- annihilation in the laboratory frame where there are two outgoing quarks, each with momentum $\sqrt{s}/2 \equiv Q/2$. The Bremsstrahlung processes accompanying the emission of a bare quark in the current fragmentation region lead to the formation of a jet identical to the quark jet in an e^+e^- annihilation at energy $\sqrt{s} = Q$ [27]. It should be noted however that interference between the current and target region can never be completely accounted for [28]. Moreover, it is important to recognise that the picture of $\mathcal{O}(\alpha_s)$ processes in the Breit frame is somewhat more complicated than the basic QPM diagram given in figure 1.7.

The presence of strongly-interacting partons in the initial state of DIS means that the BGF and initial-state QCDC processes may contribute to the overall cross-section, in contrast to e^+e^- annihilation where there are no strongly-interacting partons in the initial state. The BGF and QCDC processes both give rise to a pair of partons in the final state (ignoring contributions from the proton remnant) which may possess large transverse momentum. The three possible resulting topologies are illustrated in figure 1.8: it is possible for one or both of the parton jets to be found in the target region. At $\mathcal{O}(\alpha_s)$ the dijet cross-sections for these processes can be expressed in terms of an angular variable z_p and an event variable x/ξ. The jet scaling variable z_p is related to the angular distribution of the jets in the γ^*-parton centre of mass system (which is

equivalent to the Breit frame if $Q^2 = \hat{s}$), and is defined as

$$z_p = \frac{P.p_{\text{jet}}}{P.q} = \frac{1}{2}(1 - \cos\theta^*_{\text{jet}}) \qquad (0 \leq z_p \leq 1),$$

where θ^*_{jet} is the polar angle of the jet, which is assumed to be massless, in the γ^*-parton CMS. The event variable x/ξ is defined as

$$\frac{x}{\xi} = \frac{Q^2}{2p.q} \approx \frac{Q^2}{Q^2 + \hat{s}}$$

for massless jets, where $\sqrt{\hat{s}}$ is the invariant mass of the two-jet system. The behaviour of the cross-sections is given by [29]

$$d\sigma^{\text{BGF}} \propto \frac{1}{z_p(1 - z_p)} \quad \text{and} \quad d\sigma^{\text{QCDC}} \propto \frac{1}{(1 - x/\xi)(1 - z_p)} \quad .$$

Both processes have a singularity at $z_p = 0$ or 1, related to the emission of collinear partons. The $x/\xi = 1$ singularity in the QCDC cross-section results in a preference for small jet-jet invariant mass to be produced by this process, i.e. soft parton emissions. Such events favour topologies where two jets balanced in p_T are found in the current region (figure 1.8 b). This suppression is not present in the expression for the BGF cross-section, so that the production of jets with large invariant mass is dominated by the BGF process.

It has been observed [30] that the x/ξ spectrum peaks far down towards zero in events at small Q^2 and x, where BGF is expected to be the dominant contribution. In these processes $Q^2 \lesssim \hat{s}$, and $\hat{s}$ is the largest scale. Such events - which have no equivalent in e^+e^- annihilation - tend to have the topology shown in figure 1.8 d) where neither of the final partons is found in the current region. Distributions measured in the current region of the Breit frame at low x are expected to be sensitive to this effect, known as depopulation.
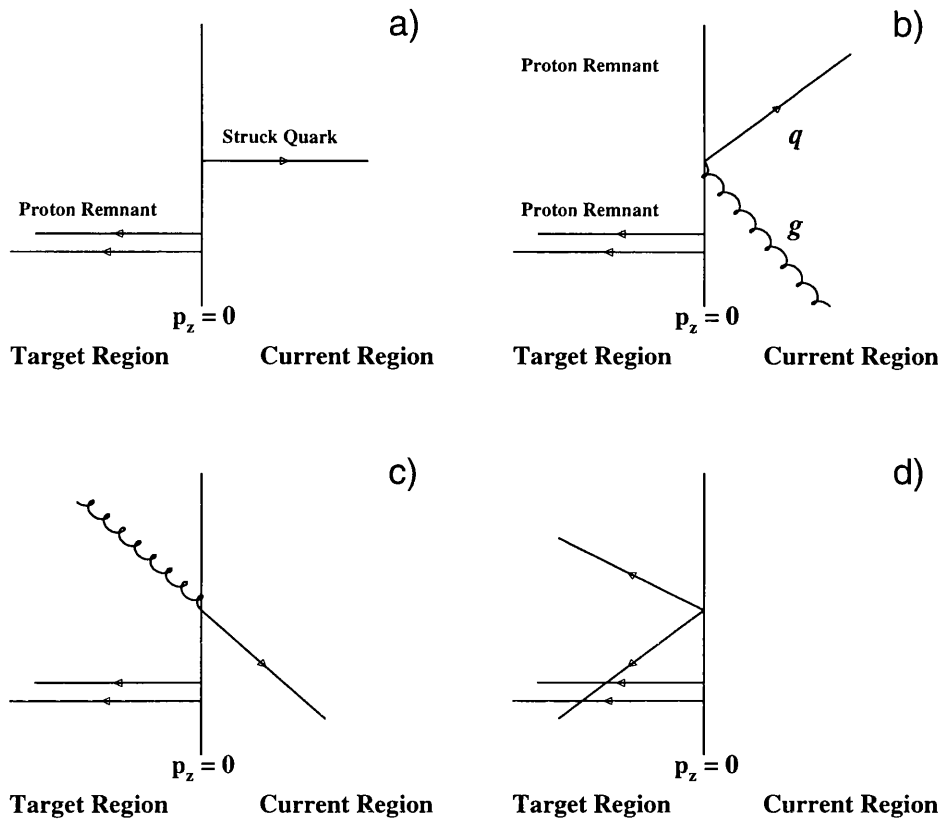
Figure 1.8: a) zeroth order DIS in the Breit frame. Possible topologies for leading order DIS interactions in the Breit frame: QCDC diagrams for b) low mass radiation ($\hat{s} < Q^2$) and c) intermediate mass radiation ($\hat{s} \approx Q^2$), d) BGF diagram for large mass radiation ($\hat{s} > Q^2$).

1.6 Summary

An outline has been given of the lower-order QCD processes contributing to DIS at HERA and to the process of fragmentation. Methods by which the properties of the fragmentation process can be predicted have been described. The properties of the Breit frame of reference have been introduced. This frame of reference provides the maximum separation of the current jet from the proton remnant, and thus enables the direct comparison of quark fragmentation properties in DIS with those exhibited by quarks produced in e^+e^- annihilation experiments.

Chapter 2

HERA and the ZEUS Detector

2.1 HERA

HERA (Hadron Electron Ring Accelerator) is an electron-proton (ep) collider based at the Deutsches Elektronen Synchrotron (DESY) in Hamburg, Germany. Its layout is shown in figure 2.1. The HERA ring is approximately circular with a circumference of about 6335 metres and a tunnel diameter of 5.6 m. The accelerator was designed to collide beams of electrons with energy 30 GeV and protons with energy 820 GeV. The beams are carried in two separate synchrotron rings contained in a tunnel about 20 m below ground level. There are four experimental halls spaced evenly around the ring. The beams are brought together in two of them (the North and South halls) where the general purpose detectors H1 and ZEUS are located. The East and West Halls house two more specialised experiments (HERMES and HERA-B) which parasite off the positron and proton beams respectively. HERMES is intended to measure the polarised nucleon structure functions by observing the interactions of the positron beam with a polarised gas stream, while HERA-B is aimed at measuring CP violation in the B system by dangling wires into the proton beam. HERA was commissioned in 1991. The first ep interactions were observed in ZEUS and H1 during the spring of 1992.

HERA initially collided electrons with protons, but early in 1994 problems with the lifetime of the electron beam motivated a decision to change to positron operation, since the electron current was limited by interactions with residual positively-charged
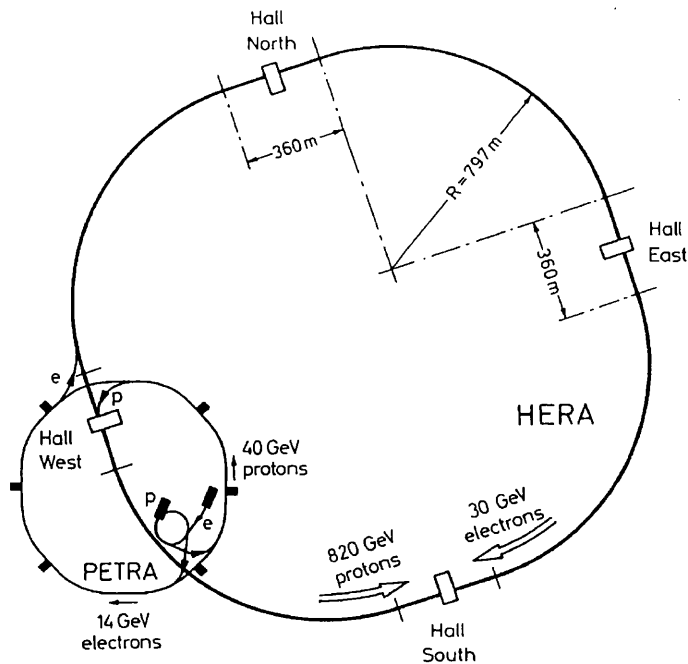
Figure 2.1: The layout of the *ep* collider facility at DESY. The main colliding ring, HERA, is shown, along with the smaller rings in which particles are accelerated up to their HERA injection energies. ZEUS is situated in the South Hall.

dust particles in the beam-pipe. Between 1994 and 1997, HERA provided collisions between 820 GeV protons and 27.5 GeV positrons.

Establishing the beams at their colliding energies in the HERA ring is a long process of accelerating bunches of particles in a sequential set of rings. Electrons (positrons) from a 500 MeV linear accelerator are injected into a small synchrotron where they are accelerated further and accumulated into bunches. When they reach 7 GeV they are injected into PETRA[1], accelerated up to 14 GeV and then injected into HERA. In HERA they undergo further acceleration until reaching the operating energy of 27.5 GeV. A 50 MeV linear accelerator is used to strip negatively charged hydrogen ions of their electrons and inject them into the small proton synchrotron. There they are accelerated to 7.5 GeV prior to injection into PETRA. They are accelerated to 40 GeV before the final injection into the HERA ring.

---

[1] Positronen-Elektronen Tandem Ring Anlage

HERA operates with a maximum of 210 'buckets' spaced 96 ns apart which can be filled, or not, with bunches of particles. In 1994 there were 153 paired *ep* bunches, as well as 15 unpaired e^+ bunches and 17 unpaired p^+ bunches; the remaining buckets were left empty. These unpaired and empty bunches are used for monitoring the backgrounds from beam-gas interactions and cosmic rays. Since the positron bunch length is small, the length of the interaction region is governed by the proton bunch length; taking into account the run-to-run variations of the mean interaction position, this leads to a length of the interaction region of $\sim$ 12 cm (r.m.s.) offset by about 6 cm in z along the direction of the proton beam.

2.2 ZEUS

The transverse $(r\text{-}\phi)$ and longitudinal $(r\text{-}z)$ cross-sections through the ZEUS detector are shown in figures 2.2 and 2.3, respectively. The ZEUS coordinate system is defined as a right-handed orthogonal coordinate system: the origin is at the nominal interaction point and the z-axis points along the direction of the proton beam. The x-axis points towards the centre of the HERA ring and the y-axis directly upwards. Polar angles, θ, are measured from 0° along the proton beam direction to 180° along the positron beam. Azimuthal angles, ϕ, are measured with respect to the x-axis. The asymmetry between the momenta of the positron and proton beams boosts the centre of mass system in the forward direction - that is, in the direction of travel of the proton beam - with respect to the laboratory frame. For this reason the detector is asymmetric in z.

Moving outwards from the nominal Interaction Point (IP), particles first encounter the vertex detector (VXD)[2] , followed by the charged particle detection system comprising the Central Tracking Detector (CTD) and the forward and rear tracking detectors (FDET and RTD). The tracking detectors are enclosed in a superconducting solenoid which provides a high and uniform magnetic field. Beyond the tracking systems and solenoid coil lies the high resolution uranium calorimeter (CAL) which is partitioned into Forward, Barrel and Rear sections (FCAL,BCAL,RCAL). Further outwards from

---

[2]The VXD was removed following the 1995 data-taking period, due to its susceptibility to beam damage. A new silicon microvertex detector is currently in preparation.

the CAL are the iron yoke, which returns the magnetic flux and contains a backing calorimeter (BAC), followed by the muon detectors. A compensating superconducting solenoid, to correct for the influence of the field from the superconducting solenoid on the colliding beams, is located behind the RCAL.

The primary components pertinent to this analysis are the CTD, CAL and Small-angle Rear Tracking Detector (SRTD). They are discussed more fully below. A detailed description of the ZEUS detector and its components can be found in [31].
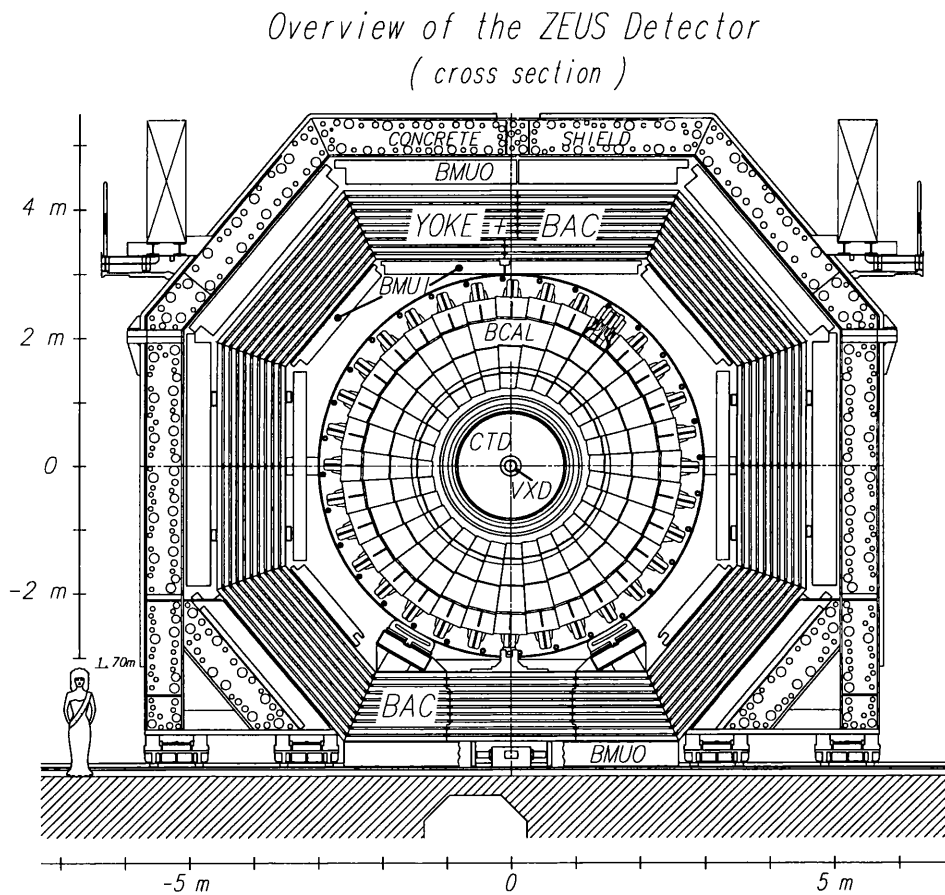
Figure 2.2: r-ϕ cross-section through the ZEUS detector.
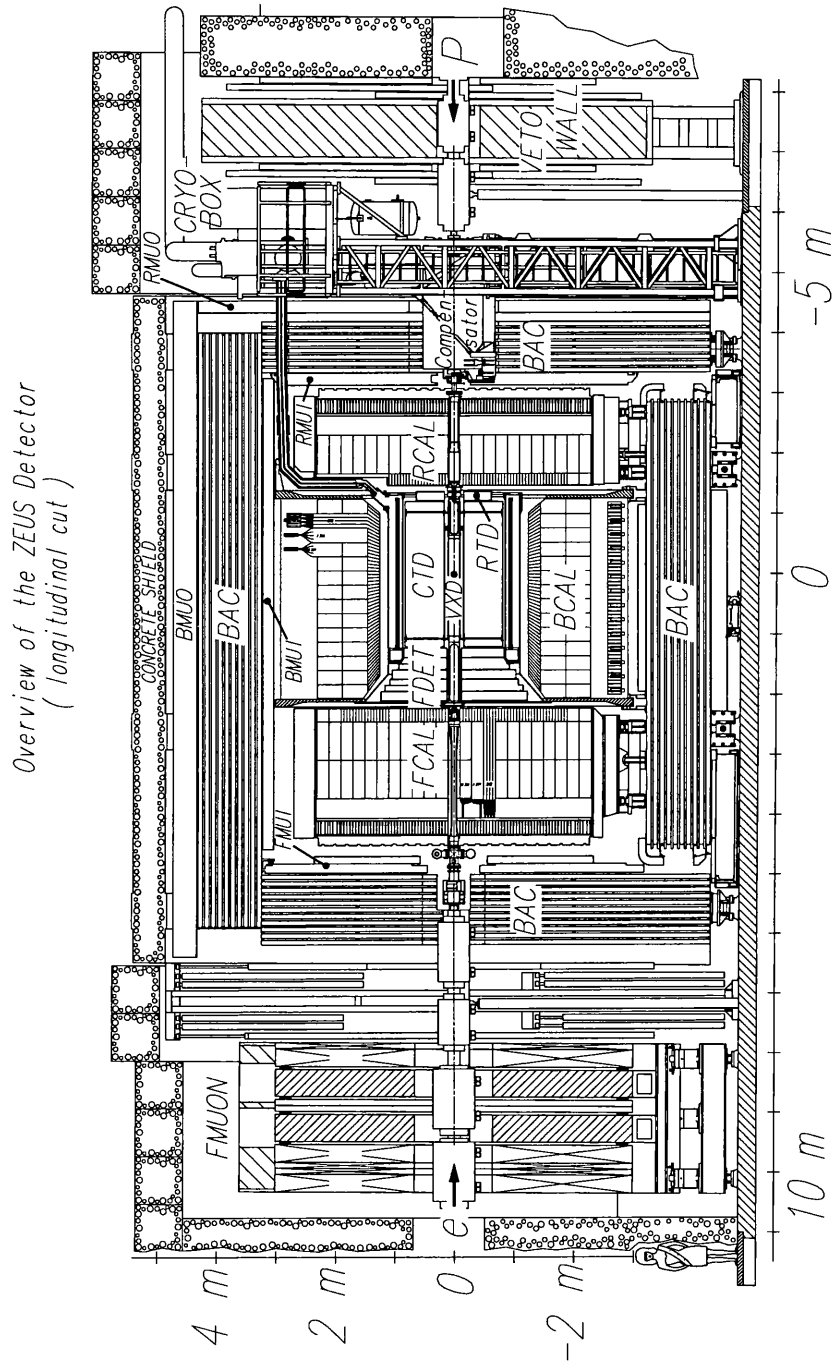
Figure 2.3: Longitudinal cross-section through the ZEUS detector.

2.2.1 CTD

Charged particle momenta are measured using the central tracking detector. The CTD is a cylindrical drift chamber, with an inner radius of 18.2 cm, an outer radius of 79.4 cm and an active length of 205 cm. The chamber is organised into 9 'superlayers', which are further subdivided into drift cells, each with eight sense wires. There are 4608 sense wires in total, covering an angular range of $15^0 < \theta < 164^0$.

There are two types of superlayers (SL): axial superlayers (odd numbers), with wires parallel to the chamber axis; and stereo superlayers (even numbers), whose sense wires are inclined at a small stereo angle ($\sim \pm 5°$) to the chamber axis. The values for the stereo angles are chosen so that the angular resolutions in polar and azimuthal directions are approximately the same. The stereo rotation allows the wires to be used to measure the z-coordinate of tracks traversing the chamber with a design resolution of $\sigma_z = 1.4$ mm. The stereo layers also provide increased accuracy in measuring the polar angle. Measurement of the differences in the arrival times of a chamber pulse at either end of a sense wire is used to provide a fast estimate of the z-coordinate using only a selection of the axial layers[3]. The resolution in z provided by z-by-timing is $\sigma_{zbyT} = 3$ cm.

The detector is filled with a argon/ethane/CO_2 gas mixture which was chosen as a reliable and fast ($\approx 50 \mu$m/ns) drift gas. Charged particles traversing the chamber ionize molecules in the gas mixture. The ionization electrons drift in the electric fields of the cells, giving rise to pulses registering on the sense wires. The chamber is designed so that the maximum drift distance in any cell is typically ~ 2.5 cm. The patterns of hits and associated drift times are then used to reconstruct the path followed by the charged particle. Figure 2.4 shows the wire layout for an octant of the CTD as it appears at one of the endplates. The drift cells are rotated so that the sense wire plane is at an angle of 45° to a radius vector from the centre of the detector. The CTD operates with a Lorentz angle of about 45°, that is, ionized electrons in a drift cell drift in a direction at 45° to the direction of the electric field lines. So the rotation of the cells ensures

---

[3]since the the 3D reconstruction necessary for the stereo z measurement is too complex for use in the trigger.
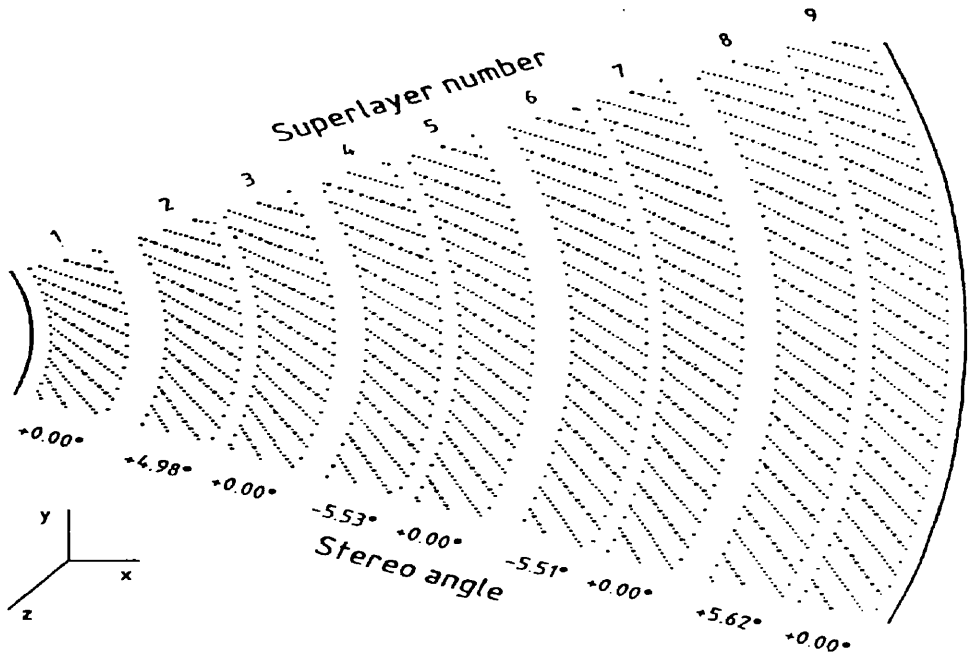
Figure 2.4: Diagram showing a cross-section of an octant of the CTD.

that the electron drift lines are perpendicular to the paths of high-momentum tracks originating at the nominal IP, thereby providing optimal resolution and minimising the left-right ambiguity[4] for such tracks.

The 1.43 T magnetic field produced by the solenoid exerts a transverse force on the charged particles, causing their trajectories to curve. Measuring the degree of curvature allows the momenta of the particles to be reconstructed. Positions of hits can be measured with a resolution of about 230 μ in r-ϕ. The resolution in transverse momentum, p_T, for full length tracks (i.e. tracks which pass through all 9 superlayers) is $\frac{\sigma_{p_T}}{p_T} = 0.005\ p_T \oplus 0.016$ (for p_T in GeV/c), where the first term is due to the space resolution of hits and the second term is due to multiple Coulomb scattering. $\oplus$ denotes addition in quadrature. The two-track resolution is 2.5 mm.

---

[4]i.e. the problem of resolving whether a hit happened to the left or right of the sense wire on which it registered.

2.2.2 The Calorimeter

The function of the ZEUS calorimeter is to absorb the energy of impinging particles, whether charged or neutral, and to translate it into light. In order to achieve this aim, a high-resolution sampling calorimeter has been designed which utilises layers of uranium and plastic scintillator. It is divided into the forward (FCAL), barrel (BCAL) and rear (RCAL) components, which cover the polar angle ranges $2.6° < \theta < 36.7°$, $36.7° < \theta < 129.1°$, and $129.1° < \theta < 176.2°$, respectively. Altogether, the solid angle coverage is 99.8% in the forward hemisphere and 99.5% in the backward hemisphere. Each component of the calorimeter is segmented longitudinally into an inner electromagnetic (EMC) and an outer hadronic (HAC) part: the EMC is read out as one section, and the HAC as two sections (except for the HAC in the RCAL which is read out as one). These sections are further subdivided into cells, of typical sizes 20×20 cm^2 for the HAC, and 5×20 cm^2 for the EMC. The total calorimeter consists of approximately 6000 cells, each read out by two photomultiplier tubes (PMTs).

Different types of particles interact with solid material in different ways. Energetic electromagnetic particles encountering a block of dense material radiate photons in a Bremsstrahlung process as they interact with the electromagnetic fields of the densely-packed atoms. The radiated photons produce e^+e^- pairs, which in turn radiate more photons as they undergo Bremsstrahlung interactions. Thus an electromagnetic "shower" results, which can be characterised for a particular material by the radiation length, X_0, the distance over which an electron's energy drops by a factor $1/e$. The transverse shower profile reaches a maximum near the point where the energies of the shower particles drop below the threshold necessary for the Bremsstrahlung and pair production processes. The remaining energy is then dissipated primarily through ionization and Compton scattering.

The physical processes underlying the propagation of a shower initiated by hadrons, on the other hand, are quite different. Hadrons not only undergo electromagnetic interactions but also typically interact with the nuclei of the absorbing material to produce more hadrons or to induce a nuclear decay. The produced hadrons interact with further nuclei and thus develop a hadronic shower. Hadronic showers tend to be

much broader than electromagnetic ones, and their characteristic radiation length, λ, is much larger than X_0 ($\lambda \simeq 25X_0$) so that an electromagnetic shower tapers off long before a hadronic shower in the same place has fully developed. The involvement of nuclei in hadronic showers - and the resulting large energy loss through nuclear binding energies, shorter mean free paths and the like - generally results in a smaller signal than an electromagnetic shower would produce. In addition, each hadronic shower has a variable electromagnetic component caused by the creation of π^0s (which can decay electromagnetically) in nuclear interactions. If the calorimeter does not respond equally to this electromagnetic component of the shower as to the hadronic component, then the energy measurement of the hadronic shower is severely affected.

In order to overcome this problem, the ZEUS calorimeter is a *compensating* calorimeter: that is, careful choices of absorber and active materials and thicknesses are combined to equalise the calorimeter's response to electrons and hadrons. The calorimeter is made up of plates of depleted uranium acting as an absorbing material, interleaved with scintillator tiles in layers of approximately 8 mm total thickness (~ 1 X_0). Showers passing through the calorimeter lose energy in the passage through the uranium layers and are sampled in the active scintillator layers, which produce a light signal on interaction with ionising particles. The scintillation light is collected by wavelength shifting plates and transmitted by total internal reflection onto a light guide which directs it into a PMT.

Under test-beam conditions the energy resolution of the calorimeter has been measured to be $\sigma_E/E = 0.18/\sqrt{E}$ for electrons and $\sigma_E/E = 0.35/\sqrt{E}$ for hadrons of energy > 10 GeV (E in GeV). For hadrons of energy 0.5 GeV it improves to $\frac{\sigma_E}{E} = 0.26/\sqrt{E}$. The timing resolution of a calorimeter cell is better than $\sigma_t = 1.5/\sqrt{E} \oplus 0.5$ ns.

In order to further improve the capabilities for distiguishing between hadronic and electromagnetic particles, an additional detector array was installed amongst the calorimeter layers. The Hadron Electron Separater (HES) discriminates between electromagnetic and hadronic showers originating from low energy particles (< 5 GeV). The HES consists of single layers of silicon diodes mounted 6.3 (3.3) radiation lengths into the FCAL (FCAL and RCAL), which should be close to the shower maximum of

an electromagnetic shower. At this point an electromagnetic shower would give a large signal while hadronic showers normally have their first interaction vertex at a greater depth and so behave like minimum ionising particles. The diodes have dimensions 3×3 cm^2, corresponding to an improvement in granularity over that offered by the CAL segmentation.

2.2.3 SRTD

The Small-angle Rear Tracking Detector was installed in the detector in 1994 to give precise measurement of the angles and energies of positrons scattered close to the direction of the positron beam where there is no coverage by other tracking detectors.

It is positioned on the inside face of the RCAL close to the beampipe. The detector consists of arrays of scintillator strips segmented into 4 quadrants, each measuring 25×44 cm^2. It covers an area 68×68 cm^2, except for the 20×2 cm^2 hole containing the beampipe. Each quadrant consists of 2 layers of scintillator strips in orthogonal orientations. The strips are 1 cm wide by 0.5 cm thick.

2.3 ZEUS Data-Taking and Reconstruction

2.3.1 Overview of Data Taking

This analysis includes data recorded by the ZEUS detector during the data-taking periods of 1994, 1995, 1996 and 1997: a total of about 800 days of running. Figure 2.5 shows the increase in the luminosity passing EVTAKE with each year, where 'EVTAKE' is the process through which events are filtered to check that they pass the triggers and DQM checks and are then written to tape, as described in section 4.3.1 There is a steep increase in the useful luminosity from 1993 as the operation of HERA has become better understood. The luminosities supplied by HERA for these years, the luminosities for events passing the online triggers and stored on tape by ZEUS, and the luminosities for on-tape events accepted after off-line reprocessing are shown by year in table 2.1.
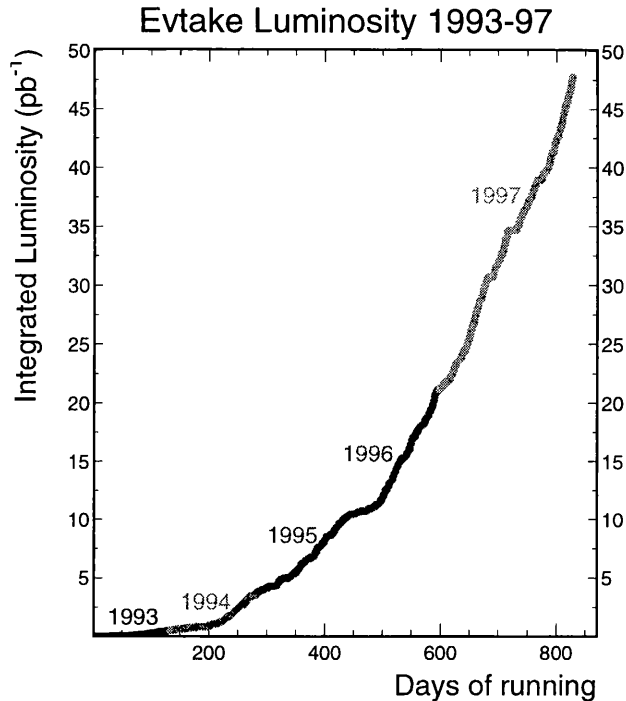
Figure 2.5: The luminosity taken by ZEUS between 1993 - 1997.

Year	HERA delivered(pb^{-1})	ZEUS on-tape (pb^{-1})	ZEUS EVTAKE (pb^{-1})
1994	5.11	3.30	3.02
1995	12.30	7.30	6.66
1996	17.16	11.26	10.71
1997	36.35	27.94	26.59

Table 2.1: ZEUS luminosities for e^+ running 1994-97.

Bunch crossings at HERA occur every 96 ns but relatively few result in interesting physics events. It is necessary to divide the useful physics from the backgrounds.

2.3.2 Backgrounds

The positron beam produces synchrotron radiation (although this is mostly produced in the bending arcs far away for the IP, and any produced close to the detector is mostly dealt with by the collimators etc.) The positrons also produce bremsstrahlung under the influence of nuclei in gas remaining in the beampipe. Such events can deposit a

large amount of energy in the rear part of the main detector which will prompt the trigger system to retain the event. However, these events leave very little energy in the forward part of the detector, in contrast to real *ep* events, and can thus be removed by online and offline analysis. The contribution of *e* gas events can be judged by including pilot *e* bunches in the machine whilst keeping the corresponding *p* bucket empty.

The proton beam is accompanied by a fairly large number of halo muons, as a result of the decays of pions created in collisions of beam particles with residual gas in the beam pipe or with the beampipe wall or collimators. Events caused by collisions of particles in the proton beam with remaining rest gas in the beam pipe form the major source of background to the interesting physics: the rate is estimated at ~ 50 kHz, which is to be compared with a rate of $\sim$ a few Hz for interesting physics. Accordingly, a trigger system is needed which can recognise the hallmarks of interesting events or of a particular type of background and decide whether the signals in the detector should be recorded or discarded. In addition, as data are accumulated the trigger is used to select a subsample of the most interesting physics data. In the earlier years it was used to remove photoproduction background, but as the amount of stored data has increased the trigger has been used to focus on e.g. higher E_T jets or high Q^2 DIS data. In this way useful information can be preserved and the amount of information which has to pass through the data acquisition system and also be stored can be kept within reasonable bounds. The trigger must limit the amount of data considered worth preserving to the amount that it is possible to store, acquired at a rate at which it is possible to store it; i.e. the trigger is confined by the rate at which events can be written to tape. In the ZEUS Data Acquisition system, events can be written to tape at a rate of 5 events per second. For instance, in 1997 20 million events of about 100 Kbytes each were recorded. Another factor which must affect the trigger design is that, with a bunch crossing time of 96 ns, it is impossible for an individual component to read out the data and provide a trigger decision for the interactions of one bunch-crossing before the next has occurred. The ZEUS solution to these limiting factors is a 3 level pipeline trigger system, clocked at 96 ns.

2.3.3 The ZEUS Trigger

The ZEUS trigger is designed as a three level system, composed of

- the First Level trigger (FLT), which is specific to each component of the detector. It eliminates most of the beamgas and beam halo backgrounds and reduces the rate to ~ 1 kHz.

- the Second Level Trigger (SLT), which performs some rudimentary analysis of the digitized data from the components and looks for signatures of physics interactions. The SLT reduces the trigger rate to ~ 100 Hz.

- the Third Level Trigger (TLT), which carries out more sophisticated analysis of the data, with access to the full event record. After the TLT, the rate has been reduced to < 10 Hz.

At every level there is a Global trigger which combines the information from the individual components.

For each bunch crossing, the data are stored in a pipeline, clocked at 96 ns, for $\sim 5\mu$s while the FLT calculations are performed and the FLT decision propagates back to the detector components. Each component completes its internal trigger calculations and passes information for a particular bunch crossing to the Global FLT (GFLT). The GFLT decision is issued exactly 46 crossings (4.4 μs) after the crossing that produced the data. The component data are jettisoned or are passed to buffers for processing by the SLT. SLT decisions are made in the order in which events are received. The SLT has access to a large fraction of the full data record for the event and is able to perfom iterative calculations that are not possible in the pipelined structure of the FLT. Events which pass the Global SLT are sent to the Event Builder, where the data from all the components are combined into a single event record, and thence to the TLT. Decisions by the TLT are based on a full analysis of the event: it runs a (reduced) version of the full offline analysis. The output rate from the TLT is $\sim$ 3-5 Hz.

If a particular bunch crossing passes the trigger selection, the event is reconstructed. The raw data digitisations from each component are corrected using the calibration

information for each detector (e.g. energy deposited in a particular calorimeter cell). At a second stage, information from different components is matched, eg. clusters of calorimeter cells, CTD-VXD track-matching, track-cell cluster track-matching etc.

2.3.4 Track Reconstruction

The track-finding algorithm, VCTRAK [32], begins with seed hits in the outer axial superlayers of the CTD. Each track seed is extrapolated inwards towards the beam axis, gathering additional hits with increasing precision as the trajectory parameters are updated. The arc in the xy plane is used for z-by-timing and stereo pattern recogition. If the candidate has z-by-timing measurements, these are used to provide a coarse first estimate of a 3D trajectory and to limit the region which must be searched for stereo hits. Eligible stereo superlayers are generally traversed by a trajectory that is already pinned on either side by axial hits. Every acceptable track candidate must ultimately have 3D information: either by z-by-timing, or stereo, or both. Periodically, tracks with too many shared hits are filtered out. Normally 85% of a candidate's hits must be unique to it, although this rule is relaxed somewhat when a track candidate spans at least two axial superlayers and any shared hits occur only in the innermost of these superlayers. This enhances the acceptance for γ conversions.

The VC track recognition makes two passes through the tracking data. In the first pass only the tracks that are successfully extrapolated all the way to the innermost superlayer are accepted. The longest tracks are found first, then slightly shorter ones, always making sure to avoid duplicate segments of longer tracks that have already been found. This process is repeated until the short SL1 tracks are sought. The second pass is made to pick up those "outer" tracks which failed to reach down to SL1 but nevertheless managed to span at least two axial superlayers, and at least one intermediate stereo superlayer. These tracks may be deep decays, or perhaps the outer part of a split track. The tracks found in this second pass are not used by the vertex reconstruction.

Each track candidate is fitted to a 5-parameter helix model. During the course of this fit, hits are sometimes swapped or dropped. The procedure is crude but fast, and one iteration suffices since the pattern recognition is fairly accurate. The trajectory fit commences by first estimating a momentum based on the slope and curvature provided

by the pattern recognition. A trajectory is established by extrapolating through the magnetic field, starting from the vicinity of the innermost measured hit and proceeding outward as far as necessary.

This analysis uses tracks associated with the primary event vertex and with measured $p_T > 150$ MeV and $|\eta| < 1.75$, where η is the pseudorapidity given by $-\ln(\tan(\theta/2))$ if θ is the polar angle of the measured track with respect to the proton direction. This restriction limits the measurement to well-measured tracks found in a region of high CTD acceptance where the detector response and systematics are best understood.

2.3.5 Vertex-Fitting of tracks

The coordinates of the event vertex are determined using tracks reconstructed with the CTD in a two-stage method based on the simple and full fit perigee techniques [33]. Trajectories that pass preliminary filtering for compatibility with the beamline enter firstly a "simple" fit filter. This solves for the weighted centre of gravity of surviving tracks, periodically discarding tracks which contribute too much to the χ^2 of the fit until the fit quality is acceptable. Each and every track is given a fair opportunity to spawn a vertex containing it. Secondly, using this simple vertex as a starting point, a full non-linear iteration is carried out to solve for the final vertex position. No additional tracks are likely to be discarded at this point. The remaining trajectories are refitted to this vertex and constrained to it.

2.3.6 Reconstructing the Scattered Positron

The most important requirement for identifying a DIS event in the ZEUS detector is the identification of the scattered positron. Several different electron/positron finders, which approach the problem from various different angles, have been designed for use in the ZEUS environment. The default finder used in this analysis is SINISTRA95 [34]. This algorithm is based on a neural network which uses information from the CAL to distinguish calorimeter deposits caused by electromagnetic particles from those due to hadronic activity (which may look rather similar, especially at low energies). A

neural network is used to find the optimal variables and cuts in a multidimensional space to be used to separate distinct distributions. Energy deposits are found using a clustering algorithm based on the idea that a shower of particles leaves an energy deposit shaped like an island, that is, a central energetic bump surrounded by lower energy deposits. These clusters are classified according to whether they were generated by electromagnetic or by hadronic activity. The electromagnetic deposits are assigned a 'positron-probability', denoting the estimated probability of their having been generated by the scattered positron. A cut on this probability allows a clean identification of the scattered positron. In this analysis, positrons are accepted from SINISTRA with a positron-probability greater than 0.9. The scattering angle of the positron is determined through measurement of its impact position on the inner face of the CAL and reconstruction of the event vertex. The impact position is reconstructed using information from the CAL or the SRTD. Where information from both is available, the SRTD reconstruction is used. The calorimeter cells associated with the scattered positron can be flagged; all other energy deposits are then assumed to be from the hadronic system.

2.4 Summary

The operation of the HERA accelerator has been outlined. The ZEUS detector has been described with particular reference to the characteristics of components pertinent to this analysis. An account has been given of the process of data-taking and basic event reconstruction in the ZEUS environment.

Chapter 3

Calibration of the Central

Tracking Detector

The Central Tracking Detector is used to reconstruct the momenta of charged particles passing through it. The efficiency and accuracy of the reconstruction depend on correct calibration of the detector. In this chapter an iterative algorithm for calibrating the CTD r-ϕ system based on the least squares method [35] is described. The results of tests of its operation, reliability and compatibility with results from the existing calibration method are presented.

3.1 The Calibration Constants

The operation of a drift chamber is based on the principle that a highly energetic charged particle passing through a gas volume will ionise gas molecules along its path. An electric field is applied across the cell so that any electrons liberated in an ionisation process accelerate towards the anode sense wire, gaining energy and causing further ionisations. Thus a few ionised electrons rapidly multiply in the electric field and develop an avalanche towards the wire. The movement of the avalanche of electrons, and of the positively-charged ions in the opposite direction through the field induces a signal in the sense wire which can then be read out. The time taken for the ionisation to drift onto the sense wire, the drift time, is the only free variable required for reconstruction of

the position of the 'hit' - that is, the position at which the ionising interaction took place - providing three constants describing the behaviour of the detector are known. These calibration constants and their inclusion in the reconstruction are described below.

Drift time offset, t_0

Drift time is measured relative to the bunch crossing time defined by the HERA clock, and so includes the time taken for a signal to propagate through the CTD wires and electronics. Also any fluctuations around the assumed collision time caused, for instance, by the finite length of the proton bunch will be included in the measured drift time. In order to determine the true time of drift a time offset, t_0, to the measured drift time must be taken into account.

Drift velocity, v_0

If the true drift time t_i for a hit i is known, the drift distance μ_i between the sense wire and the position of the hit can be calculated via a time-distance relationship

$$\mu_i = \int_0^{t_i} v(t)dt$$

where $v(t)$ is the drift velocity at a distance corresponding to drift time t_i from a particular sense wire and must be found by calibration. The calibration method described in the next section assumes a constant drift velocity, v_0, throughout the drift volume such that $\mu_i = v_0 t_i$.

Lorentz angle, θ_L

The CTD reconstruction makes use of the planar drift approximation [36] in which ionisation drift is assumed to take place in a plane of negligible thickness. Hence, having once determined the distance of drift, the only remaining information needed to calculate the position of the hit is the angle of drift of the ionised electrons. This is measured as θ_L, known as the Lorentz angle: the angle between the electric field vector and the direction of drift of electrons in the crossed electric and magnetic fields. Using the Lorentz equation for the motion of a charge through crossed electric and magnetic

fields, it can be shown [37] that the drift velocity of the particle can be expressed in the form :

$$\mathbf{v_0} = \frac{\mu}{1 + \omega^2\tau^2} \left(\mathbf{E} + \frac{\mathbf{E} \times \mathbf{B}}{B} \omega\tau + \frac{(\mathbf{E} \cdot \mathbf{B}) \cdot \mathbf{B}}{B^2} \omega^2\tau^2 \right) \tag{3.1}$$

where ω is the Larmor frequency, $\omega = -\frac{e\mathbf{B}}{m}$, τ is the mean time between two collisions in the drift gas, and $\mu = \frac{e\tau}{m}$ is the electron's mobility. This equation does not hold in all cases, since its derivation includes the assumption that $v_0 \propto \mathbf{E}$ - an assumption which is not true in the case of operation in the CTD where the drift velocity is saturated - however it is a useful general approximation for calculations involving the Lorentz angle. If, for instance, the fields are simplified to $\mathbf{E} = (E_x, 0, 0)$ and $\mathbf{B} = (0, 0, B_z)$ as the design of the ZEUS CTD intended, then the drift velocity is

$$v_x = \mu E_x \frac{1}{1 + \omega^2\tau^2}, \ v_y = -\mu E_x \frac{\omega\tau}{1 + \omega^2\tau^2}, \ v_z = 0 \tag{3.2}$$

indicating that $\tan\theta_L \propto \mathbf{B}$.

To summarise: in order to reconstruct the position of a particular hit, the measured drift time is used in conjunction with three calibration constants t_0, v_0, $\tan\theta_L$.

3.2 Calibration Method

The aim of the calibration method is to find the values of the calibration constants which, when used in the reconstruction, produce tracks which best fit the observed hits. This is accomplished by the implementation of a least squares minimisation of the hit residuals for each track, where the residual for a hit i, δ_i, is the distance between the hit and the track reconstructed without that hit.

The residual has a sign depending on which side of the reconstructed track the hit falls, as illustrated in figure 3.1. Hits at azimuthal angles above the sense wire plane are defined to have positive drift distances and those at angles below the sense wire plane to have negative drift distances. Hence hits at azimuthal angles above tracks have positive residuals, and those below tracks have negative residuals.

The effect on a hit residual, δ_i, due to miscalibrations of the constants has the form [36]:

$$\delta_i = v_0\delta t_0 + t_i\delta v_0 + |\mu_i| \cot\psi_i' \delta\theta_L \tag{3.3}$$
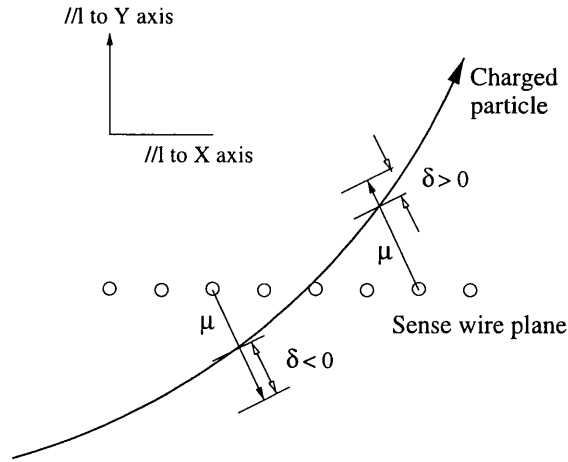
Figure 3.1: Definition of the residual.

where

t_i = drift time for the ith hit;

μ_i = drift distance of the ith hit;

ψ' = angle between nominal electron drift direction and track;

$\delta t_0 = t_0' - t_0^{true}$ = difference between the value of t_0 used and the true value;

$\delta v_0 = v_0' - v_0^{true}$ = miscalibration of v_0; and

$\delta \theta_L = \theta_L' - \theta_L^{true}$ = miscalibration of θ_L

The δt_0 and δv_0 terms denote the error in the reconstructed position resulting from the assumption of a linear time-distance relationship. The $\delta \theta_L$ represents the error in the hit's position caused by reconstructing using the wrong angle of drift. Figure 3.2 shows how a miscalibration in θ_L of $\delta \theta_L$ leads to an extra contribution to the residual of magnitude $\mu \cot \psi' \delta \theta_L$.

The calibration algorithm sums over the total number of hits on a track the squares
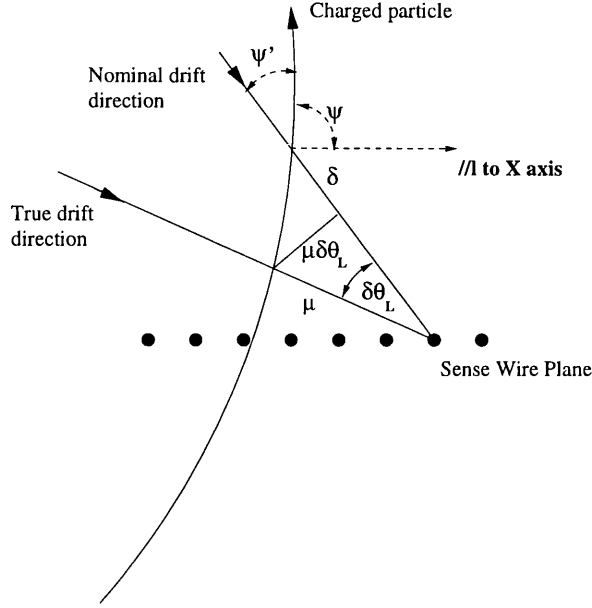
Figure 3.2: Contribution to the residual from a miscalibrated Lorentz angle.

of the residuals weighted by their errors,

$$S = \sum_{i=1}^{n} (\frac{\delta_i}{\sigma_i})^2 \qquad (3.4)$$

and then minimises S, i.e. looks for solutions of

$$\frac{\partial S}{\partial t_0} = 0, \quad \frac{\partial S}{\partial v_0} = 0, \quad \frac{\partial S}{\partial \theta_L} = 0 \qquad (3.5)$$

If the differences between the reconstructed and the true calibration constants are assumed to be small, then a Taylor expansion can be made of equation 3.4 and minimisation is equivalent to solving for δt_0, δv_0 and $\delta \theta_L$ in the equation,

$$\begin{pmatrix} \frac{\partial^2 S}{\partial t_0^2} & \frac{\partial^2 S}{\partial t_0 \partial v_0} & \frac{\partial^2 S}{\partial t_0 \partial \theta_L} \\ \frac{\partial^2 S}{\partial v_0 \partial t_0} & \frac{\partial^2 S}{\partial v_0^2} & \frac{\partial^2 S}{\partial v_0 \partial \theta_L} \\ \frac{\partial^2 S}{\partial \theta_L \partial t_0} & \frac{\partial^2 S}{\partial \theta_L \partial v_0} & \frac{\partial^2 S}{\partial \theta_L^2} \end{pmatrix} \begin{pmatrix} \delta t_0 \\ \delta v_0 \\ \delta \theta_L \end{pmatrix} = - \begin{pmatrix} \frac{\partial S}{\partial t_0} \\ \frac{\partial S}{\partial v_0} \\ \frac{\partial S}{\partial \theta_L} \end{pmatrix} \qquad (3.6)$$

Differentiating equation 3.4 and substituting into equation 3.6 gives:

$$\begin{pmatrix} \sum_{i=1}^{n}(\frac{v_0}{\sigma_i})^2 & \sum_{i=1}^{n}(\frac{v_0 t_i}{\sigma_i^2}) & \sum_{i=1}^{n}(\frac{v_0|\mu_i|\cot\psi_i'}{\sigma_i^2}) \\ \sum_{i=1}^{n}(\frac{v_0 t_i}{\sigma_i^2}) & \sum_{i=1}^{n}(\frac{t_i}{\sigma_i}^2) & \sum_{i=1}^{n}(\frac{t_i|\mu_i|\cot\psi_i'}{\sigma_i^2}) \\ \sum_{i=1}^{n}(\frac{v_0|\mu_i|\cot\psi_i'}{\sigma_i^2}) & \sum_{i=1}^{n}(\frac{t_i|\mu_i|\cot\psi_i'}{\sigma_i^2}) & \sum_{i=1}^{n}(\frac{|\mu_i|\cot\psi_i'}{\sigma_i})^2 \end{pmatrix} \begin{pmatrix} \delta t_0 \\ \delta v_0 \\ \delta\theta_L \end{pmatrix}$$

$$= \begin{pmatrix} \sum_{i=1}^{n}(\frac{\delta_i v_0}{\sigma_i^2}) \\ \sum_{i=1}^{n}(\frac{\delta_i t_i}{\sigma_i^2}) \\ \sum_{i=1}^{n}(\frac{\delta_i|\mu_i|\cot\psi_i'}{\sigma_i^2}) \end{pmatrix} \quad (3.7)$$

or in matrix notation, $\mathbf{H}\,\delta\mathbf{a} = \mathbf{q}$.

The calibration was performed by summing over selected hits to evaluate the elements of the matrices $\mathbf{H}$ and $\mathbf{q}$, and solving for δt_0, δv_0 and $\delta\theta_L$. The weights σ_i were all taken to be equal, since to a first approximation they could be assumed to depend on chamber properties rather than being specific to the hits themselves. The suggested changes in the calibration constants were then applied and iterations continued until a stable solution was reached.

The variance in each calibration constant was obtained from the corresponding entry on the main diagonal of $\mathbf{H}^{-1}$ and the covariances between pairs of calibration constants corresponded to the following off-diagonal terms:

$$\mathbf{H}^{-1} = \begin{pmatrix} \sigma(t_0)^2 & & \\ \mathrm{cov}(t_0, v_0) & \sigma(v_0)^2 & \\ \mathrm{cov}(t_0, \tan\theta_L) & \mathrm{cov}(v_0, \tan\theta_L) & \sigma(\tan\theta_L)^2 \end{pmatrix}$$

From these covariances, the correlations between pairs of calibration constants could be determined:

$$\rho_{12} = \frac{\mathrm{cov}(1,2)}{\sigma_1\,\sigma_2}$$

3.3 Testing

3.3.1 Data Quality Monitoring (DQM)

In order to be confident that the CTD is functioning as expected and to recognise problems in its operation swiftly so that as little data as possible is lost or rendered

unusable, it is necessary to monitor the quality of the data as it is being taken. Basic monitoring of the gas pressure and composition can be supplemented by offline checking of track reconstruction from hits measured in the CTD and any changes in the chamber constants used in the track-fitting. An offline job (TCDQM) which performs checks on the efficiencies and chamber constants for each run of data already exists.

The calibration method described above had been shown to work successfully on Monte Carlo data [35]: it was implemented into a DQM-type job in order to undergo further testing on real data in a DQM environment. Physics events were selected using various TLT (Third Level Trigger) bits.

3.3.2 Nominal cuts

In order to avoid the influence of systematic effects, restrictions were placed on the sample of hits used in the reconstruction:

- The residual δ_i was demanded to be < 0.2 cm, corresponding to an approximately 10σ cut on the hit, so that badly reconstructed hits were discarded.

- The number of degrees of freedom of the track used must be greater than 30. Since the tracks are fitted using a 5 parameter helix, this is approximately equivalent to constraining the number of hits on a track to be greater than 35. Hence only hits belonging to reasonably long, well-measured tracks were used.

- Since the algorithm assumes a linear time-to-distance relationship, hits with drift distances which fall outside the region of the drift cell where this approximation is valid were not used. This was carried out by ensuring that $|\mu_i| > 0.8$cm and $\mu_{max} - |\mu_i| > 0.3$cm [35]

- $|z|$ position of the hit must be < 50 cm and only hits found in the first five superlayers were used, to ensure uniformity of the magnetic field. The axial magnetic field has been shown to be uniform to within 2% in this region [38].

The above cuts were applied throughout the following procedure, except for the final section 3.3.7 where the cuts on the z position and superlayer number of the hit were relaxed.
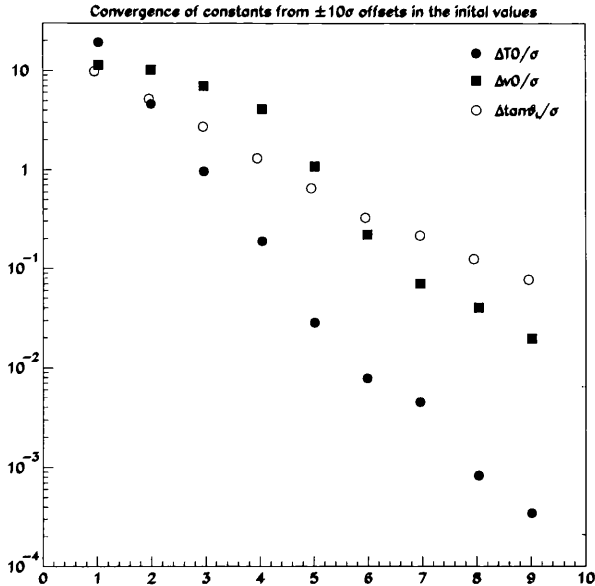
Figure 3.3: Convergence of the calibration constants with iteration.

3.3.3 Convergence Criterion

Tests were performed on the convergence of the algorithm and its dependence on the initial values of the calibration constants with which it was supplied. A first calibration was performed beginning with the normal (reasonable) initial values to check that the calibration constants were within the usual bounds and to find the estimated errors in the constants. Separate subsequent calibration runs were then initialised with $\pm 10\sigma$ shifts in the starting values, and the value of each constant and its error were returned at consecutive iterations. Figure 3.3 shows the variation with iteration number of the difference between the estimated values for t_0, v_0 and $\tan\theta_L$ returned from a calibration starting from a high initial value, x_{high}, and one starting from a low initial value, x_{low}, scaled to their individual errors for that iteration σ_x. i.e. for iteration i, the figure shows

$$\left(\frac{\Delta x}{\sigma_x}\right)_i = \frac{x^i_{high} - x^i_{low}}{\sigma^i_x}$$

where $x = t_0$, v_0, $\tan\theta_L$. The values used for the high and low initialisations, and the results obtained on convergence (taken at the 10th iteration), are tabulated in table 3.1.

Calibration Constant	x_{high}	x_{low}	Value at 10th iteration	$\frac{\Delta x}{\sigma_x}$
t_0 (DSP units[1])	62.0	48.0	54.88 ± 0.73	0.0002
v_0 (cm/ns)	51.80	44.80	48.41 ± 0.35	0.006
$\tan \theta_L$	1.05	0.89	0.973 ± 0.008	0.08

Table 3.1: Table showing convergence from high and low offset initialisation values.

Taking $\frac{\Delta x}{\sigma_x} \sim 0.1$ as a reasonable point at which convergence could be said to have taken place, the values for t_0 appear to converge reasonably fast, v_0 somewhat more slowly, and those for θ_L significantly more slowly. From this slow convergence it can be inferred that $\tan \theta_L$ has only a small effect on the reconstruction of tracks. This is consistent with the shapes of the tracks themselves: long fast tracks are almost straight, and hence have ψ' close to zero so that the Lorentz angle has a very small influence on the direction of electron drift; short slow tracks, on the other hand, are dominated by multiple scattering.

It was concluded that the 10th iteration of the algorithm would be taken as the point of convergence.

3.3.4   Comparison with the existing calibration method

The method of calibration of the CTD in current use (TCDQM) compares the distributions of hit residuals in successively increasing bins of drift time. The mean value of the residual is plotted against the mean drift time and a straight line is fitted. From the intercept and gradient of this line the miscalibrations in t_0 and v_0 are calculated. The Lorentz angle is found in a second step by relating the residual of a hit to its drift distance multiplied by $\cot \psi'$. Two flaws in the above method are that it fails to allow for correlations between the calibration constants, and that there is no straightforward way to estimate the error in the result.

The cuts employed are identical to those used in this study, except that as the TCDQM method finds the Lorentz angle in a separate step from t_0 and v_0, different sets of cuts can be applied for the calibration of the different constants. For instance, the TCDQM method calibrates for t_0 and v_0 using hits from all superlayers, but only

	TCDQM result	This method
t_0 (ns)	23.05	23.00 ± 0.6
v_0 (cm/ns)	48.25	48.24 ± 0.24
$\tan \theta_L$	0.987	0.985 ± 0.016
r-ϕ Physics Resolution (μm)	243	246
r-ϕ Good CTD Res. (μm)	235	240
r-ϕ Peak CTD Res. (μm)	226	230
($z$byT) Physics Resolution (μm)	5183	5108
($z$byT) Good CTD Res. (μm)	5648	5575
($z$byT) Peak CTD Res. (μm)	4652	4655

Table 3.2: Calibration results for Run 13735.

uses hits from superlayers ≤ 5 to calibrate for θ_L.

Results from the two calibration techniques are compared in table 3.2. The quoted resolutions are obtained by fitting a Gaussian to the distributions of residuals of hits on the tracks found using the quoted calibration constants. The different types of resolution are acquired by applying different selection criteria to the tracks considered:

the "Physics" resolution is the resolution of all tracks through the CTD which pass the cuts $|\eta| < 1.5$, $p_T > 200$ MeV;

the "Good CTD" resolution is the resolution of tracks which pass the physics cuts and also have more than 30 degrees of freedom and a probability of more than 0.5 % from the track fit; and,

the "Peak CTD" resolution is found by fitting to the peak of the 'good CTD' distribution and ignoring the tails towards larger residuals.

The comparison is based on a study of 300 events, leading to a total of about 1700 tracks. The values of t_0, v_0 and $\tan \theta_L$ obtained from the two methods are consistent to well within the quoted errors. The r-ϕ resolutions achieved by the TCDQM algorithm appear slightly better than this method, and the z-by-timing resolutions slightly worse, however further studies on different track samples resulted in slightly larger variations

in the values of the resolutions, so this is not a serious discrepancy. The two methods therefore appear to perform equally well.

3.3.5 Comparison between axial and stereo superlayers

The VCTRAK track reconstruction algorithm fits hits to a 5 parameter helix which is projected onto the x-y plane. Since the sense wires in the stereo superlayers are inclined at angles $\alpha \sim \pm 5°$ to the z-direction, this means that distances (and hence the drift velocities) in these layers are scaled by a factor $\cos \alpha$. If these superlayers are to be calibrated, this projection must be compensated for before the matrix elements are calculated.

The scaling was implemented into the calibration code, and an investigation was carried out into whether there were any systematic differences in the resulting values of the calibration coefficients found in the stereo and in the axial superlayers. A calibration was performed once using information from only axial superlayers, once again using only hits in stereo superlayers, and a further time using hits from both types of superlayer. The results are shown in tables 3.3, where only hits from the inner superlayers (1 to 5) were used, and 3.4, where no restriction on superlayer number was employed.

The values obtained for t_0 and v_0 from each type of superlayer are consistent, and the different results for the Lorentz angle are within about 1σ of each other. The electrostatic field in the stereo superlayers is more complicated than that in the axial layers - due to the stereo rotation and the effects of the fields in the surrounding axial layers - which may well give rise to such a systematic effect on the Lorentz angle.

3.3.6 Correlations between Calibration Constants

A sample of tracks selected with the cuts described earlier was calibrated in order to explore the correlations between the calibration constants. Given the time-to-distance relationship employed it was expected that t_0 and v_0 would be inversely correlated, and consideration of the Lorentz equation 3.1 indicated that v_0 and $\tan \theta_L$ would show some small correlation. Results for the correlations obtained from the covariances between pairs of calibration constants are shown in the first column of table 3.5. The expected

	All $\leq$ 5	Axial only $\leq$ 5	Stereo only $\leq$ 5
t_0 (ns)	23.26 ± 0.31	23.20 ± 0.39	23.36 ± 0.50
v_0 (cm/ns)	48.30 ± 0.30	48.28 ± 0.37	48.33 ± 0.49
$\tan \theta_L$	0.9775 ± 0.0039	0.9804 ± 0.0047	0.9717 ± 0.0074
Resolution (μm)	244	243	245

Table 3.3: Calibration results for superlayers $\leq$ 5.

	All	Axial only	Stereo only
t_0 (ns)	23.26 ± 0.25	23.19 ± 0.32	23.35 ± 0.38
v_0 (cm/ns)	48.32 ± 0.23	48.30 ± 0.30	48.36 ± 0.36
$\tan \theta_L$	0.9794 ± 0.0027	0.9817 ± 0.0034	0.9757 ± 0.0046
Resolution (μm)	248	249	247

Table 3.4: Calibration results for all superlayers.

inverse correlation between t_0 and v_0 was indeed patent, but individually t_0 and v_0 showed very little correlation with $\tan \theta_L$. It was deduced [39] that this unexpected result might be a consequence of the cancelling of contributions from positive and negative tracks to the offdiagonal matrix elements (in equation 3.2), since oppositely signed tracks have oppositely signed values of $\cot \psi'$. This deduction was tested by calibrating separate samples of 30000 positive and negative tracks: the results are shown in table 3.5.

The results from positively charged tracks draw attention to a weakness in the method of minimising residuals to calibrate tracks, and incidentally a weakness in this design of drift chamber. Fig 3.4 shows that positively curving tracks may run approximately parallel to the sense wire plane, so that by variation of the value used for t_0 a track can be fitted well through these points with exceedingly small residuals despite using the wrong value of the Lorentz angle. This effect is manifest in a Lorentz angle which appears much lower than the correct value, and a correlation between t_0 and $\tan \theta_L$.

The correlation between v_0 and $\tan \theta_L$ is thought to arise from their relationship

	Both signs	Negative tracks	Positive tracks
t_0 (ns)	23.3 ± 0.6	23.3 ± 0.8	23.0 ± 0.9
v_0 (cm/ns)	48.3 ± 0.2	48.3 ± 0.3	48.1 ± 0.4
$\tan \theta_L$	0.979 ± 0.003	0.988 ± 0.005	0.958 ± 0.005
Resolution (μm)	248	264	236
$\rho(t_0, v_0)$	-0.97	-0.93	-0.95
$\rho(t_0, \theta_L)$	-0.026	0.018	-0.093
$\rho(v_0, \theta_L)$	-0.004	-0.27	0.28

Table 3.5: Calibration results for positive and negative tracks.
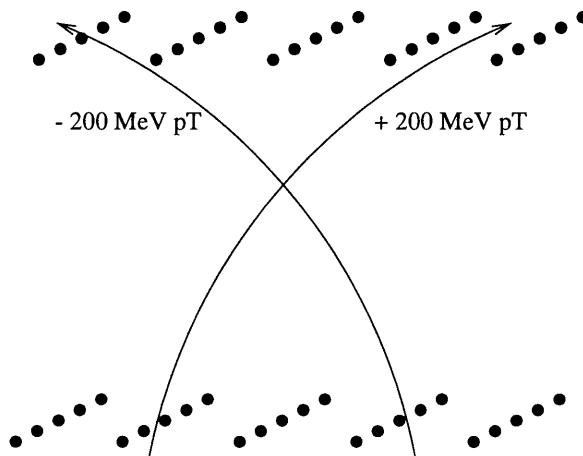
Figure 3.4: Illustration of positive and negative tracks through the CTD.

via the Lorentz equation: from equation 3.2 for perpendicular electric and magnetic fields, it can be shown that $v_0 \propto \cos \theta_L$.

3.3.7 Magnetic field effects

The layout of the CTD is such that tracks towards the edges and corners of the chamber experience variations in the magnetic field from the solenoid, which may lead to variations in the value of the Lorentz angle in such regions of the chamber. Figures 3.5 and 3.6 show maps of the radial and axial magnetic fields in the CTD.

As the radial magnetic field becomes non-negligible it produces an extra component of drift in the z-direction. Corrections are made in the track reconstruction for the effect of this z-drift on the drift distance, Lorentz angle and calculated drift velocity. Previously in this chapter the quoted values of $\tan\theta_L$ have in all cases been for θ_L projected onto the x-y plane; once the radial magnetic field becomes non-negligible this is no longer a good approximation, and the component of Lorentz drift in the z-direction must also be taken into account.

In order to test the effectiveness of the corrections, the calibration was performed on tracks falling within $1.12 < |\eta| < 1.46$ in the outer axial superlayers of the CTD (i.e. in the far corners), where the greatest magnetic field effect would be anticipated.

The results are shown in table 3.6, and demonstrate that the corrections are successful to a large extent in correcting $\tan\theta_L$ back to the nominal value to within a few %, but that some fine-tuning (for instance in the parametrisation of the radial magnetic field) might improve the reconstruction still further.

These results also illustrate that the cuts on superlayer ≤ 5 and $|z| < 50$ cm, traditionally applied to ensure a uniform magnetic field, can be somewhat relaxed, since the track reconstruction is reliable to a good approximation even in these corners of the CTD.

Calibration	$-1.46 < \eta < -1.12$		$1.12 < \eta < 1.46$	
constant	without correc[ns.]	with correc[ns.]	without correc[ns.]	with correc[ns.]
$t_0(ns)$	22.7 ± 2.0	22.6 ± 2.2	23.1 ± 1.2	23.0 ± 1.3
v_0 (cm/ns)	47.7 ± 1.7	48.1 ± 1.9	47.8 ± 1.1	48.1 ± 1.1
$\tan\theta_L$	0.772 ± 0.023	0.942 ± 0.025	0.818 ± 0.013	0.952 ± 0.014

Table 3.6: Calibration values from corners of the CTD.
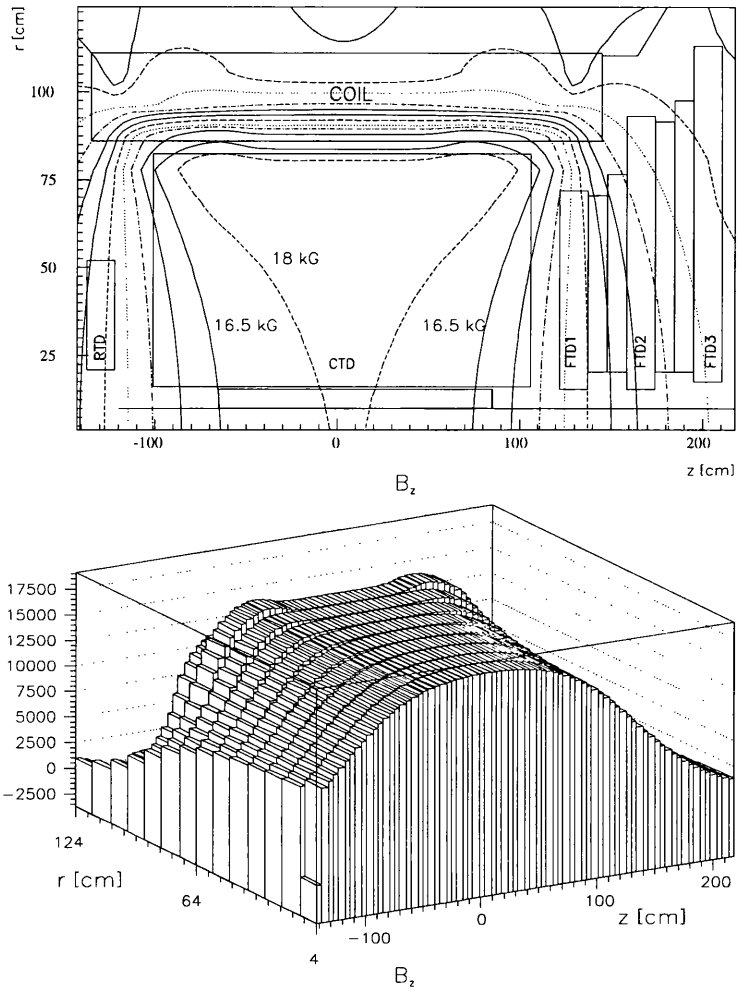
Figure 3.5: Axial field B_z as contour lines and in a perspective view. The lines are $1.5kG$ apart from each other. The field is $18kG$ at the centre of the coil.
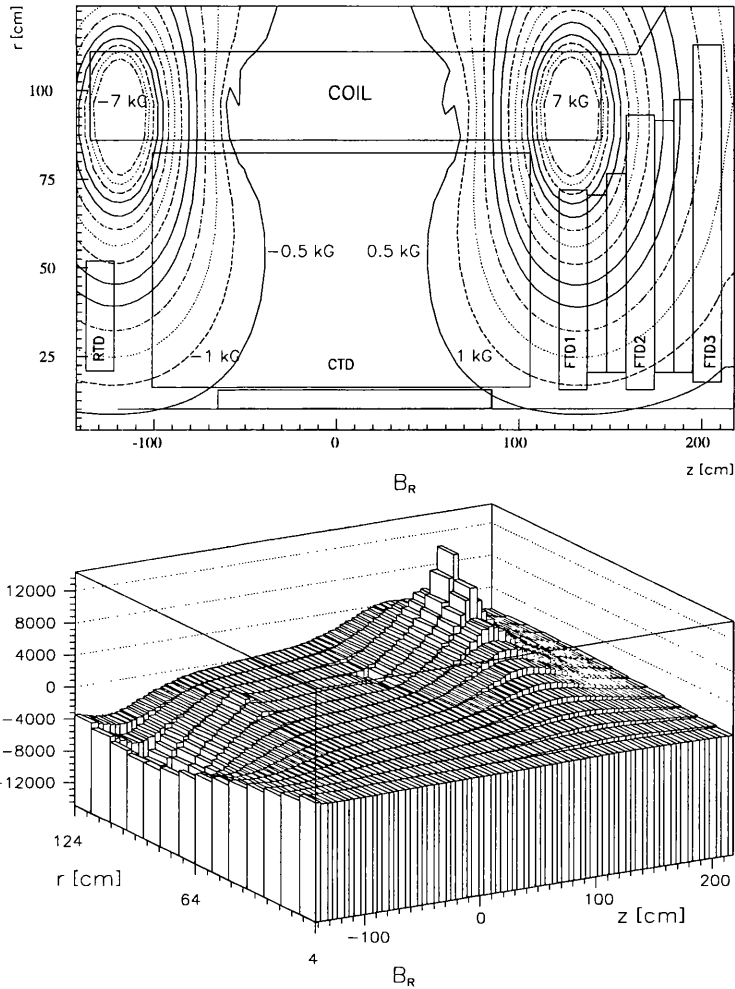
Figure 3.6: Radial field B_r as contour lines and in a perspective view. The lines are 0.5 kG apart from each other. Up to 7 kG can be observed in the detector near the end of the coil.

3.4 Summary

Studies have been made of the calculation of three calibration constants of the CTD. The calibration method has been shown to converge swiftly and efficiently and to give values consistent with existing calibration methods. The technique has been extended for use on stereo superlayers. Results from the calibration technique have been used to investigate the correlations predicted to exist between the calibration constants and to probe the effectiveness of corrections applied in the track reconstruction to deal with variations in the magnetic field strength within the CTD.

Chapter 4

Event Reconstruction and Selection

In this chapter the event reconstruction and selection techniques are discussed. The online and offline triggers use different methods of reconstructing the kinematic variables of the event in order to ensure that the event is indeed NC DIS. These reconstruction methods, and their use in reducing backgrounds to the process under study, are described. The kinematic bins used in the analysis are introduced and the results of an investigation of acceptance are reported.

4.1 Outline of the Data Selection

The selection procedure applied to the data at the TLT is relatively loose, since some information is as yet unavailable at that level. Therefore, when the full offline reconstruction of events is carried out, filters consisting of more sophisticated combinations of cuts are applied to label the data tentatively by the area of physics interest they may lie in and to reduce the levels of background further. These are the DST (Data Summary Tape) bits.

The data from 1994, 1995 and 1996 used in the analysis were required to satisfy DST bit 18, which has been formulated to recognise events displaying the characteristics of Neutral Current DIS interactions. The 1997 data were required with DST bit 12, which

chooses events with the signatures of high Q^2 DIS events. The definitions of the cuts applied in these preselection bits are given in appendix A.

In order to obtain a fiducial sample of data for this analysis, a final pass through the data passing the DST bits was performed in which the selection criteria were tightened further. Here, detailed information about the behaviour of the detector - for instance, studies leading to the identification of noisy cells in the calorimeter [40, 41, 42] - could be used. The nomenclature, the motivation behind the definition of the selection criteria, and the procedure by which the selection was carried out, are described in the following sections.

4.2 Reconstruction of Kinematic Variables

The interactions between particles cannot be observed directly: instead the experimental physicist must reconstruct the interaction as best he can from the experimentally-observable evidence in the final state. A DIS interaction can be fully described with the help of various Lorentz scalars. The Quark Parton Model picture of DIS is shown in figure 4.1. The four-momenta of the incoming positron, incoming proton, exchanged photon and outgoing positron are denoted by k, p, q and k' respectively. A DIS interaction can be characterised using combinations of Lorentz scalars, which are constructed from these four-momenta.
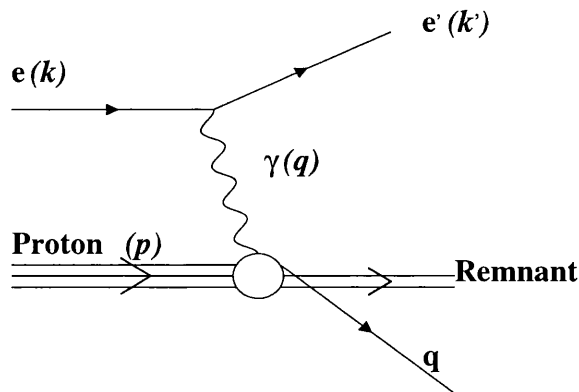
Figure 4.1: QPM Diagram of a DIS event.

The total centre-of-mass energy squared, s, is fixed by the incoming beam energies:

$$s = (k+p)^2 \simeq 4E_eE_p,$$

where E_e and E_p are the incoming positron and proton beam energies. HERA nominally runs with beam energies of $E_e = 27.5$ GeV and $E_p = 820$ GeV, resulting in a value of $s = 90200$ GeV^2.

Other relevant variables are Q^2, x and y, where $Q^2 = xys$ (in the massless approximation):

$$Q^2 \equiv -q^2 = -(k-k')^2 \text{ , the negative square of the four-momentum carried by}$$
the exchanged boson;

$$x = \frac{-q^2}{2p.q} \text{ , the Bjorken scaling variable, equivalent to the fraction of the proton's}$$
momentum carried by the struck quark; and

$$y = \frac{p.q}{p.k} \text{ the fractional energy transfer to the proton in the proton's rest frame.}$$

The ZEUS detector is almost hermetic, allowing reconstruction of these Lorentz scalars in a variety of ways from the energies and angles of the scattered positron (E_e' and θ_e, where θ_e is measured with respect to the proton direction) and of the hadronic system. The hadronic system is characterised by the energies

$$\delta_h \equiv \sum_h (E_h - p_z) \text{ , and } p_{T_h} \equiv \sqrt{(\sum_h p_{x_h})^2 + (\sum_h p_{y_h})^2};$$

and by the angle γ_h, defined as

$$\cos \gamma_h = \frac{p_{T_h}^2 - \delta_h^2}{p_{T_h}^2 + \delta_h^2}.$$

In the naive quark parton picture of DIS γ_h corresponds to the polar angle of the struck quark.

Using all four independently-measurable quantities would over-constrain the kinematic variables - most of the Lorentz scalars can be reconstructed with the input of only two of the above quantities - so that a judicious choice must be made of the method of combination of variables which optimises the accuracy, stability and resolution of reconstruction. The methods of reconstruction in general use on ZEUS are outlined below. In general it is assumed that the rest masses of the positron and proton are much smaller than the energies involved and hence can be neglected.

4.2.1 Electron Method

The positron variables, E'_e and θ_e, are measured with high precision and have small systematic uncertainties. The kinematic quantities determined from these quantities are:

$$Q_e^2 = 2E_e E'_e(1 + \cos\theta_e),$$

$$y_e = \frac{p \cdot q}{p \cdot e} = 1 - \frac{E'_e}{2E_e}(1 - \cos\theta_e)$$

and

$$x_e = \frac{Q^2}{ys} = \frac{E'_e}{2yE_p}(1 + \cos\theta_e)$$

This method gives good results at high y where E'_e is significantly different from the positron beam energy E_e, but at low y ($y \leq 0.1$) y_e has both poor resolution and poor stability.

4.2.2 Jacquet-Blondel Method

If the scattered positron is not detected, for instance in photoproduction where it usually escapes down the beampipe, it is necessary to reconstruct the event using solely the hadronic energy flow of the event. The Jacquet-Blondel (JB) method [43] assumes that the transverse momentum carried by undetected hadrons (which follow the positron down the beampipe or are lost through the beam hole in the opposite direction) is negligible. Then:

$$y_{JB} = \frac{\delta_h}{2E_e}, \quad \text{and} \quad Q_{JB}^2 = \frac{p_{T_h}^2}{1 - y_{JB}}$$

At low y (≤ 0.04), y_{JB} has a resolution superior to that in y_e, but Q_e^2 has better resolution than Q_{JB}^2 over the entire kinematic range. The method is further unsuitable because substantial systematic uncertainties are introduced by energy losses in the passive material in front on the CAL and by energy scale uncertainties in the CAL itself.

4.2.3 Double Angle Method

A reconstruction method commonly used in DIS studies in ZEUS is the Double Angle (DA) method [44], which combines the angle of the scattered lepton and the

characteristic angle associated with the final hadronic state, γ_h. The kinematic variables for the event are then given by

$$Q^2_{DA} = 4E^2_e \frac{\sin\gamma_h(1+\cos\theta_e)}{\sin\gamma_h + \sin\theta_e - \sin(\gamma_h + \theta_e)}$$

$$y_{DA} = \frac{\sin\theta_e(1-\cos\gamma_h)}{\sin\gamma_h + \sin\theta_e - \sin(\gamma_h + \theta_e)}$$

This method has the advantage that γ_h depends on the ratio of the measured quantities δ_h and p_{T_h} so that uncertainties in the hadronic energy measurement tend to cancel, leading to a good accuracy of the reconstructed kinematic variables.

4.2.4 'p_T/Σ' Method

The characteristics of the ZEUS detector mean that, while the angle and energy of the scattered lepton are well-measured, those of the hadronic system are much more prone to distortion by the effects of resolution and energy-loss. The p_T/Σ method attempts to correct for this, by first (p_T) balancing the p_T measured in each of the two systems on an event-by-event basis and secondly (Σ) combining the advantages of the electron, JB and DA methods.

In a fully contained DIS event the transverse momenta of the scattered positron and of the hadronic system should balance, if the negligible transverse momentum carried by QED initial state radiation is discounted (since the scattered positron is measured in the CAL, energy from final state QED is generally included in the measured positron energy). For events measured in the ZEUS detector, the positron p_T tends to be precisely measured, while the hadronic p_T is less certain, due to hadronic energy loss down the beam pipe and/or in dead material in front of the CAL, as well as from the finite energy resolution of the CAL. To a first approximation such mismeasurement will affect both p_{T_h} and δ_h in the same way, so that an estimate of the true y of an event is provided by:

$$y' = \frac{p_T^{elec}}{p_T^{had}} \, y_{JB}^{meas}$$

where the unmeasured energy disappearing down the forward beampipe (referred to as the "proton remnant") carried no p_T, and the current jet was well-collimated. However, in standard DIS events there is a colour flow between the current jet and the proton

remnant, so that a significant fraction of the (hadronic) transverse energy flow is spread between the current jet and proton remnant. This fraction increases with γ_h and decreases as the total transverse momentum of the hadronic system increases. The effect can be accounted for using a correction function, F, determined from Monte Carlo and applied to the data on an event-by-event basis. F is parametrised using 2nd order polynomials. The corrected y_{JB} is then given by:

$$y_{p_T} = F(\frac{p_T^{elec}}{p_T^{had}}, \gamma_h, p_T^{had}) \, y_{JB}^{meas}$$

The resolution at high y can be improved by applying the Σ-correction, first introduced in [45] and used by H1 [46, 47], which combines y_{p_T} with y_e :

$$y_\Sigma = y_{p_T} \frac{1}{y_{p_T} + 1 - y_e}.$$

At this stage the best estimate for the transverse momentum of the hadronic system is p_{Te} and for the hadronic sum $\sum_h (E_h - p_z)$ is $2E'_e y_\Sigma$. Hence, the angle γ_h can be recalculated as

$$\cos \gamma_h = \frac{p_{Te}^2 - 4E_e^2 y_\Sigma^2}{p_{Te}^2 + 4E_e^2 y_\Sigma^2}.$$

and the kinematic variables then recalculated via the DA method. This alternative method has been shown to produce a good resolution in x and Q^2 over the full kinematic range.

4.2.5   Summary of Reconstruction Techniques

In view of its proven accuracy and reliability, and of its stability in the face of uncertainties in the calorimeter energy scale, the DA method was adopted as the central reconstruction method for this analysis. Reconstruction of the kinematic variables using the p_T/Σ method was used as a systematic check. The reconstruction of y using the electron and Jacquet-Blondel methods are particularly useful in identifying backgrounds from photoproduction and the effects of noise in the calorimeter; these were made use of in the selection cuts described below.

4.3   Event Selection

In order to choose as pure a sample of DIS events as possible, it is necessary to reject events which may be badly reconstructed or which may arise from background processes. The event selection procedure thus divides roughly into two streams: firstly ensuring that the data were measured when the detector was functioning reliably and in parts of the detector which are well-understood, and secondly that the events fall into a part of the kinematic plane where the likelihood of background is low.

Primarily, events are accepted if a scattered positron and a primary track vertex have been found. These events are then subjected to a several-stage selection procedure which gradually reduces the sample. The selection criteria are described in the following sections.

4.3.1   EVTAKE

The Data Quality Monitoring of the components of the detector makes it possible to recognise swiftly when a component is malfunctioning. Specific runs and ranges of events can be excluded with this information, discarding events when, for instance,

- there were bad modules (i.e. holes) in the CAL, or problems with the CALFLT;

- the CTD voltage was off, or the mixture of gases in the CTD was wrong, or there was too much noise, or a problem with the trigger;

- the SRTD clock was wrong, or there were too many bad channels in the SRTD;

- there were problems with the global triggering.

Generally, such problems may not be noticed at the time of data-taking but show up in offline DQM checks. The data thus affected can then be discarded offline.

4.3.2   Positron Identification

The signature of neutral current DIS events is the presence of the scattered positron in the final state. The detection and accurate reconstruction of this positron is crucial to the analysis. This analysis employs an electron finder SINISTRA95 which is based on

neural network identification of electromagnetic deposits in the calorimeter as described in section 2.3.6. Manifestly, this procedure will be more difficult if the current jet is close to the scattered positron. In figure 4.2 the thin (thick) arrows indicate the direction and relative energy of the outgoing positron (current quark) in a given (x, Q^2) interval delimited by the dashed lines. It can be seen that the topologies of DIS events are generally such that the current jet and scattered positron are well separated from one another. Problems arise however at low x where the current jet is scattered into the rear calorimeter and the positron has a relatively low energy. Positron identification also suffers in the low x and high y region where the electromagnetic showering from π^0 decays in the calorimeter may be mistaken for low energy positrons; this is most likely to occur in photoproduction events where there is no detectable scattered positron. The positron finder functions optimally for scattered positrons with energy > 10 GeV. Photoproduction events with fake positrons were excluded by requiring $y_e < 0.95$.

4.3.3 Hadronic Activity

The uranium calorimeter is subject to constant low-level noise due to emissions from the depleted uranium (^{238}U). This can be mistaken for hadronic activity and distorts the measurement of the angle of the current jet, γ_h, with particular effect at low y_{JB}. In order to avoid this, events were required to satisfy $y_{JB} > 0.04$. As a further measure, noise suppression was applied to remove individual noisy calorimeter cells: EMC (HAC) cells with an energy deposit of less than 60 (110) MeV were discarded from the analysis.

4.3.4 Vertex Position

Measurements of the position of the scattered positron and of track parameters rely on accurate reconstruction of the event vertex. While the majority of the interactions between the proton and positron bunches take place in the vicinity of the nominal interaction point, the backgrounds from upstream beam-gas interactions and cosmic rays typically lead to vertices with more random z-coordinates.

Only events with a z-vertex in the range $-50 < z_{vtx} < 40$ cm were selected. The asymmetry of the cut ensures that contributions from the satellite peak are reduced.
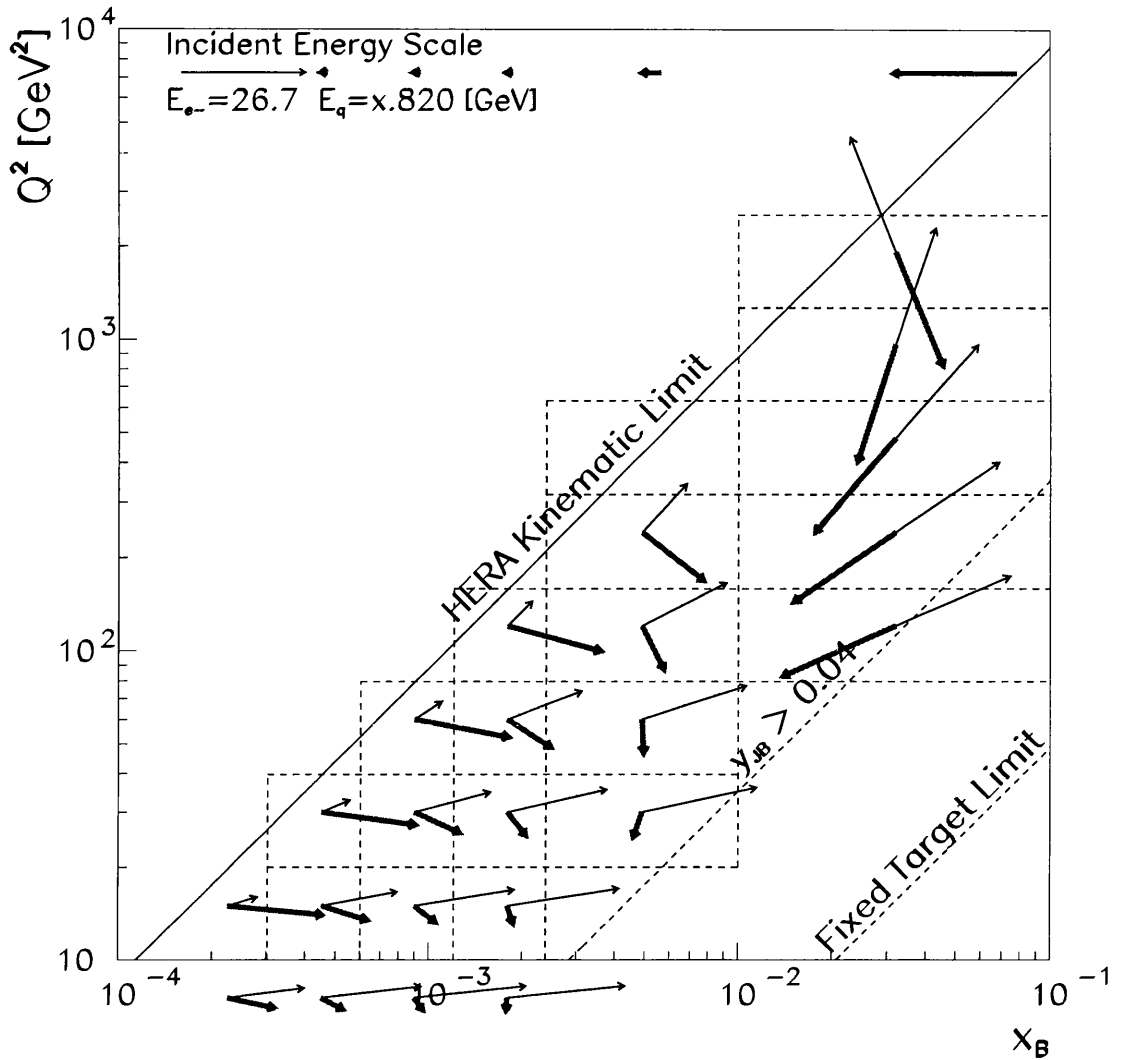
Figure 4.2: QPM directions of the scattered positron and current quark across the kinematic plane.

Also, the radial coordinate of the vertex is restricted to $r_{vtx} = \sqrt{x_{vtx}^2 + y_{vtx}^2} < 10$ cm, a relatively loose cut which ensures that the vertex is reconstructed within the beam pipe.

4.3.5 Beam Gas Suppression

Interactions between the proton beam and gas in the beam pipe, as described in section 2.3.2, can occur anywhere in the beam line. Events that deposit energy in the ZEUS detector in general have vertices ranging from inside the main detector to many metres

upstream (of the order $z = -100$ m). Particles created in such upstream events may deposit energy in the RCAL. Such events will display odd timing characteristics when compared with events occurring inside the detector; that is, the energy will be deposited in the RCAL before the actual bunch crossing occurs. Hence these events can be recognised by employing a method based on the time at which energy was deposited in the CAL. The times of arrival of individual PMT pulses in the FCAL, BCAL and RCAL can be measured: these are denoted as t_F, t_B and t_R respectively. Standard *ep* events with central vertices have $t_F = 0$ ns and $t_R = 0$ ns. Beam gas events with energy in the FCAL are also given $t_F = 0$ ns, but any energy deposited in the RCAL is early by the amount of time taken for the particles to traverse the distance between the RCAL and the FCAL. This is approximately 11 ns. For beam gas events with energy in the RCAL we therefore expect $t_R = -11$ ns. Such events are rejected by requiring $|t_R| < 3$ ns for $E_{RCAL} > 5$ GeV. There is an added restriction on the difference between t_F and t_R which takes into account the non-negligible lengths of the bunches, by requiring $|t_F - t_R| < 5$ ns.

4.3.6 Box cut

In events where the scattering angle of the positron is very small and the scattered positron is measured very near to the beampipe there may be losses from the shower and subsequent degradation to the measurements of the positron's position and energy. In order to be secure that the positron is fully contained when it is measured, the impact point of the scattered positron on the face of the RCAL is required to be outside a square region of dimension 32 cm × 32 cm centred on the beam pipe. Events were required to satisfy the box cut $|x| > 16$ cm and $|y| > 16$ cm.

4.3.7 Suppression of Photoproduction

The quantity $\delta = \sum_i (E - P_z)$, where the sum is over all calorimeter cells i, is expected to be approximately equal to $2E_e$ for well-measured neutral current DIS events, with some variation due to the smearing of energies in the calorimeter. For events where there is initial state radiation, the high energy photon disappears down the beampipe

without being measured and lowers the energy of the incident electron, leading to a considerably lower value of δ. For final state radiation there is no such problem, since the emitted photon tends to be almost collinear with the scattered positron and so is generally included in the measurement of the electromagnetic shower associated with the scattered positron.

For photoproduction events the positron goes down the beampipe, leading to a far far lower value for δ. These events will only be selected if a positron has been faked, for instance by a π^0, in the hadronic final state. Events with $35 < \delta < 60$ GeV were selected.

4.4 Track Selection

This analysis relies on the reconstruction of the tracks of charged particles, hence it is necessary to ensure that the tracks used are those which will be well-behaved and well-measured. Having selected reliable events as described above, reliable tracks are selected within those events using the cuts described below.

CTD active area

The momenta of particles inside the CTD are measured from the curvature of their trajectories. However, if the trajectories curl all the way round so as to form a full circle within the CTD problems may arise with the track-finding. This is prescribed by placing a lower limit on the p_T of the tracks accepted in the analysis: tracks are required with $p_t > 0.15$ MeV.

There are slight fluctuations of the magnetic field within the active volume of the CTD (as shown in figures 3.6 and 3.5); particles with trajectories passing through such areas would be difficult to reconstruct correctly. Also, particles which travel at a small angle to the beamline and just graze the inner superlayers leave few hits behind and thus tend to be poorly reconstructed. In order to avoid these effects accepted tracks are required to pass through at least 3 superlayers and to remain within the regions of the CTD where the magnetic field is at its most uniform, i.e. to satisfy $|\eta| < 1.75$.

Assignment to the primary vertex

The track reconstruction was performed to give two sets of tracks: one set where tracks were required to have been assigned to the primary vertex, and one set consisting of any track reconstructed from the hits in the CTD. The assignment of tracks to the primary vertex provided an extra fixed point to fit to, so disposing of, for instance, tracks from conversions in the beam-pipe walls and synchrotron radiation. Therefore the analysis required tracks from the primary vertex only. These requirements establish a sample of well-measured tracks.

4.5   Current Region Track Acceptances

The selection cuts outlined above result in a restriction of the phase space in the (x,Q^2) plane which is available to be probed experimentally. It is necessary to be aware of such implicitly-imposed limits when deciding on the bin-widths in x and in Q^2 in which the analysis is to be performed. Fig 4.3 shows the areas of the (x,Q^2) plane which are specifically excluded by the event selection cuts. Isolines are shown to illustrate the imposed kinematic constraints in E'_e, y_e, y_{JB}. Also, since tracks in the current region of the Breit frame are close to the direction of the struck quark, isolines of $\eta(\gamma_h) = \pm 1.75$[1] are shown in order to give an impression of the effects of the track selection cuts.

The selected bin sizes were based on those in [48], motivated by the need to have good statistics in each bin and minimal migrations between bins. A correction factor method will be used to correct the data for the event and track selection cuts to regain the full phase space. If this correction method is to be valid, the chosen bins must have high acceptances.

A Monte Carlo study at the generator level was performed in order to check the acceptance of the chosen bins. The acceptance due to the event and track selection cuts was defined for each (x,Q^2) bin as:

$$A(\%) = \frac{\text{No. of tracks reconstructed in current region after event and track selection cuts}}{\text{No. of tracks generated in current region}}$$

---

[1] where $\eta(\gamma_h)$ is the pseudorapidity of the QPM struck quark.

Figure 4.3 shows the (x,Q^2) bins taken into consideration and their acceptances due to the combined effects of the event and track selection cuts.

Current Region Track Acceptances
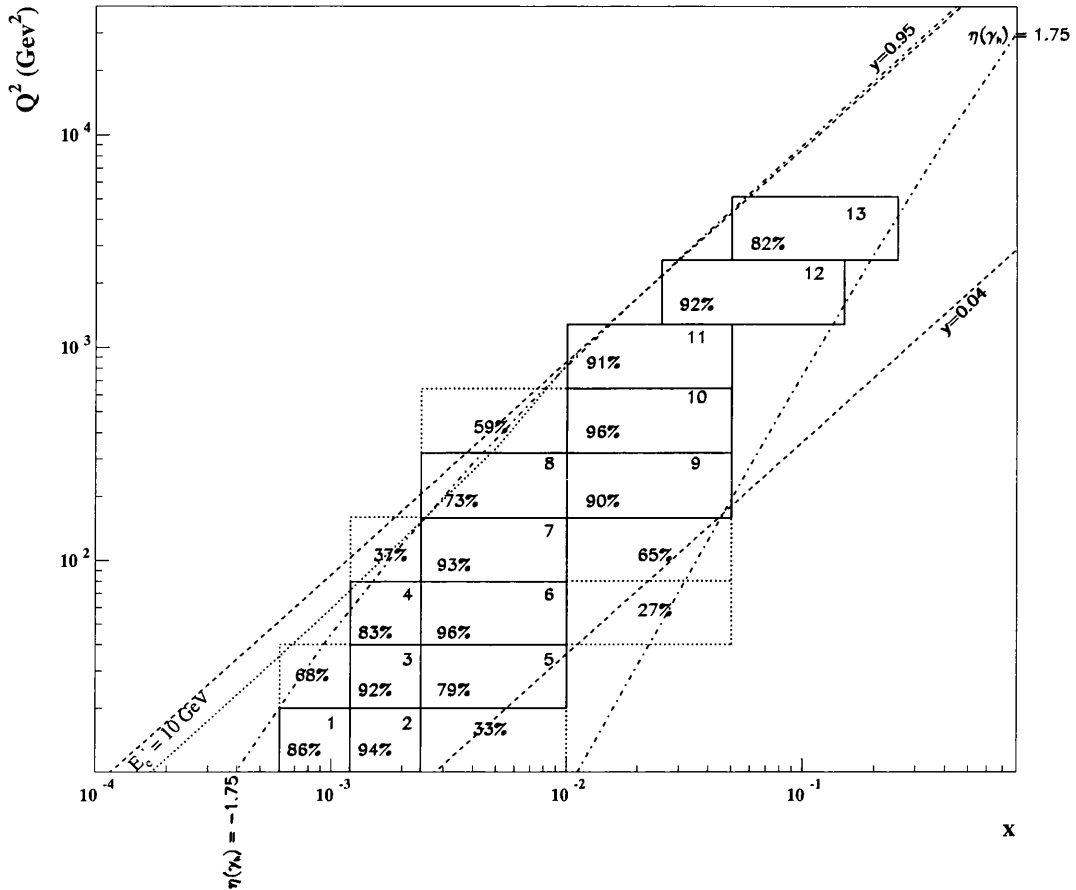
Figure 4.3: Acceptances for the analysis (x,Q^2) bins, calculated using a four-vector Monte Carlo study.

It can be seen that the main restriction on the available phase space is exerted by the $\eta > -1.75$ requirement for events in the lower Q^2 bins, and by the $\eta < 1.75$ requirement for events in the higher Q^2 bins. This corresponds to the change in the topologies of the events as Q^2 increases (as shown in figure 4.2). A lower limit of $\sim 70\%$ acceptance due to the event and track selection cuts was required. The bins thus justified are delineated by solid lines in figure 4.3; they are also numbered (in the top righthand corner) for ease of reference.

In order to ascertain that the kinematic variables are measured without bias and with an accuracy commensurate with the sizes of the bins, an investigation was made into the resolutions in the measurements of x and Q^2 afforded by the Double Angle method within the prescribed bins. For instance, the resolution in x_{DA} was defined for each event as the ratio

$$\sigma(x_{DA}) = \frac{x_{\text{true}} - x_{DA}}{x_{\text{true}}},$$

so that the distribution of $\sigma(x_{DA})$ would be expected to be approximately Gaussian, centred at zero and varying between -1 and 1. Figures 4.4 and 4.5 show the resolutions in x and Q^2 afforded by the DA method in these analysis bins.

4.5.1 Purities and Efficiencies

Monte Carlo which had been through the entire detector simulation was used to calculate the purities and efficiencies of the x and Q^2 reconstruction, where

- the purity for bin i is defined as

$$P_i = \frac{\text{No. events generated and reconstructed in bin } i}{\text{No. events reconstructed in bin } i}; \text{ and}$$

- the efficiency for bin i is defined as

$$\epsilon_i = \frac{\text{No. events generated and reconstructed in bin } i}{\text{No. events generated in bin } i}$$

In general it is hoped that the purity and efficiency for the bin are large ($\gtrsim 50\%$)and approximately equal, indicating that the reconstruction is efficient and the kinematic migrations into and out of the kinematic bins due to inaccuracies in the reconstruction balance fairly well. The results are presented in table 4.1. The purities are consistently $> 50\%$, especially for the higher Q^2 bins, indicating that a small percentage of the events reconstructed in an analysis bin are from outside that bin. However, the efficiencies are rather lower ($\sim 30 - 50\%$) in the low Q^2 bins - significantly so in the bins at low x and low Q^2 - implying that in these regions more events migrate *out of* the bin on reconstruction than migrate *into* it. The effect is particularly apparent in bins 5 and 8, close to the y_{JB} cut.

Bin	1	2	3	4	5	6	7	8	9	10	11	12	13
P (%)	52	54	57	62	73	76	77	78	77	78	82	82	86
ϵ (%)	33	34	43	53	38	69	75	54	78	75	77	81	82

Table 4.1: Purity and efficiency for each analysis (x,Q^2) bin due to the complete selection and reconstruction procedure.

4.6 Summary

The methods of kinematic reconstruction have been described: from these the DA method was adopted as the central reconstruction method for the analysis. An outline is given of the kinematic cuts used to obtain a pure DIS sample. The analysis (x,Q^2) bins, chosen for their high acceptances, are shown. Due to the breadth of the kinematic plane covered by the analysis, it was not possible to keep all events for the full Q^2-range from the data taken in each year. Thus the minimum Q^2-cut was incremented with each data-set analysed to increase the statistics in the poorly-represented phase space at high Q^2. The (x,Q^2) bins chosen for the analysis in [49] have been extended as far as possible into higher Q^2 and x ranges, considering the limitations imposed by falling statistics and the uncertainties in the measurement of tracks in the far forward region.

Therefore, data were accepted with $Q^2_{DA} > 10$ GeV^2 in 1994, with $Q^2_{DA} > 50$ GeV^2 in 1995 and 1996, and with $Q^2_{DA} > 100$ GeV^2 in 1997. The numbers of events in the data samples for each year falling into each bin are presented in table 4.2. The bins are numbered for ease of reference.

Bin no.	x range	Q^2 range (GeV^2)	No. events (DA)				
			1994	1995	1996	1997	Total
1	$0.6 - 1.2\ 10^{-3}$	$10 - 20$	14754	-	-	-	14754
2	$1.2 - 2.4\ 10^{-3}$	$10 - 20$	12708	-	-	-	12708
3		$20 - 40$	8993	-	-	-	8993
4		$40 - 80$	5397	-	-	-	5397
5	$2.4 - 10.\ 10^{-3}$	$20 - 40$	10039	-	-	-	10039
6		$40 - 80$	10066	-	-	-	10066
7		$80 - 160$	5369	13422	17598	-	36389
8		$160 - 320$	1449	3901	5067	-	10417
9	$1.0 - 5.\ 10^{-2}$	$160 - 320$	2266	5733	7528	-	15527
10		$320 - 640$	985	2359	3237	-	6581
11		$640 - 1280$	371	951	1328	-	2650
12	0.025 - 0.15	$1280 - 2560$	196	421	581	1303	2501
13	0.05 - 0.25	$2560 - 5120$	48	149	202	389	788

Table 4.2: The numbers of events reconstructed from each data-set in the analysis (x,Q^2) bins.
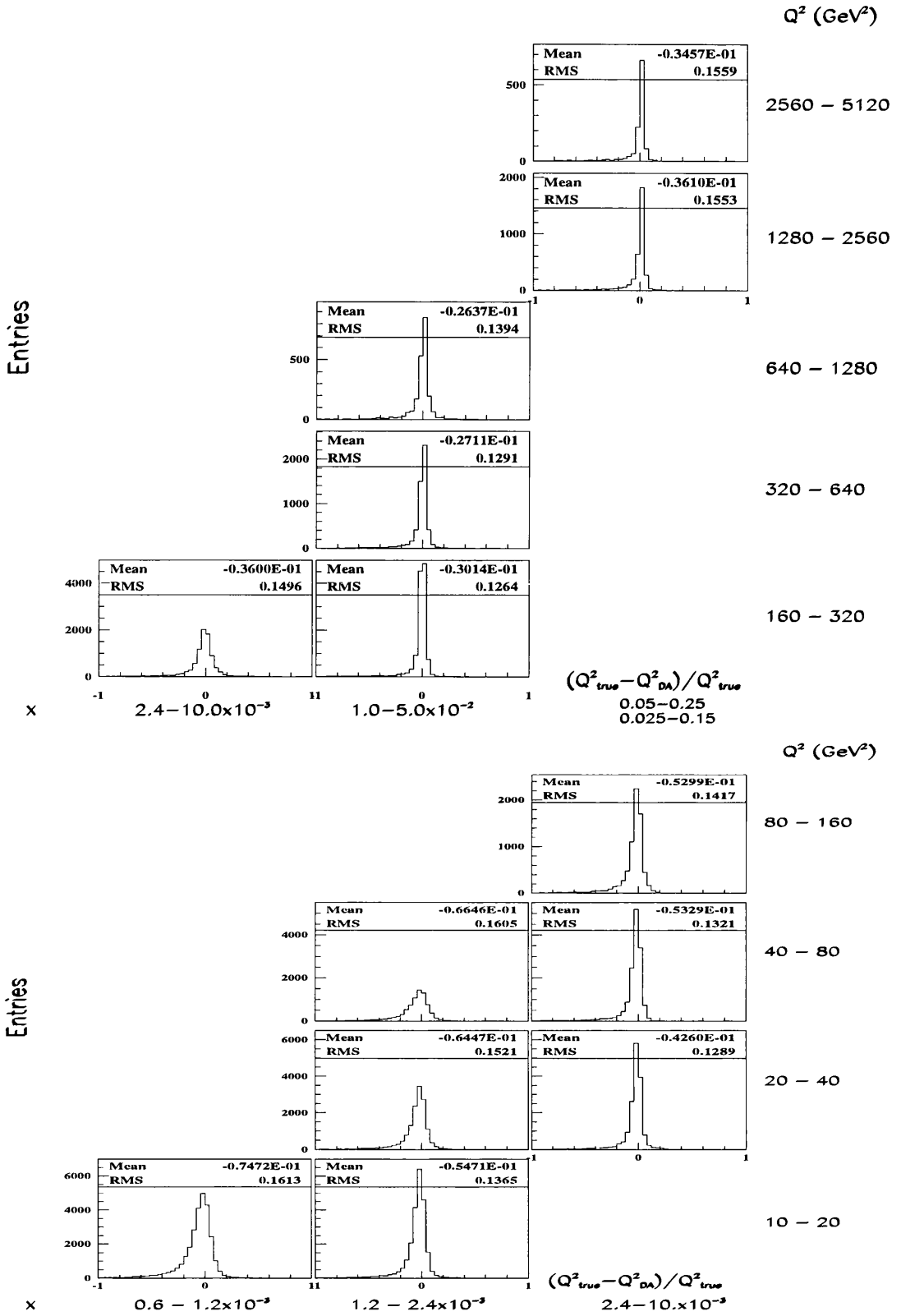
Figure 4.4: Resolution in the measurement of Q^2_{DA} in the analysis (x, Q^2) bins.
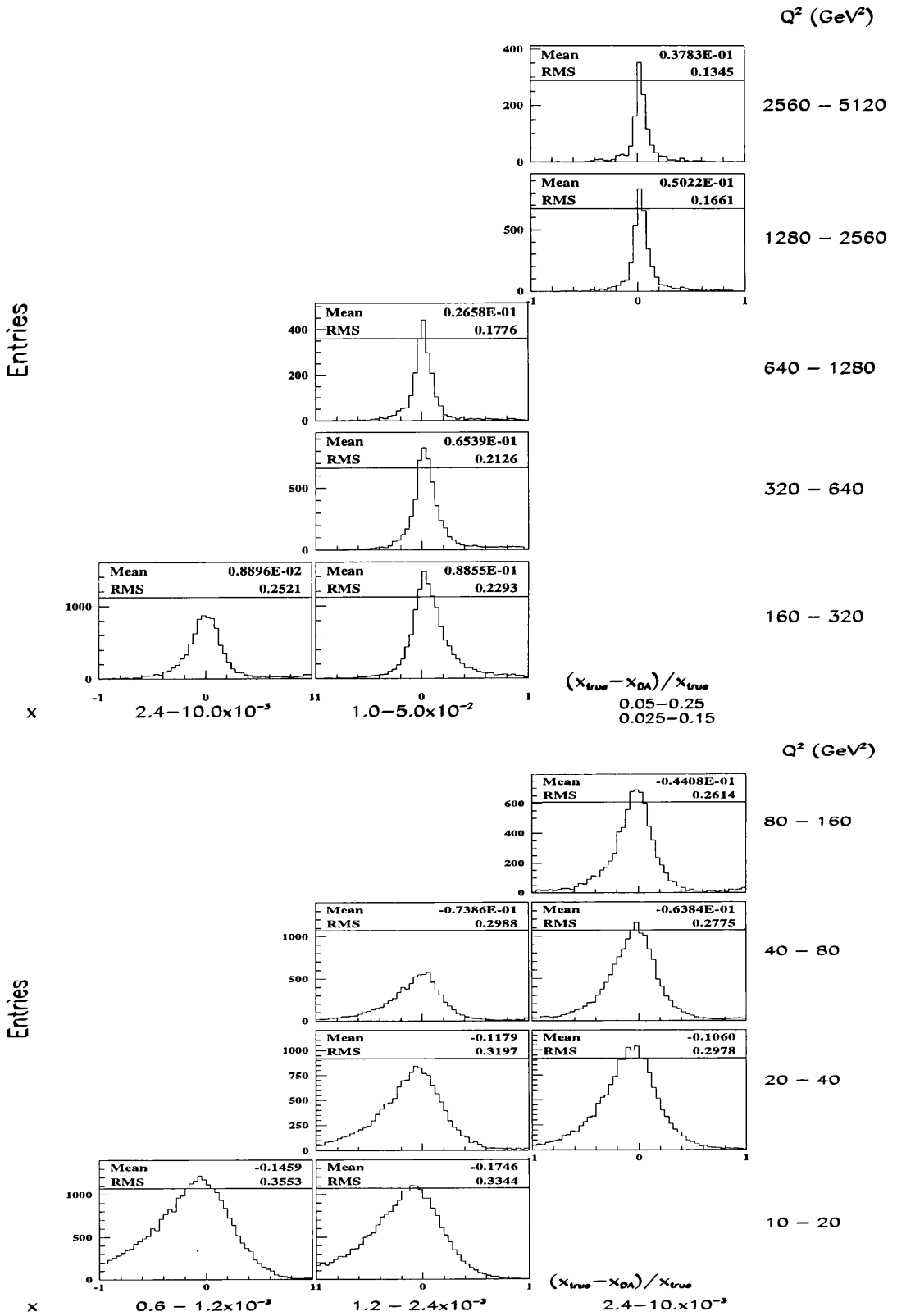
Figure 4.5: Resolution in the measurement of x in the analysis (x,Q^2) bins.

Chapter 5

Event and Detector Simulation

This chapter provides an outline of the techniques used for the simulation of physics interactions and describes the simulation ansatz used for this analysis. Comparisons between simulated and real ZEUS data are shown.

5.1 Introduction

The aim of this analysis is to measure the momentum spectra of final state hadrons in DIS interactions and to compare the results with theoretical predictions. Predicting the final state in DIS is not a straightforward process, even at leading order. Whilst the basic lepton-quark scattering processes have well-defined cross-section formulae, consideration of the higher-order QCD contributions and processes which are not calculable in perturbation theory complicate the picture beyond the reach of analytical methods. This problem can be overcome by the use of Monte Carlo (MC) methods, where random statistically-independent numbers are used to simulate the probabilistic production of particles. The chain of processes employed in this procedure is outlined in the next section.

Monte Carlo techniques are not only used to simulate the physics processes under study, but are also required in describing the experimental measurement. The observed distributions of particles are affected by the resolutions, efficiencies and responses of the detectors used to measure them. In order to make a direct comparison between the theory and the experimental data it is essential to assess and unfold the biasing

effects introduced by the detector. This unfolding can be performed by simulating the physics interactions and treating the results to a simulation of the detector and read-out systems, thus obtaining a sample of mock data in the same format as the real output from the detector which can then be subjected to exactly the same treatment as the real data. This method allows the linking of the ersatz data distributions back to the true distributions which produced them, and thus the investigation of the resolution properties of the detector as we understand it.

5.2 Monte Carlo Models

Monte Carlo event simulation is made possible through the factorization property of perturbative QCD: the property that the different processes in an interaction can be calculated separately and their results convoluted to give the overall result. DIS event simulation can be broadly partitioned into three or more distinct stages: $f \otimes \hat{\sigma} \otimes \mathcal{D}$ as described below.

Parton Distribution Function (PDF), $f(x, Q^2)$

The distributions of the partons inside the proton cannot be calculated, but if the distribution is known at a particular scale they can be evolved to different scales. There are various different phenomenological models for the initial distributions: we use the MRSA [50] and MRSA′ [51] parametrisations of the PDFs, which have been shown to describe well the HERA measurements of the proton structure function F_2 in the (x, Q^2) range of this analysis [52, 53].

Hard Scatter

The hard subprocess cross-section, $\hat{\sigma}$, can be exactly calculated to a defined order in pQCD. The Monte Carlos under discussion here use cross-sections calculated to leading order in QCD, corresponding to the BGF and initial- and final-state QCDC diagrams. Ultimately the data are compared with calculations where the hard cross-section is known to next-to-leading order.

Fragmentation

Following the hard scatter the partons undergo a fragmentation process, $\mathcal{D}$, and eventually produce final-state colourless hadrons. The fragmentation process is itself divisible into the **Parton Showering** and **Hadronisation** processes. The former deals with QCD radiation from the hard partons emerging from the hard scatter, for instance the outgoing hard partons in the leading order DIS diagrams shown in figures 1.3 and 1.4 can continue to radiate gluons and quarks, which in turn can interact further with one another. This fragmentation continues until α_s becomes large and the coloured partons transform into colourless hadrons (which are then free to decay, interact with the detector etc.) in a non-perturbative process: this is the hadronisation process.

In principle, the parton showering fragmentation process can be calculated perturbatively (if the branchings are at a sufficiently hard scale), but in practice it's too difficult to calculate beyond more than a few powers of α_s. However, the probability distributions for the initial and final state parton shower can be evolved between the hard scattering scale and the hadronization scale according to DGLAP evolution, if the probability distributions for the final state particles with respect to their parent partons are known from a phenomenological model.

The hadronization process, which occurs at large values of α_s, cannot even in principle be calculated in pQCD and is modelled phenomenologically. Several different models of the fragmentation process are available on the market: since the analysis is intimately concerned with this process, Monte Carlos implementing two different fragmentation models were used to generate events, thus providing a check for any systematic effect on the measurement arising from the hadronization model. The central corrections to the data were carried out using events generated by a combination of Lund Monte Carlo generators: LEPTO was used to provide the hard scatter with initial-state radiation simulated via DJANGO, ARIADNE to perform the parton showering, and JETSET to carry out the hadronisation. Further Monte Carlo samples were generated using HERWIG, for systematic checks.

The models implemented in these Monte Carlo generators are briefly described below.

5.2.1 Lund String Models

The Lund Monte Carlo family are a set of Monte Carlo generators which all employ a string (or similar) description of the fragmentation process. The Lund string model takes as its basis the assumption of linear confinement. As two partons move apart, the colour field between them is modelled as the stretching of a colour flux tube joining them. The transverse dimensions of the tube are of typical hadronic sizes (~ 1 fm). The tube stretches until its tensile energy is large enough to provide masses for two or more new partons. Eventually all of the coloured partons are associated by strings into colour singlet states which do not have sufficient invariant mass to break apart. These are the final state hadrons. Using various tunable parameters, the Lund string model has proved very successful in describing experimental data.

LEPTO

The LEPTO Monte Carlo [54] can be used to simulate complete events in deep inelastic lepton-nucleon scattering. The parton level interaction is based on the standard model electroweak cross sections, which are fully implemented in leading order for any lepton of arbitrary polarization; different parametrizations of parton density functions may be used. First order QCD matrix elements for gluon radiation and boson-gluon fusion are implemented and higher order QCD radiation is treated using parton showers.

DJANGO

DJANGO [55] is an interface of the Monte Carlo programs HERACLES [56] and LEPTO. It simulates deep inelastic lepton-proton scattering including QED and QCD radiative effects. The use of HERACLES takes into account the complete one-loop electroweak radiative corrections.The LUND string fragmentation as implemented in JETSET is used to obtain the complete final hadronic state.

ARIADNE

A slightly different approach to the problem of describing the partonic final state is provided by the colour dipole model (CDM), implemented in ARIADNE [57]. In this

model the struck quark and proton remnant are considered to form a colour dipole. When this dipole radiates a gluon, it splits into two radiating dipoles: one between the struck quark and the gluon, and one between the proton remnant and the gluon. Repeated gluonic emissions lead to a chain of such dipoles. The implementation of this model for DIS differs from the e^+e^- case in that one end of the dipole system - the proton remnant - is not point-like and must be treated as an extended object. ARIADNE has been very successful at describing ZEUS data [58], [59], and is thus the Monte Carlo event generator of choice for this analysis. Events were generated without contributions from diffractive or F_L components.

RAPGAP

In order to simulate the diffractive contribution to the measurement, a sample of events were generated using the 1994 detector description and the RAPGAP Monte Carlo [60]. This Monte Carlo follows a model by Ingelman and Schlein where the proton couples to a (spacelike) pomeron, and this pomeron consists of partons. The photon coupling to the incoming lepton interacts with partons in the pomeron instead of interacting directly with the partons in the proton. The program calculates the cross-section for the partonic scattering process, which depends on the partonic structure of the pomeron. RAPGAP is used in conjunction with ARIADNE and JETSET, which carry out the parton showering and hadronisation processes.

5.2.2 HERWIG

Unlike the LEPTO model of parton showering, where the struck quark can emit partons before and after the boson vertex, in the HERWIG [61] model the parton shower takes place inside a cone whose angular size is defined by the incoming and outgoing struck parton.

HERWIG is designed to make use of the pQCD "preconfinement property" which states that in hard processes the confinement of particles is local in colour and independent of the hard scale Q. It assumes a cluster hadronization model which is local in colour and independent of the hard process and the energy. After the perturbative parton branching process, all outgoing gluons are split non-perturbatively into light

q-$\bar{q}$ pairs or diquark-antidiquark pairs. In the planar approximation, a colour line may now be followed from each quark to an antiquark or diquark with which it may form a colour-singlet cluster. These low-mass colourless clusters satisfy the "preconfinement' conditions; any heavier clusters are allowed to decay into two lighter clusters in a manner similar to that used in the Lund string fragmentation. The clusters thus formed then decay isotropically to form hadrons.

5.3   Simulation of the Detector

The above Monte Carlo simulations generate the event as far as leptons and hadrons, including relatively short-lived particles such as K^0_S, Λ^0, η etc. The lifetimes of these particles are such that they may decay within the volume of the ZEUS detector. Therefore their interaction with the apparatus must be taken into consideration. This is carried out by MOZART (Monte Carlo for ZEUS Analysis Reconstruction and Trigger) - an extensive software program which uses the GEANT [62] package of detector description and simulation tools and contains a detailed description all the detector component materials and positions. MOZART simulates the passage of generated particles through the ZEUS detector including, for instance, the ionization energy losses in the tracking chambers, the random chance of energy loss into dead material, and the smearing of the energy resolution as a particle showers in the calorimeter. These processes are statistical in nature and handled with random number generation on a probability distribution - thus this is also a Monte Carlo treatment.

The ZEUS detector continues to evolve year by year - for instance, the vertex detector was removed and the presampler inserted in the period between the end of 1995 data-taking and the beginning of the 1996 data-taking - so the description of the detector implemented into the Monte Carlo must be updated annually and Monte Carlo suitable for one year's data does not necessarily suit another year. The specifications and numbers of events in the individual Monte Carlo samples are given in table 5.1, alongside the year in which the data were taken.

The Monte Carlo used to describe data taken in 1997 was generated using the 1996 detector simulation. There was a short break (of the order of 3 weeks) between these

Year	MC Q^2_{min} cut (GeV^2)	No. of events (1000s)	MC generator & PDF
1994	$Q^2 > 3$	800	ARIADNE 4.08 + DJANGO, MRSA
	$Q^2 > 6$	600	ARIADNE 4.08 + DJANGO, MRSA
	$Q^2 > 3$	300	RAPGAP + HERACLES + ARIADNE
	$Q^2 > 4$	200	HERWIG 5.8c, MRSA'
1995	$Q^2 > 40$	380	ARIADNE 4.08 + DJANGO, MRSA
	$Q^2 > 70$	100	HERWIG 5.8d, MRSA
1996	$Q^2 > 70$	200	ARIADNE 4.08, MRSA
	$Q^2 > 70$	100	HERWIG 5.8d, MRSA
1997	$Q^2 > 800$	20	ARIADNE 4.08, GRVHO-94
	$Q^2 > 800$	20	HERWIG 5.8d, MRSA

Table 5.1: The numbers of Monte Carlo events generated for each year's data.

running periods and no explicit changes were made to the detector.

5.4 Monte Carlo Description of the Data

In the following figures the distributions of various global event variables observed in the data are compared with those observed from the central (ARIADNE) Monte Carlo sample described above. All histograms are normalised to the number of events contributing to them. In each histogram the ZEUS data points are denoted by black dots and the Monte Carlo by a histogram (indicating the binwidth). The figures are divided into low, medium and high Q^2 ranges.

5.4.1 Event Variables

The following figures compare the distributions measured in the data and measured in the Monte Carlo of the variables which are used in the event selection procedure. Clearly, it is vital that the Monte Carlo describe these particular distributions well.

Figure 5.1 shows data in the low Q^2 ($10 < Q^2 < 100$ GeV^2) sample. The

distributions are fairly well modelled by the Monte Carlo, although there are slight discrepancies at the lowest Q^2_{DA} and x_{DA}. The spectrum in the corrected energy of the scattered positron shows the kinematic peak at about 25 GeV, and the angle of scatter of the positron is peaked in the backward direction. The slight differences between the y_{JB} distributions may be due to noise in the calorimeter not yet being completely simulated in 1994. The distribution in the $\sum(E-p_z)$ over all calorimeter cells shows the characteristic DIS peak at $2E_e \approx 55$GeV. The z-vertex distribution is slightly shifted towards positive z but is well described by the MC. The $\eta_{\max}$ distribution, where $\eta_{\max}$ is the pseudorapidity of the most forward calorimeter cluster, demonstrates the contribution of large rapidity gap events in this Q^2 range. The inclusion of $\sim 10\%$ RAPGAP events in the Monte Carlo models the shape of the distribution well.

The plots in figure 5.2 are for the medium Q^2 ($Q^2 > 80$ GeV^2) data, comprising events taken in 1995 and 1996. The Monte Carlo reproduces the data excellently except in the $\eta_{\max}$ distribution, where the substantial shortfall of the MC makes it manifest that no suitable diffractive Monte Carlo sample was available in this Q^2 range. A cut applied to exclude diffractive events later shows this not to be a serious systematic effect.

The 1997 data sample was defined with $Q^2_{DA} > 800$ GeV^2. Despite the poor statistics, figure 5.3 shows relatively good description of the data by the Monte Carlo. At such high values of x the events are boosted far forward in the laboratory frame, so that $\eta_{\max}$ is no longer a good yardstick for detecting diffractive events.
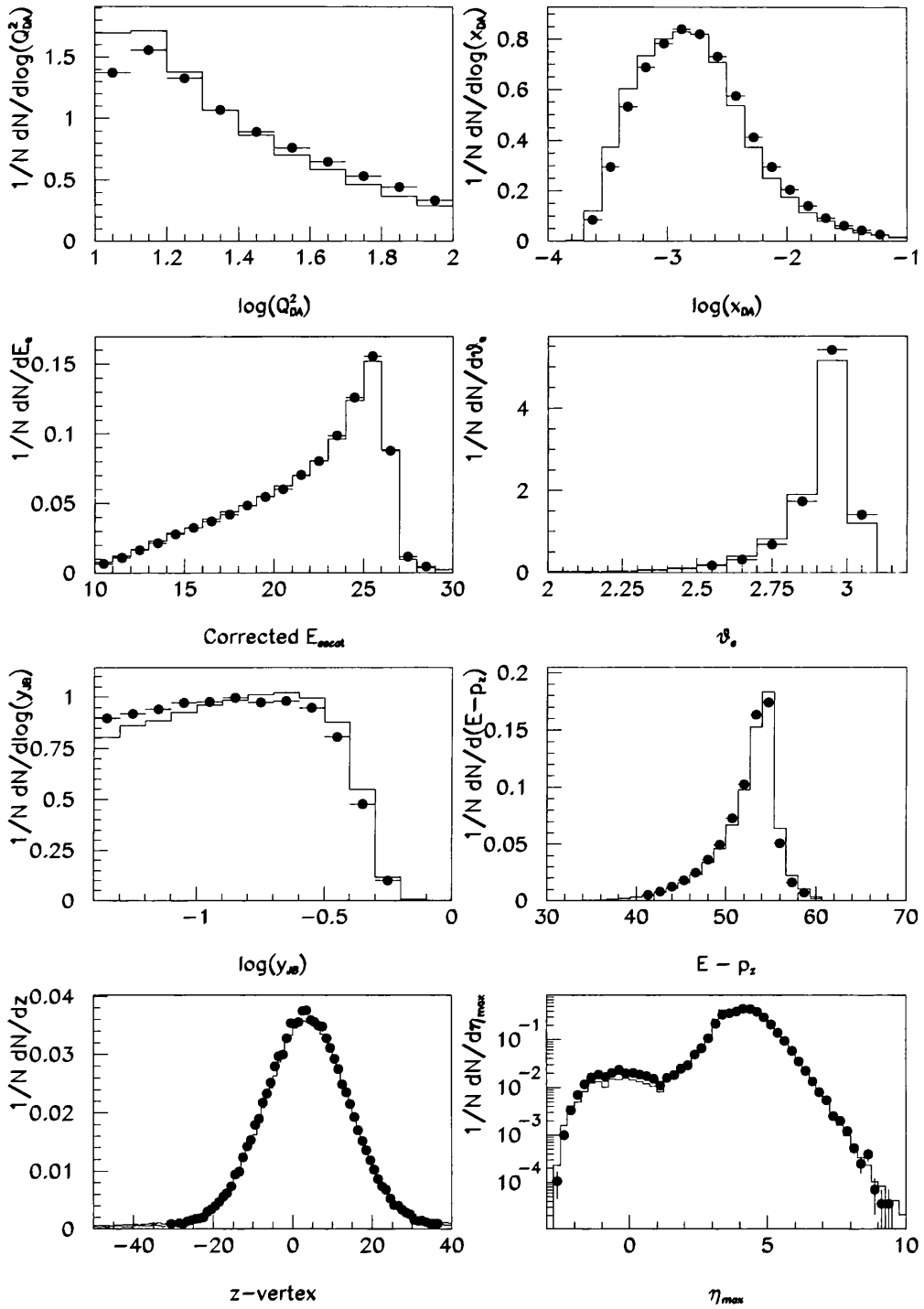
Figure 5.1: Comparison of 94 MC and data event variables.
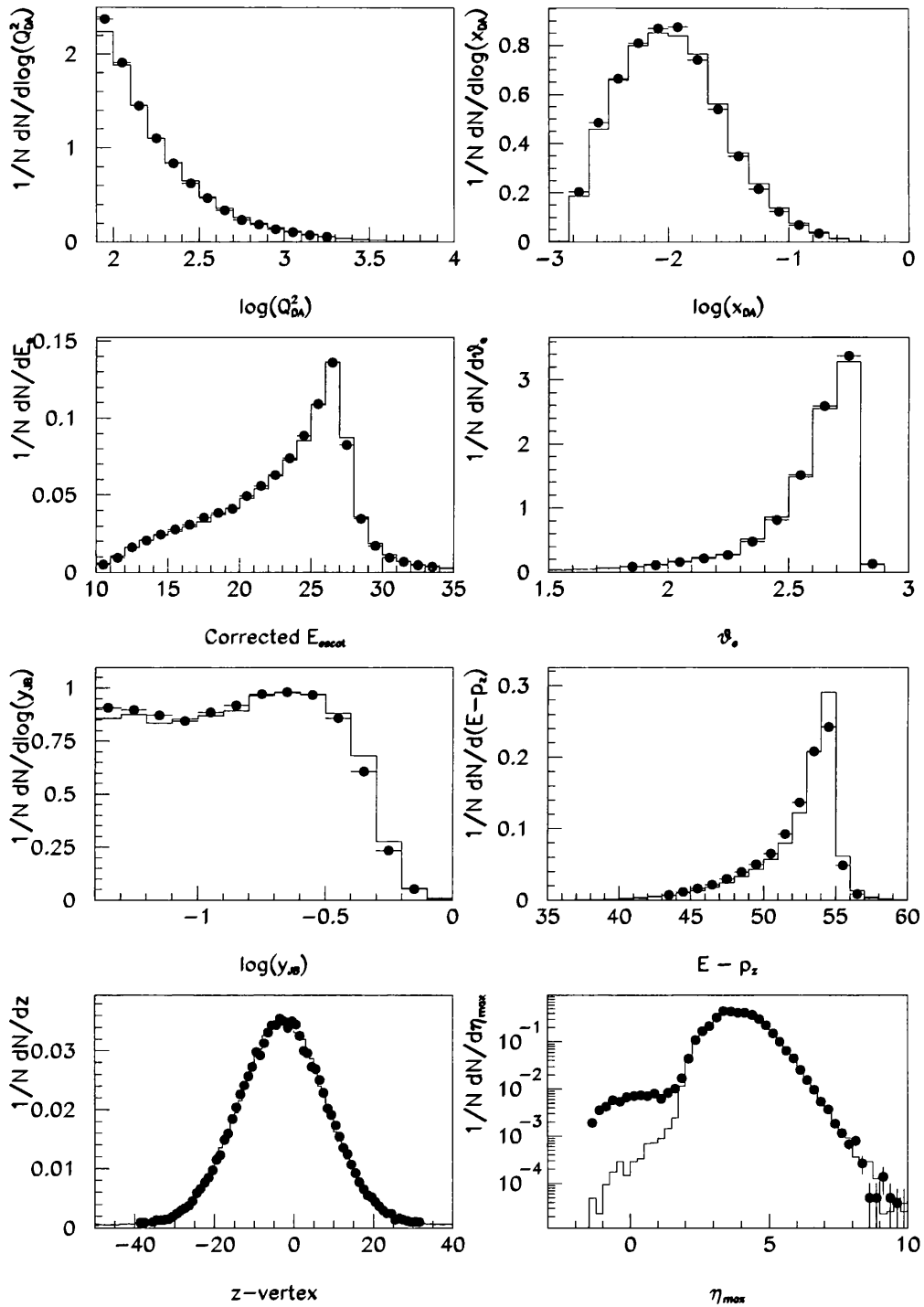
Figure 5.2: Comparison of 95 + 96 MC and data event variables.
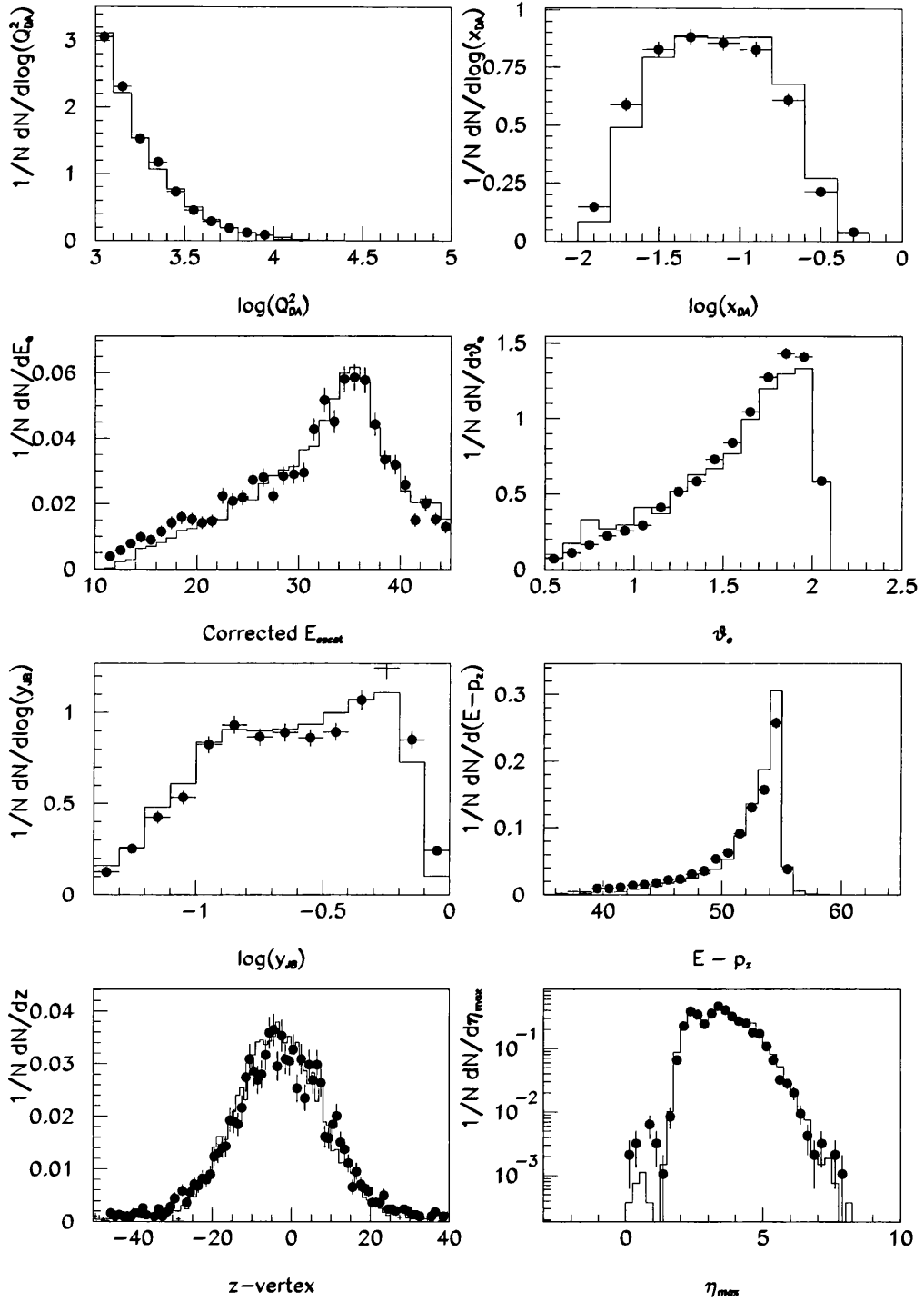
Figure 5.3: Comparison of 97 MC and data event variables.

5.4.2   Track Variables

Since this analysis is based on tracking variables, the agreement between the Monte Carlo description of the tracking and the data was also studied.

Figure 5.4 shows the distributions of various relevant tracking variables obtained from the 1994 data and from the Monte Carlo after the event and track selection cuts. The Monte Carlo undershoots the data slightly in the laboratory variables $\log p_{lab}$ and η, but the effect is not apparent on the p_T^{lab} plot. The distribution of p_z^{Breit} shows that in this Q^2 range the majority of the reconstructed tracks lie in the target region of the Breit frame ($p_z > 0$). The remaining two plots show the distributions in the number of degrees of freedom per track (i.e. the number of points on the track + 5) and the $\chi^2/$ndf of the final track fitted to the points. The distribution of the number of degrees of freedom per track from the data shows nice evidence of the superlayer structure of the CTD. The Monte Carlo is smoother and does not describe the details of the distribution. The distribution of the $\chi^2/$ndf of the tracks is peaked near unity in the Monte Carlo but at far smaller values in the data, indicating that the track errors are significantly overestimated in the track reconstruction. It would seem that, while the Monte Carlo may describe the gross tracking parameters fairly well, the errors are typically underestimated by a factor 2. It should be noted that cuts on error quantities are avoided in the track reconstruction and no explicit cuts have been made on the values of these latter two quantities.

In figure 5.5 the Monte Carlo describes the data very well (apart from the track χ^2 distribution). The appearance of superlayer structure in the track ndf plot indicates the improvements made in the Monte Carlo description of the tracking after 1994.

The data points in figure 5.6 are limited by poor statistics, but the agreement seems fairly good. However it is apparent that the ARIADNE MC may require tuning in this region of high Q^2 in order to reproduce the observed multiplicity.
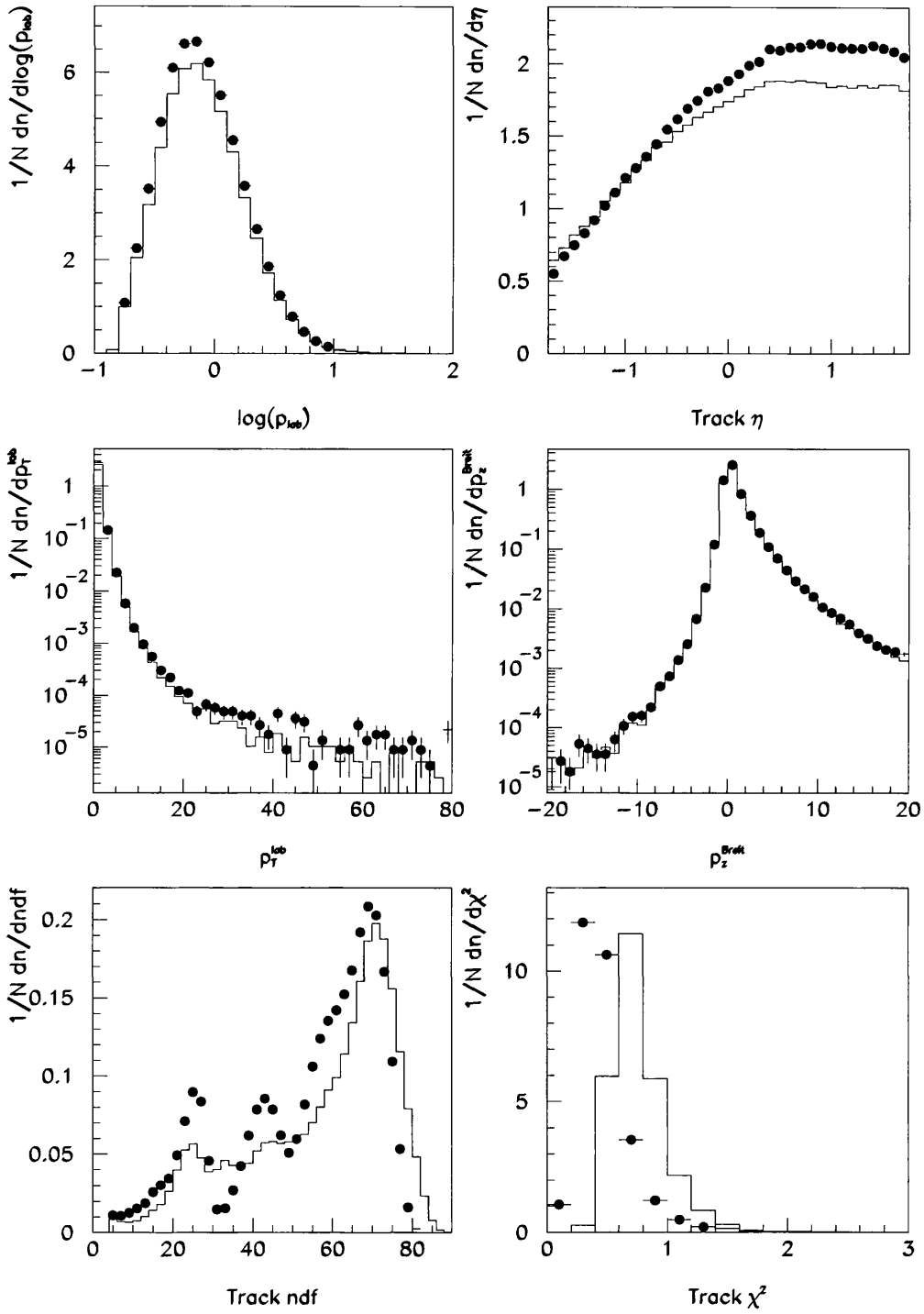
Figure 5.4: Comparison of 94 MC and data track variables.
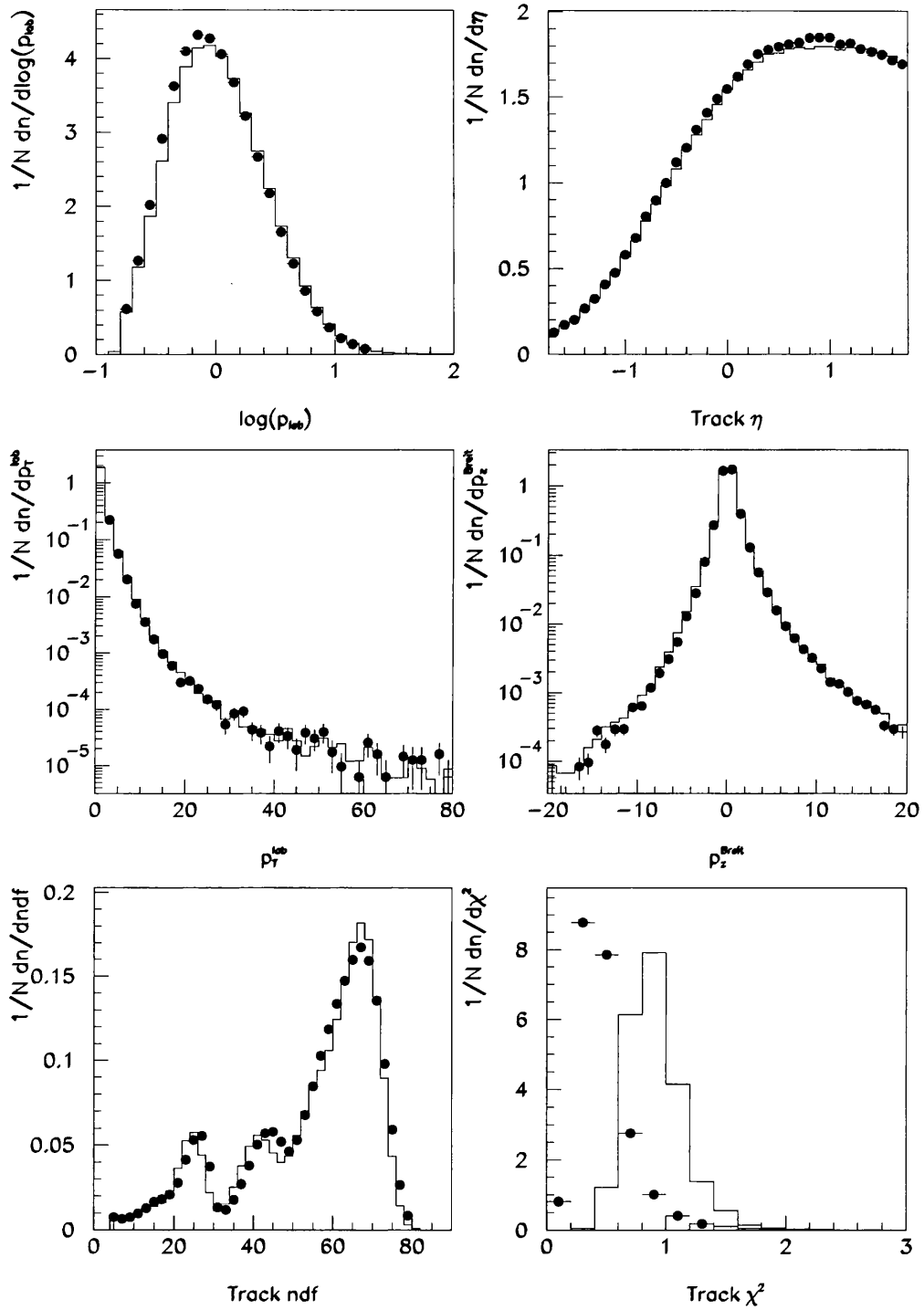
Figure 5.5: Comparison of 95 + 96 MC and data track variables.
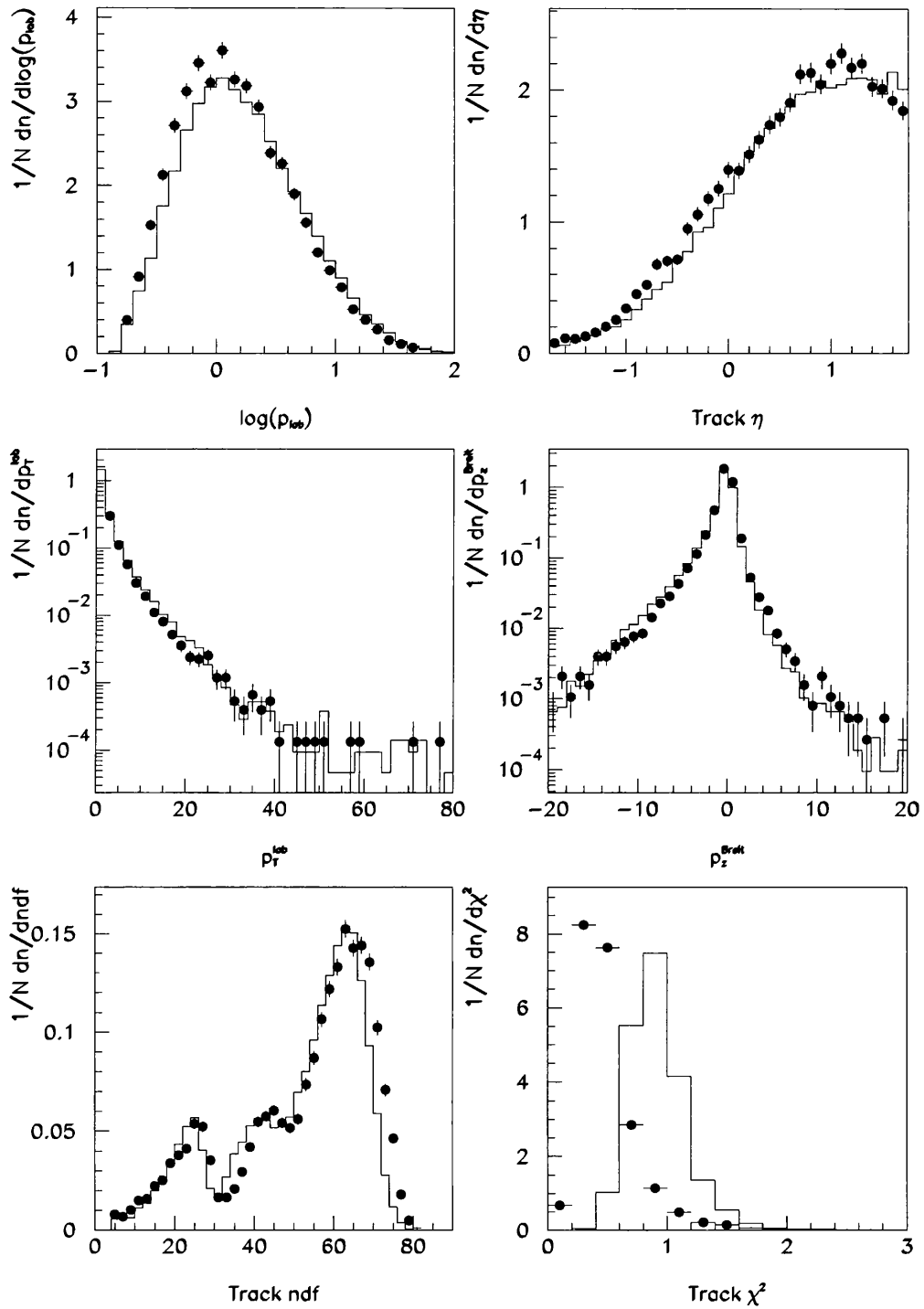
Figure 5.6: Comparison of 97 MC and data track variables.

Chapter 6

Reconstruction of Fragmentation Variables

In this chapter the transformation from the HERA laboratory frame to the Breit frame is described and an account is given of the method by which the boost employed in the transformation is calculated. The results of an investigation into the limits on the accuracy of the measurement of x_p and $\ln\left(\frac{1}{x_p}\right)$ are presented and the limiting factors are discussed. The investigation was restricted to the selected (x, Q^2) analysis bins and to the kinematic region defined by the event selection cuts (described in chapter 4).

6.1 Experimental Reconstruction of the Breit frame

The definition of the Breit frame is given in chapter 1 as the frame in which the exchanged boson in an interaction is completely spacelike. This definition leads to an expression for the velocity, $\underline{\beta}$, of the Breit frame with respect to the laboratory frame as

$$\underline{\beta} = \frac{\underline{q} + 2x\underline{P}}{q_0 + 2xP_0},$$

if $q = (q_0, \underline{q})$ and $P = (P_0, \underline{P})$ are the four-momenta of the virtual photon and the incident proton beam as measured in the laboratory frame, respectively. The mass of the proton is assumed to be negligible.

Particles taking part in a DIS event in the HERA laboratory frame (S) can be

85

transformed to the Breit frame (S') by performing a Lorentz transformation and subsequent rotations such that

- The virtual photon is aligned with the negative z'-axis; and

- the plane formed by the momenta of the incident and scattered positron is aligned with the x'-z' plane.

Since the four-momentum of the incident proton beam, $P = (820, 0, 0, 820)$ GeV, is well-defined[1], the experimental determination of the boost vector relies on the reconstruction of the kinematic variable x and of the four-momentum components of the exchanged virtual photon, $q = (q_0, \underline{q})$. The Double Angle method, as described in chapter 4, was used to determine these kinematic quantities. The virtual photon was experimentally reconstructed from the difference between the four-momenta of the incident and scattered positron. The 4-momentum of the incident positron[2] was assumed to be $k = (27.5, 0, 0, -27.5)$ GeV. The angle of the scattered positron was calculated using the information returned from the positron-finder described in section 2.3.6 and the position of the reconstructed event vertex. The energy of the scattered positron was derived from the angles θ_e and γ_h via the expression for Q^2_{DA}, using

$$E'_e = \frac{Q^2_{DA}}{2E_e(1 + \cos\theta_e)}$$

where E_e is the energy of the incident positron. This method avoids systematic difficulties which might arise from uncertainty in the energy scale of the calorimeter.

Having established the boost vector for the event, the final state particles were transformed to the Breit frame. The momenta of particles detected in the CTD were measured from the curvature of their tracks. Their energies were thence calculated assuming that they possessed pion mass. Particles with energy E and three-momentum $\underline{p}$ in the laboratory frame which passed the track selection cuts were transformed into the Breit frame where they had energy E' and three-momentum $\underline{p}'$ given by

$$E' = \gamma(E - \underline{\beta} \cdot \underline{p}) \qquad \text{and} \qquad \underline{p}' = \gamma(\underline{p} - \underline{\beta}E),$$

---

[1]The proton beam energy was measured to be $\sim$ 820.8 GeV in 1995, increasing to 820.9 GeV in 1997. The variation in energy was of the order of 100 MeV between 1995-7, and about 20 MeV within any particular year.

[2]In 1997 the nominal positron energy varied by about 40 MeV around a central value of 27.56 GeV.
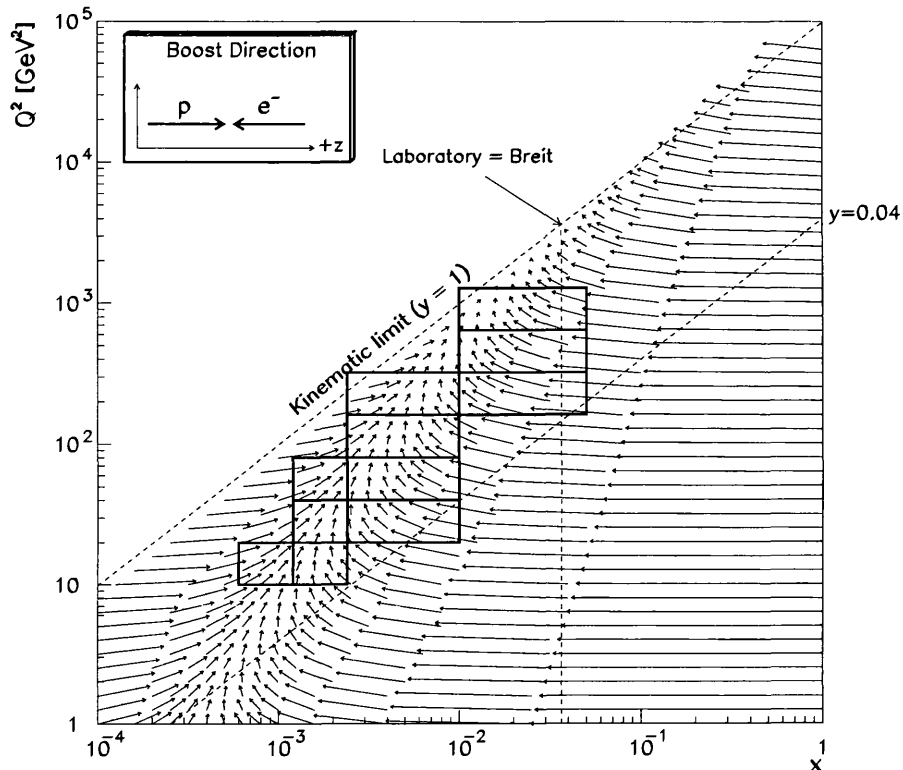
Figure 6.1: The variation in the magnitude and direction of the boost vector for the transformation from the laboratory frame to the Breit frame across the kinematic plane.

where $\gamma = 1/\sqrt{1 - \beta^2}$. Once the entire event had been transformed to the Breit frame, the particles were assigned to either the current or the target region, depending on their z'-momentum within the frame.

6.2   Properties of the boost

The arrows in figure 6.1 indicate the variation in the magnitude and direction of the boost vector required to transform from the laboratory frame to the Breit frame as a function of x and Q^2. The magnitude of the vectors is proportional to $\log \gamma$. A subset of the (x, Q^2) bins used in this analysis are outlined by the bold lines.

At high x a large negative longitudinal boost is needed to overcome the difference between the momentum of the parton and the much lower momentum positron, whilst

at low x the momentum of the parton is small in comparison with the incident positron and a substantial positive boost is required. In the analysis region – between these extremes – the boosts are relatively small with a large transverse component. Also indicated in the figure is the unique point at $x = E_e/E_P$ and $y = 1$ where the laboratory frame and the Breit frame coincide.

6.3 Migrations

The boost to the Breit frame is derived from the kinematic variable x and the four-momentum components of the virtual photon, which are experimentally determined using the reconstructed kinematic variables and the momentum components of the scattered positron. Thus poor reconstruction of x or a mismeasurement of the scattered positron would lead to a badly reconstructed Breit frame in which, for instance, the axes might be rotated or displaced relative to their true orientation. In this case not only would there be a degradation in the measurement of the individual particle momenta, but particles which truly lay in the current region could instead be reconstructed in the target region, or vice versa. This movement of particles due to reconstruction inaccuracies is known as migration. Patently, since this analysis relies on measuring particles in the current region of the Breit frame, it is necessary to investigate the extent and impact of particle migrations on the measured distributions. The Monte Carlo simulation described in chapter 5 was used to carry out such an investigation.

The Monte Carlo relates the generated particles to the hits measured in the CTD; using this information the reconstructed track with the most hits in common with a generated track was deemed to match that track. The generated tracks satisfying the event and track selection cuts were boosted to the Breit frame using the momentum components of the generated virtual photon. The matching reconstructed tracks were boosted to the Breit frame using the reconstructed virtual photon. Each true and measured track was then assigned to the current or target region according to its longitudinal momentum in the Breit frame, and those tracks for which the true track lay in one region and the matching observed track in the other were counted. The results are shown in table 6.1; the column labelled '%' indicates the percentage of the

number of particles observed in the current region the migrating particles represent.

x range	Q^2 range (GeV^2)	No. particles in current			No. particles in target		
		generated	migrate to target	%	generated	migrate to current	%
0.6 $-$ 1.2 10^{-3}	10 - 20	26353	3483	11	112505	10267	31
1.2 $-$ 2.4 10^{-3}	10 - 20	24045	2855	10	64750	6759	24
	20 - 40	20719	2438	10	56250	5237	22
	40 - 80	13639	1534	10	37234	2774	19
2.4 $-$ 10. 10^{-3}	20 - 40	24047	2986	12	37174	3707	15
	40 - 80	27857	2492	8	40327	4059	14
	80 - 160	65976	5712	8	107579	8033	12
	160 - 320	23836	1749	7	36246	2540	10
1.0 $-$ 5. 10^{-2}	160 - 320	35603	2924	9	17353	1481	4
	320 - 640	19419	1337	7	11556	972	5
	640 - 1280	9521	420	4	6376	525	6
0.025 - 0.15	1280 - 2560	15484	557	4	5264	491	3
0.05 - 0.25	2560 - 5120	5547	129	2	1144	118	2

Table 6.1: Table comparing the numbers of particles generated in the current and target regions of the Breit frame with the migrations between them due to the reconstruction procedure.

The entries for the $Q^2 \lesssim 80$ GeV^2 indicate the preponderance of particles found in the target region over those belonging to the current region. As Q^2 increases, the mean multiplicity of particles falling into the target region increases more slowly than that for particles in the current region [63], so that in the highest Q^2 bins most of the reconstructed tracks lie in the current region. Also, the topologies of the events alter as Q^2 increases, so that an ever-larger proportion of the phase space for the target region is discarded by the event and track selection cuts.

In the lower Q^2 bins the migrations from the target region into the current region (i.e. where the generated particle lay in the target region but was reconstructed in the current region) are significantly larger than those in the opposite direction. For $Q^2 \gtrsim 80$

GeV^2, the migrations in each direction appear to be approximately equal and represent $\leq 10\%$ of the particles found in the current region. The dwindling levels of migration with rising Q^2 shown in the table mirrors the improvement in the the resolutions in x and Q^2 shown in figures 4.4 and 4.5.

In order to ascertain whether these particles migrate democratically or whether any areas of measurement are particularly susceptible, the x_p and $\ln\left(\frac{1}{x_p}\right)$ spectra for correctly assigned particles were compared with those for migrating particles. Figure 6.2 shows the true scaled momentum spectrum for particles generated in the current region compared with the true scaled momentum spectrum of particles migrating from the current region to the target region for 1996 MC (i.e. $Q^2 > 70$ GeV^2) events generated in any of the analysis (x, Q^2) bins. The spectrum of migrating particles is roughly the same shape as the overall spectrum, at a level of $\lesssim 10\%$. In figure 6.3 the reconstructed scaled momentum spectra of the particles migrating *out of* the current region is compared with that for particles migrating *into* the current region. The two distributions are alike, suggesting that the migrations in each direction compensate for each other to a large extent.

Figures 6.4 and 6.5 show the $\ln\left(\frac{1}{x_p}\right)$ distributions from particles selected in the same ways. The spectrum of particles migrating out of the current region is roughly the same shape, although with a broader peak, as the overall distribution from particles generated in the current region. The $\ln\left(\frac{1}{x_p}\right)$ distribution from particles migrating into the current region is similar to that for particles migrating out of the current region.
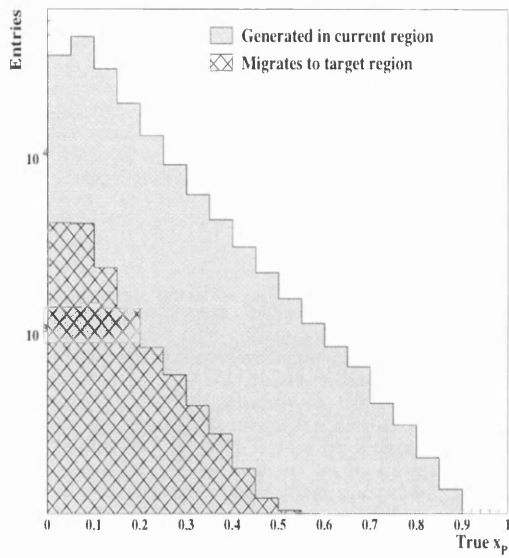
Figure 6.2: The x_p distribution for particles generated in the current region compared with the x_p distribution for those particles which migrate out.
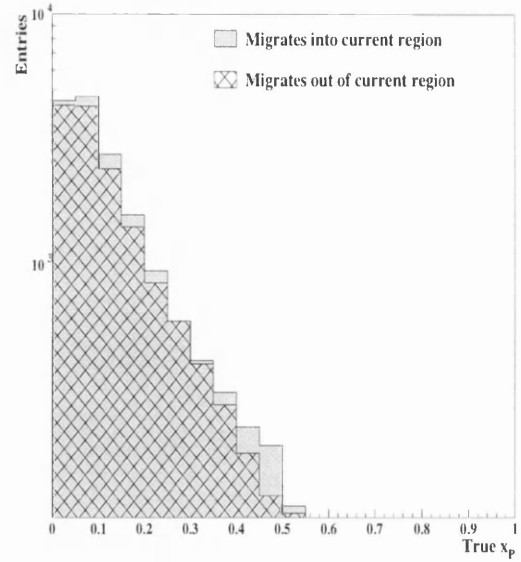
Figure 6.3: The x_p distribution from particles migrating out of the current region compared with that for those migrating in.
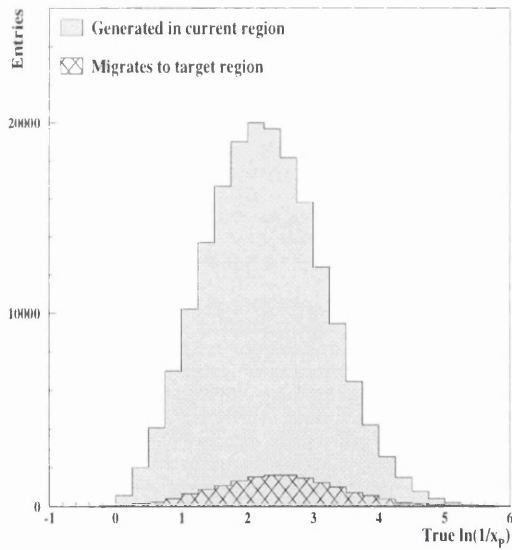
Figure 6.4: The $\ln\left(\frac{1}{x_p}\right)$ distribution from particles migrating out of the current region compared with that for those migrating in.
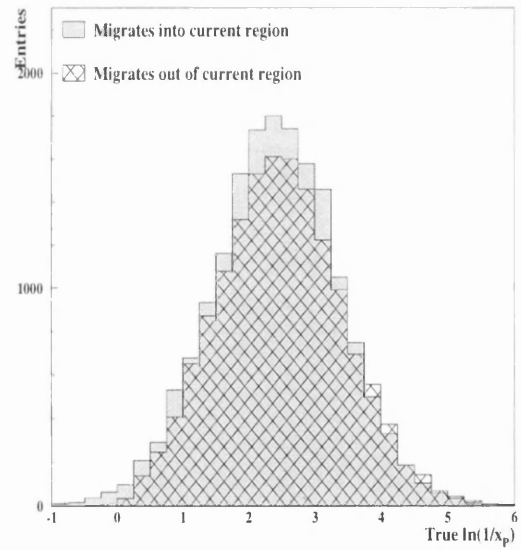
Figure 6.5: The $\ln\left(\frac{1}{x_p}\right)$ spectrum of particles migrating into the current region compared with the distribution for particles which migrate out.

6.4   Resolution of the Scaled Momentum

The quality of the reconstruction of x_p in the Breit frame was also studied by considering the resolution of the measured variable, that is by finding the difference between the value of x_p calculated when the true particles are operated on by the true boost (x_p^{True}) and that measured when the reconstructed tracks are boosted using the reconstructed boost (x_p^{Rec}) and remain in the current region. Fig 6.6 shows profile plots of the difference

$$\Delta = x_p^{\text{Rec}} - x_p^{\text{True}}$$

in the analysis (x,Q^2) bins. Points are plotted at the statistical mean of Δ in each x_p bin, and the error bars represent the RMS spread. In general the means occur at, or very close to, zero; the spreads improve towards medium Q^2 and then deteriorate again at the highest Q^2. The bin sizes in x_p chosen for the analysis are indicated by the dashed lines: that the spreads of the resolutions lie comfortably within these lines was accepted as justification for the chosen bin sizes.

The effects contributing to the resolution from the reconstruction can be split into two main contributing factors: the track reconstruction and the reconstruction of the boost. In figure 6.7 the contribution from the track reconstruction only is investigated. This figure shows profile plots of

$$\Delta_{\text{Track}} = x_p^{\text{Track}} - x_p^{\text{True}}$$

where x_p^{Track} is measured by boosting the reconstructed particle momenta using the true components of the virtual photon. x_p^{True} is as defined previously. Similarly, figure 6.8 shows the effect due to the reconstruction of the boost; here Δ_{Boost} is plotted, i.e.

$$\Delta_{\text{Boost}} = x_p^{\text{Boost}} - x_p^{\text{True}}$$

where x_p^{Boost} is the scaled momentum found by operating with the reconstructed components of the boost on the true particle momenta. Comparison of figures 6.7 and 6.8 reveals that reconstruction of the boost is the dominant factor in the resolution at low x and Q^2. At higher Q^2 the scattered positron is identified better and its energy is derived more accurately. However, high Q^2 events are boosted further forward in

the detector and their tracks are correspondingly more difficult to reconstruct. Thus the track reconstruction becomes the limiting factor on the measurement of x_p in the higher Q^2 bins.

Figure 6.9 shows profile plots of the resolution in the measurement of $\ln\left(\frac{1}{x_p}\right)$, where the dashed lines indicate the chosen binwidth of 0.25. At low Q^2 there is a systematic trend for large $\ln\left(\frac{1}{x_p}\right)$ values to be reconstructed with lower $\ln\left(\frac{1}{x_p}\right)$. This region corresponds to very low momentum tracks, and comparison with figure 7.16 shows them to fall well into the falling edge of the spectrum. This apart, the means are generally close to zero and the spreads of the resolutions justify the chosen binwidth.

6.4.1 Purities and Efficiencies

Following the investigation of the purity and efficiency of the x and Q^2 reconstruction in chapter 4, an assessment was made of the measurement of x_p and $\ln\left(\frac{1}{x_p}\right)$ in a similar fashion, where purity and efficiency were now defined for bin i of (x,Q^2,x_p) or of $(x,Q^2,\ln\left(\frac{1}{x_p}\right))$ as

$$P_i = \frac{\text{No. of tracks generated and reconstructed in bin } i}{\text{No. of tracks reconstructed in bin } i} \text{ ; and}$$

$$\epsilon_i = \frac{\text{No. of tracks generated and reconstructed in bin } i}{\text{No. of tracks generated in bin } i}$$

The purity and efficiency on x_p are laid out in the analysis (x,Q^2) bins in figures 6.10 and 6.11. They are low at low Q^2, rising to more than 50% at higher Q^2, and are approximately flat across the range of x_p. The efficiencies are higher than the purities throughout. There is a marked sharp fall-off in purity with x_p in bins 12 and 13, reflecting the deterioration in the resolution also visible in these bins.

The purities and efficiencies in $\ln\left(\frac{1}{x_p}\right)$ are shown in figures 6.12 and 6.13. Again, the efficiency is consistently lower than the purity, and both are low at low Q^2 and increase towards higher Q^2. The distributions are approximately flat across the values where the peaks of the distributions fall, but worsen towards larger values of $\ln\left(\frac{1}{x_p}\right)$.

6.5   Summary

The reconstruction of the fragmentation variables in the Breit frame of reference has been described. The resolution in the measurement of x_p and $\ln\left(\frac{1}{x_p}\right)$ is governed by the reconstruction of the boost in the low (x, Q^2) bins, and by the track reconstruction in the high (x, Q^2) bins. The chosen binwidths are commensurate with the resolutions in x_p and $\ln\left(\frac{1}{x_p}\right)$.
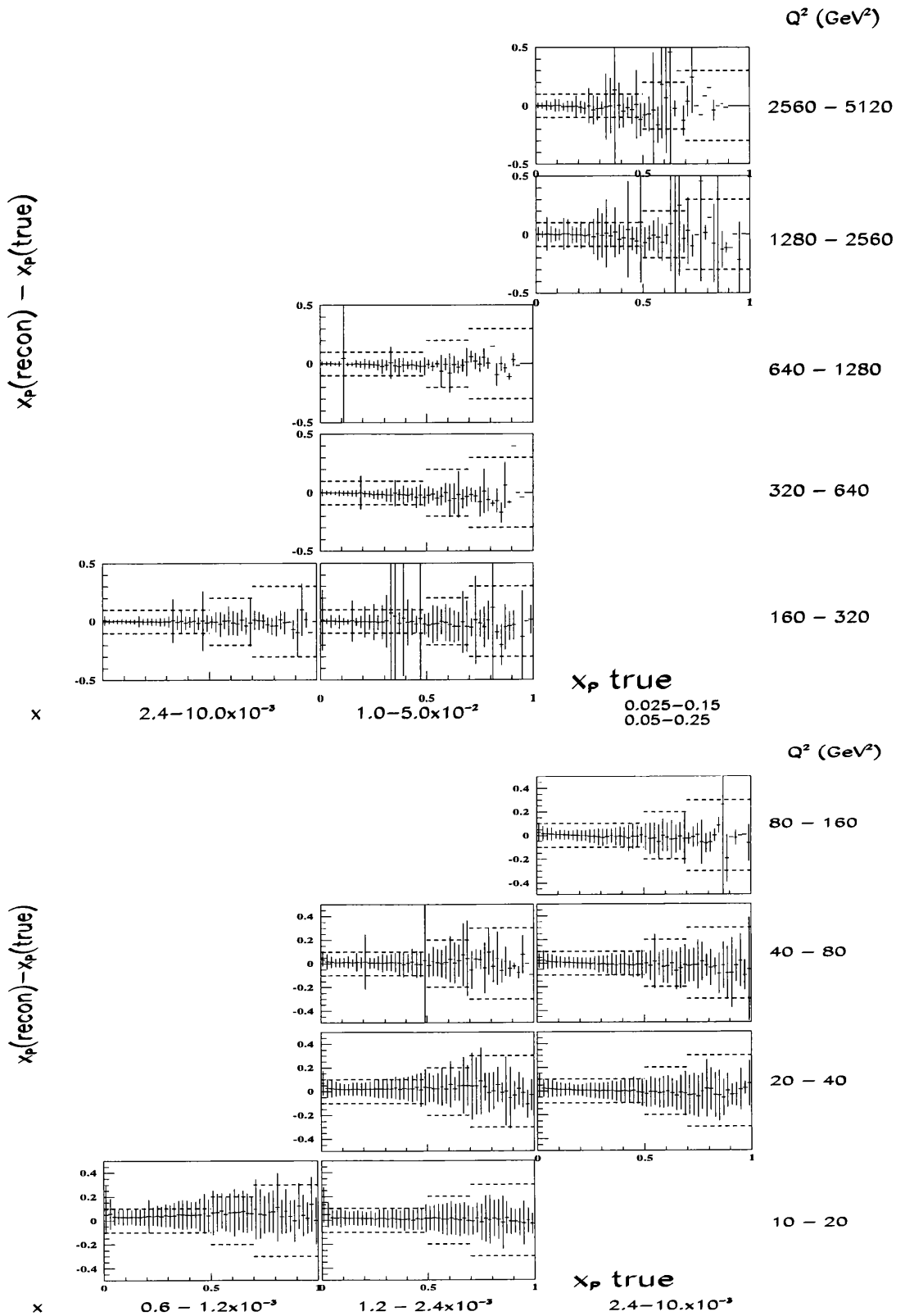
Figure 6.6: The resolution in the measurement of x_p.
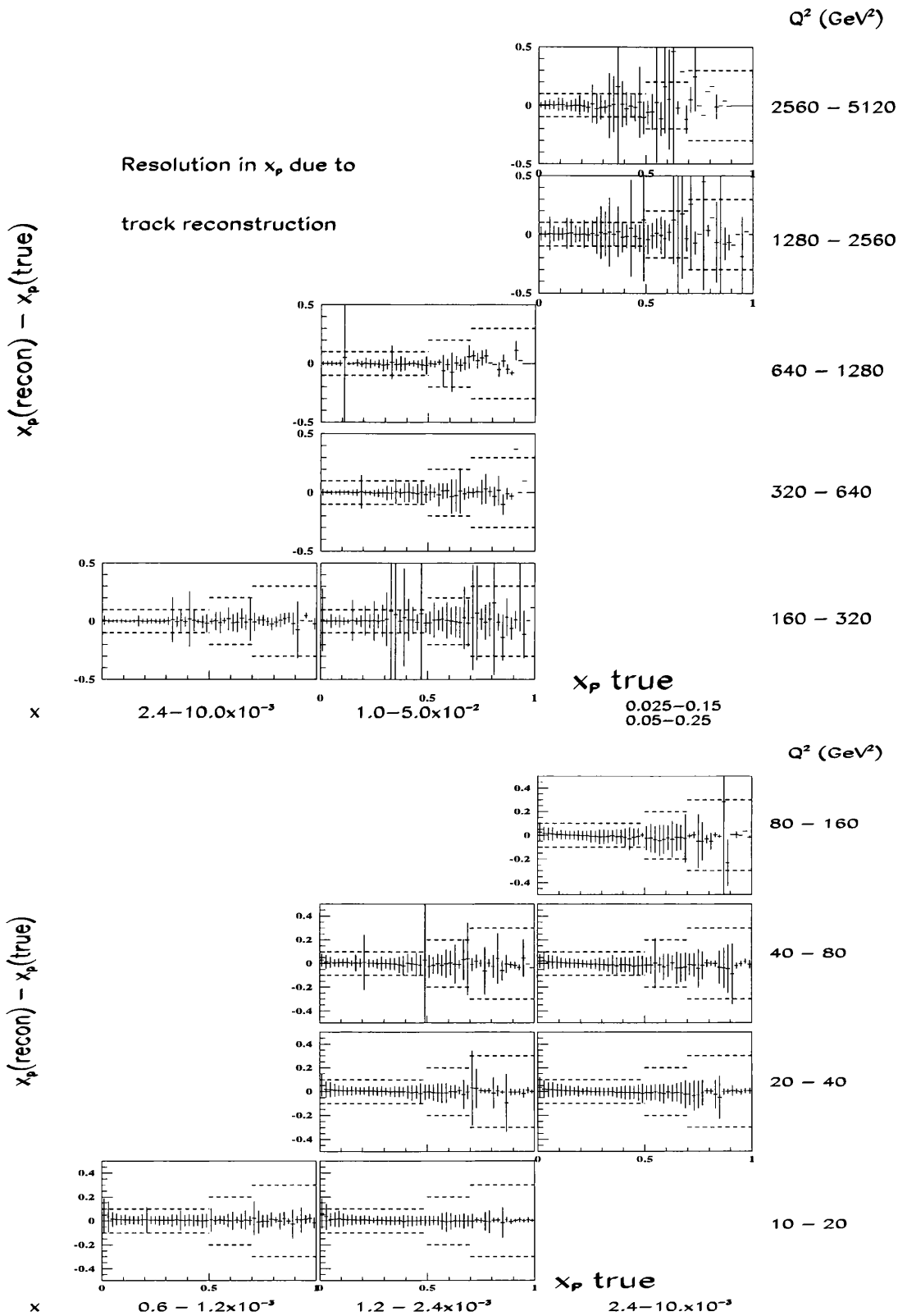
Figure 6.7: The resolution in the measurement of x_p due to the track reconstruction.

Figure 6.8: The resolution in the measurement of x_p due to the reconstruction of the boost.
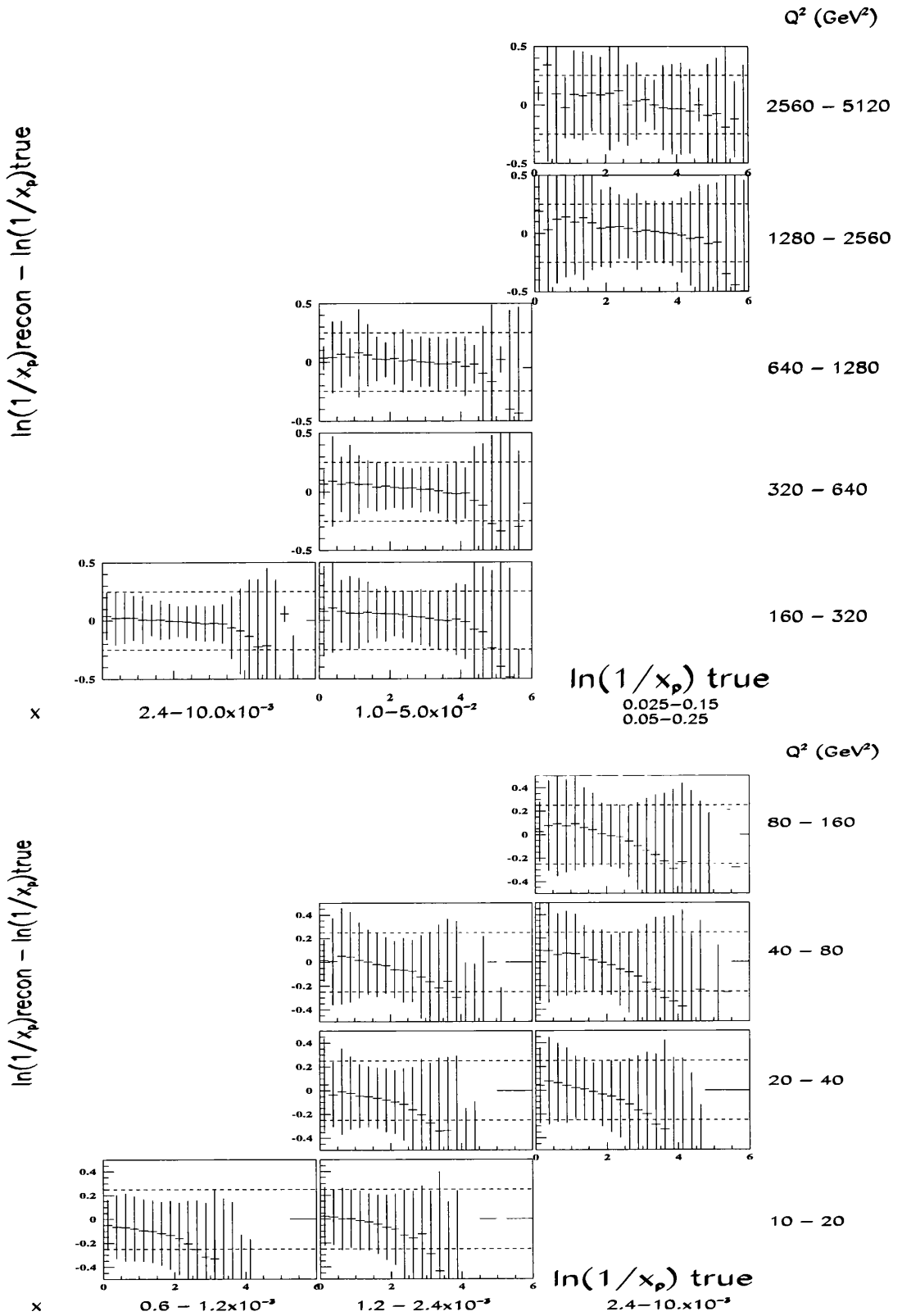
Figure 6.9: The resolution in the measurement of $\ln\left(\frac{1}{x_p}\right)$.
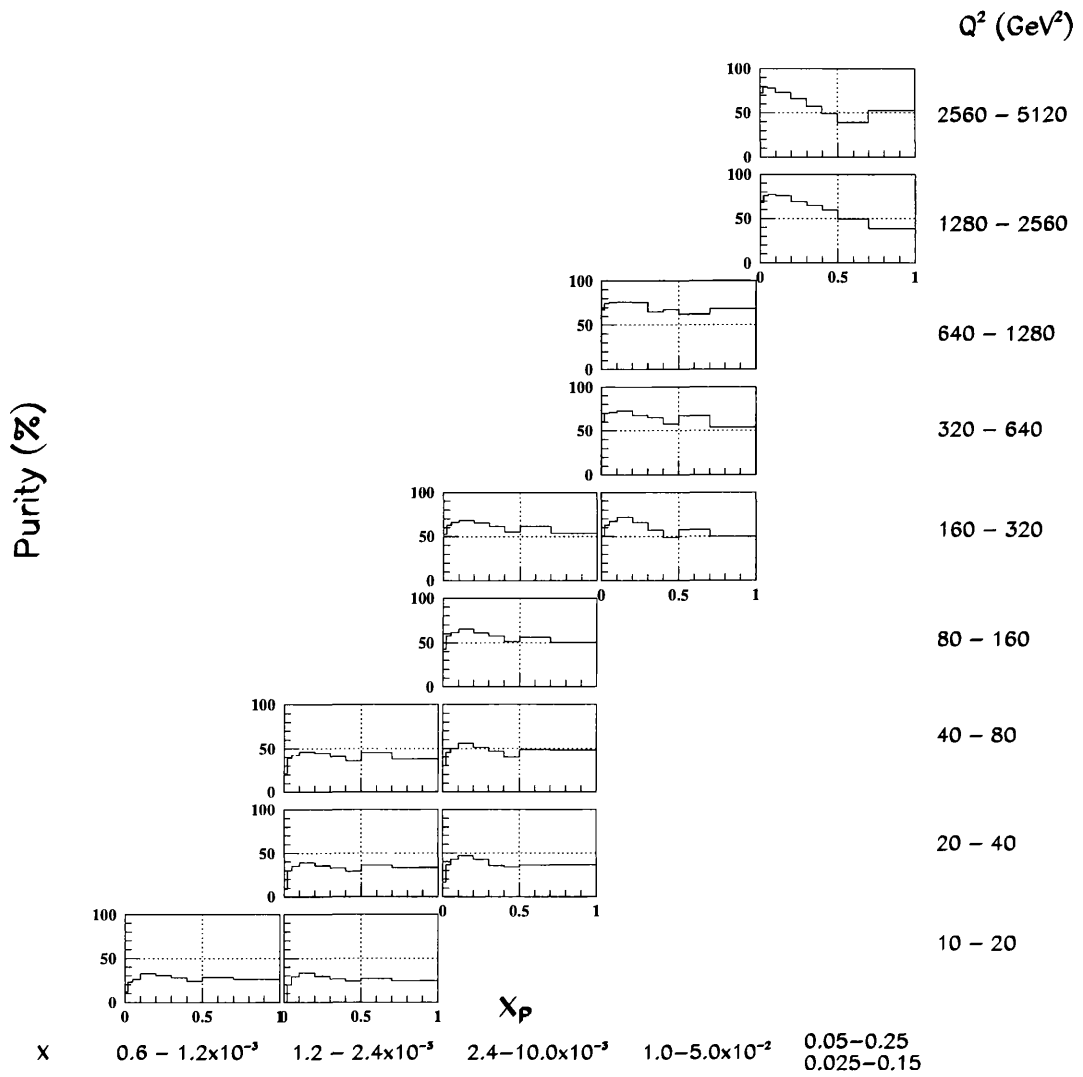
Figure 6.10: The purity in the measurement of x_p in the analysis (x, Q^2) bins.
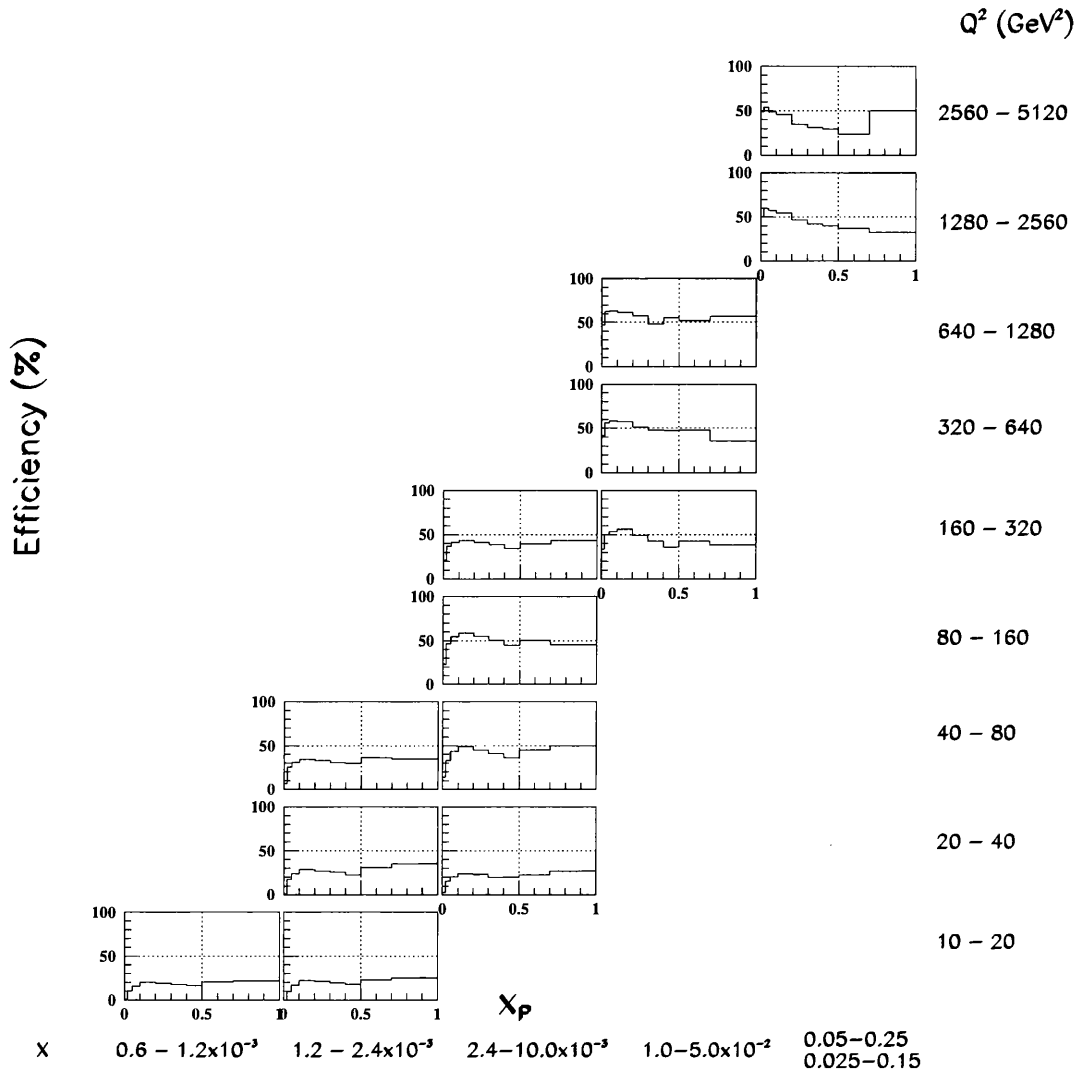
Figure 6.11: The efficiency in the measurement of x_p in the analysis (x, Q^2) bins.
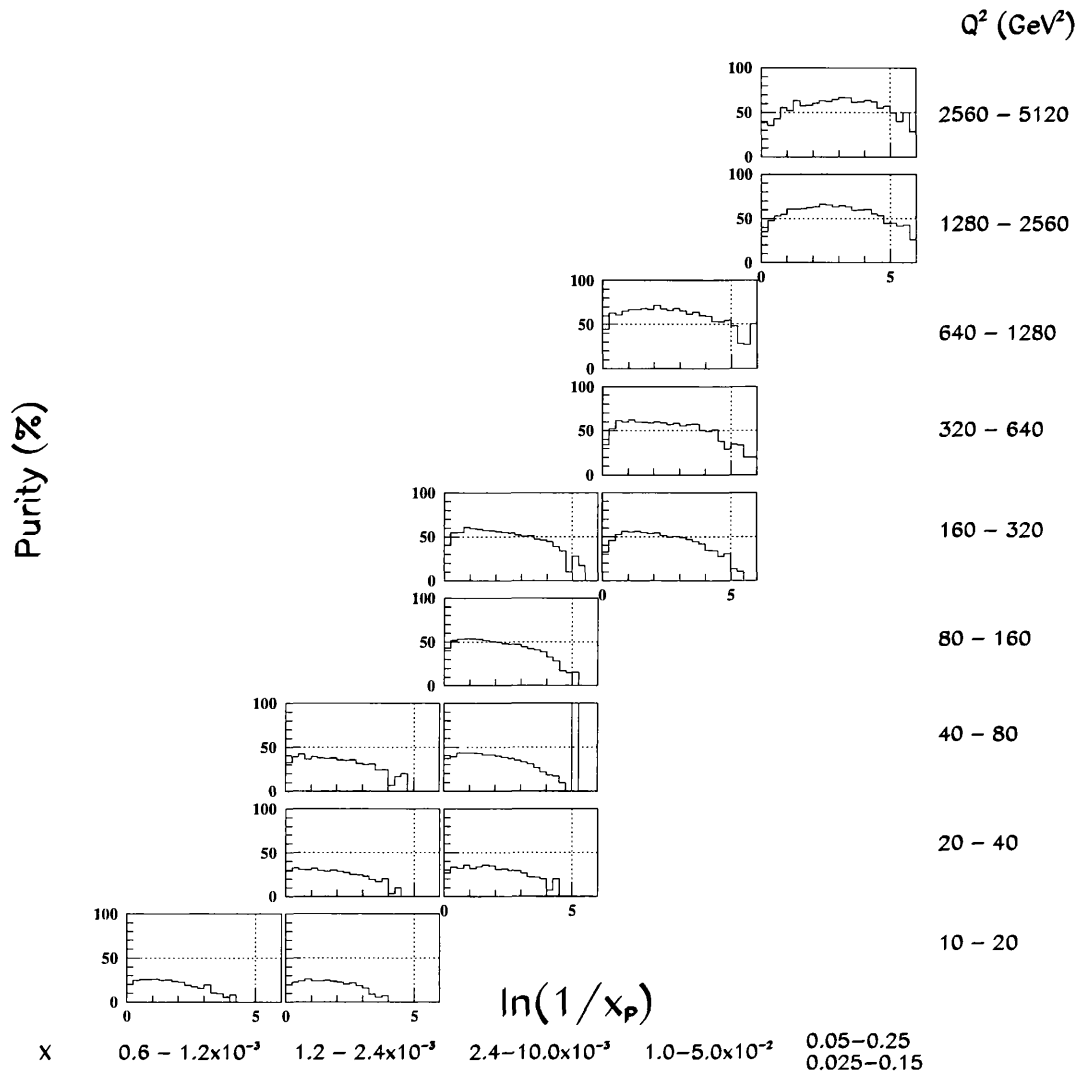
Figure 6.12: The purity in the measurement of $\ln\left(\frac{1}{x_p}\right)$ in the analysis (x, Q^2) bins.
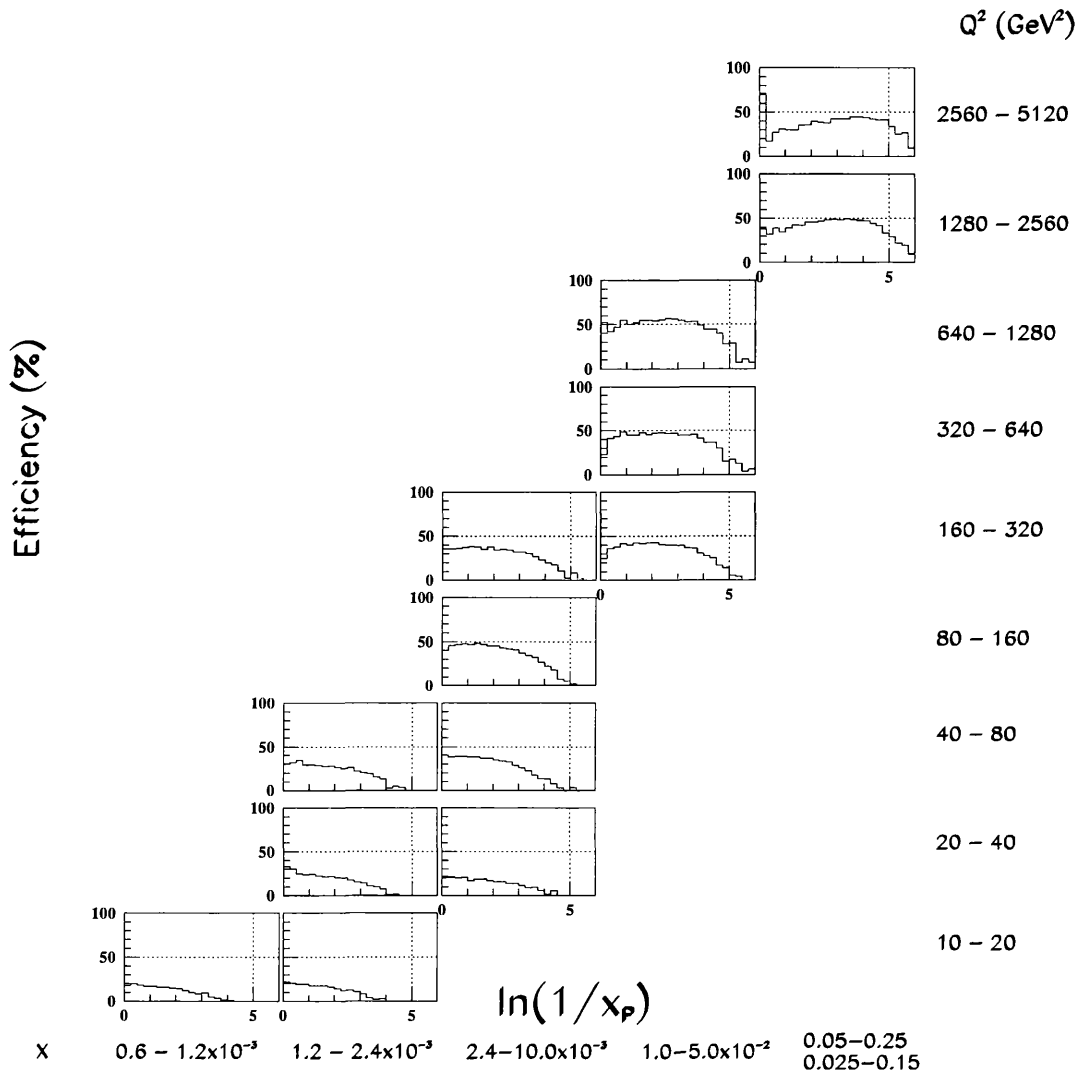
Figure 6.13: The efficiency in the measurement of $\ln\left(\frac{1}{x_p}\right)$ in the analysis (x,Q^2) bins.

Chapter 7

Correction of Fragmentation Variables

In this chapter the raw x_p and $\ln\left(\frac{1}{x_p}\right)$ distributions are presented. The process by which the measured data is corrected for the detector response is illustrated using 1996 ZEUS data and Monte Carlo. The methods used to correct and combine results from different years' data-taking are discussed, and the corrected data distributions obtained from this procedure are shown. The systematic effects arising from varying the analysis method are described.

7.1 The Raw Data

Events were selected to satisfy the cuts described in chapter 4; the kinematic variables of the surviving events were derived via the Double Angle method and events were binned in intervals of x and Q^2 commensurate with the resolution given by this reconstruction method. The boost to the Breit Frame was calculated as related in chapter 6, using the four-momentum components of the scattered positron and the kinematic variables x_{DA} and Q^2_{DA}. Tracks in the CTD which were associated with the primary vertex and fulfilled the track selection requirements $p_T > 150$ MeV and $|\eta| < 1.5$ were reconstructed - assuming pion mass to determine the particle's energy - and boosted to the Breit frame. Tracks with $p_z^{\mathrm{Breit}} < 0$ were assigned to the current region, and the quantities
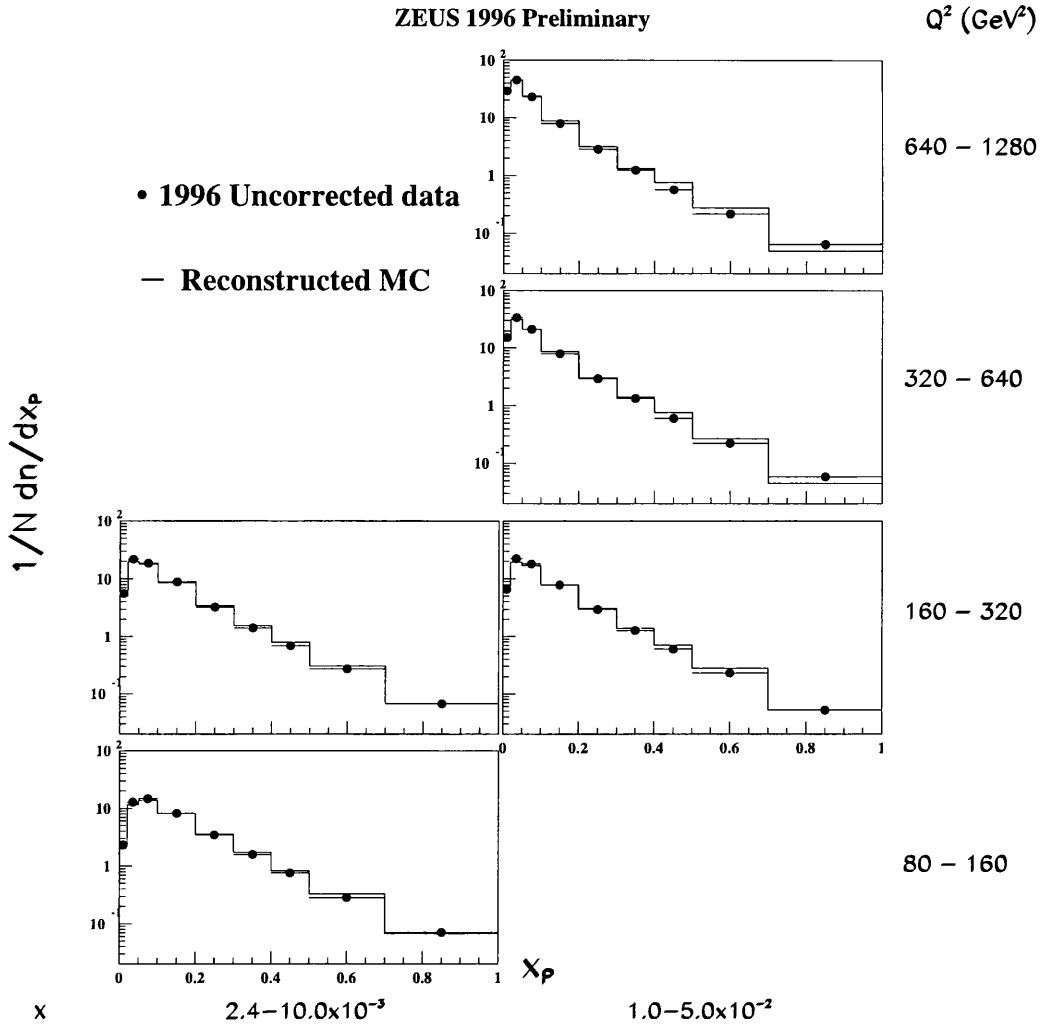
Figure 7.1: Raw data x_p distributions measured from data taken in 1996.

x_p and $\ln\left(\frac{1}{x_p}\right)$ were measured.

Investigation of the resolution on the reconstruction of the measured variables (see chapter 6) demonstrated that the uncertainties in the measurements are dominated by the reconstruction of the boost vector, $\underline{\beta}$, at low Q^2 and by the accuracy of track reconstruction at high Q^2.

Figure 7.1 shows the resulting raw scaled momentum, $x_p = 2p/Q$, spectra measured from tracks in ZEUS data taken during the 1996 running period. The bulk of the produced particles appear with $x_p < 0.1$, and the distribution falls rapidly towards
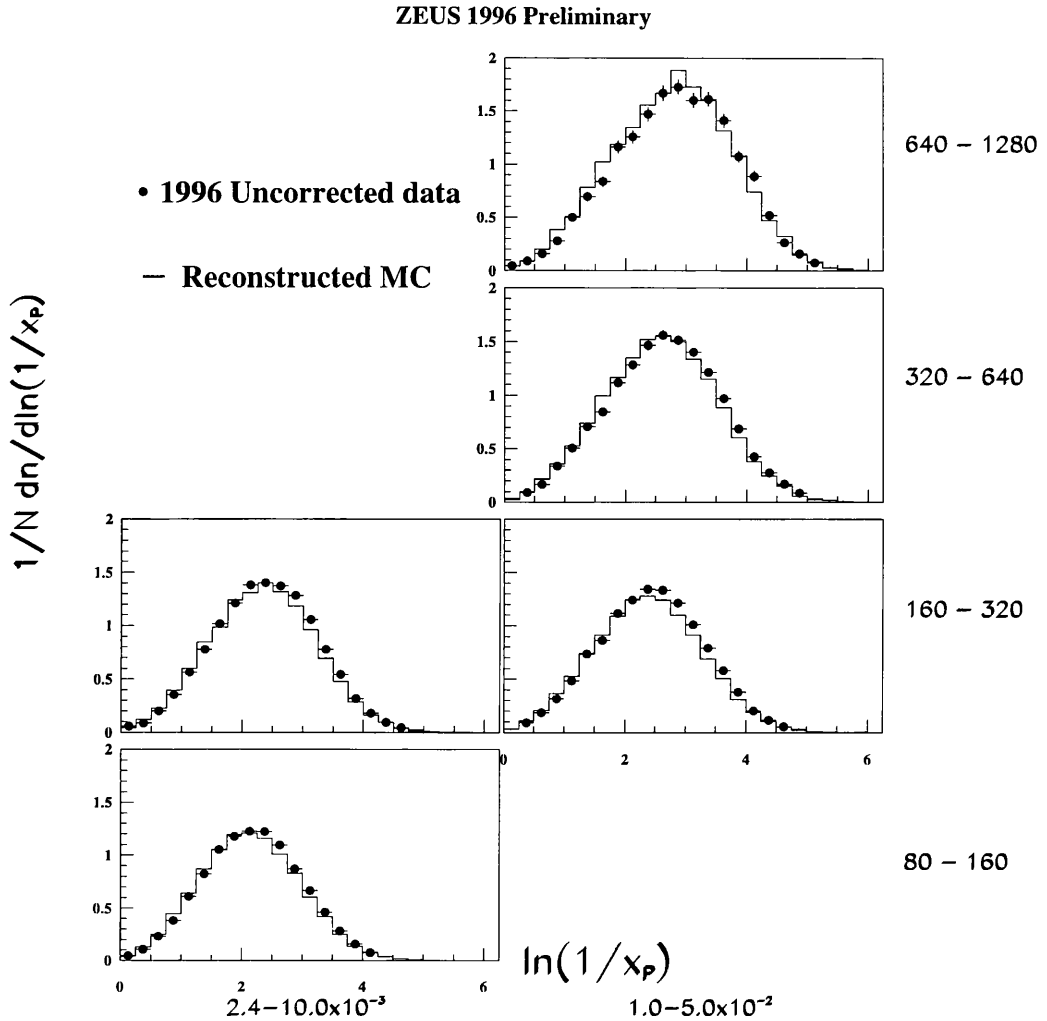
Figure 7.2: Raw $\ln\left(\frac{1}{x_p}\right)$ distributions measured from data taken in 1996.

larger values of x_p.

The raw $\ln(1/x_p)$ spectra measured using the same data sample are presented in figure 7.2. The distributions are roughly Gaussian, and show increasing multiplicity with increasing Q^2. There are slight differences between the distributions measured in the same Q^2 range but separate x ranges.

Both sets of distributions show broadly the expected characteristics at this stage, but conclusions cannot confidently be drawn until the distributions have been corrected.

7.2 Data Correction

As described in chapter 5, the distributions observed in the detector are a convolution of the true distributions with the distortions introduced by the acceptances and resolutions of the detectors used to measure them. These effects can be corrected using the procedure outlined below. The correction procedure is based on a combination of simulated physics events produced by event generators with a detailed Monte Carlo simulation of the ZEUS detector. The ARIADNE Monte Carlo was used for the standard corrections to the distributions, since it has been shown to give the best description of our observed energy flow [58, 59]. Figures 7.1 and 7.2 show, overlaid on the raw data points, the distributions obtained by passing the Monte Carlo events through the detector simulation and the same reconstruction, selection and analysis processes as the data. The Monte Carlo describes the data well, which lends confidence to its use in the correction procedure.

Correction factors were constructed from the Monte Carlo simulation by generating the "true" distributions from stable charged hadrons in the final state - obtained using solely the event generator information - and comparing them with the "observed" distributions from tracks found after the detector and trigger simulations had been carried out and the same reconstruction, selection and analysis had been performed as those applied to the real data. The decay products of K_S^0 and Λ particles, and the products from decays of weakly decaying particles with a lifetime $> 10^{-8}$ s were not included in the "true" distributions. Monte Carlo studies using 1994 tracking and detector have shown that up to 2% of the current region tracks from the reconstructed primary vertex are due to charged particles from the decay of K_S^0 and Λ [49].

Bin-by-bin correction factors were defined, for example, for each x_p bin in a (x,Q^2) bin as:

$$F(x_p) = \frac{1}{N_{\text{gen}}} \left(\frac{dn}{dx_p} \right)_{\text{gen}} \Bigg/ \frac{1}{N_{\text{obs}}} \left(\frac{dn}{dx_p} \right)_{\text{obs}}$$

where N_{gen} (N_{obs}) was the number of generated (observed) Monte Carlo events falling into the particular (x, Q^2) interval. Clearly the errors in the correction factors cannot simply be taken as the errors in the ratios of two statistically independent distributions, since the bin in which a particle is generated affects the bin in which it is reconstructed.

The method of calculating the statistical error on such a ratio is outlined in appendix B. The errors calculated thus tended to be about 10% larger than the straightforward binomial error in the low (x,Q^2) bins (bins 1 to 5) where migrations are large, about the same as the binomial errors in the medium Q^2 bins (7 to 10) and smaller by 10 to 25 % in the high Q^2 bins where migrations are very low.

Since the data and the correction factors are statistically independent distributions, their errors were combined in quadrature to give the statistical errors in the corrected distributions. The data are thus corrected for the effects of:

. the acceptance and resolution of the detector;

. the event reconstruction and selection;

. the track reconstruction and selection;

. the decay products of K^0_S and Λ decays being misassigned to the primary vertex;

. QED radiation;

. event migration between (x, Q^2) bins;

. track migration between current and target regions; and

. track migration between x_p or $\ln\left(\frac{1}{x_p}\right)$ bins.

For the bin-by-bin correction technique to be valid, the widths of the bins in x_p and $\ln\left(\frac{1}{x_p}\right)$ must be consistent with the resolutions in their measurements: this ensures that any bias introduced by the Monte Carlo employed in the correction procedure is minimised. As described in chapter 5, the ZEUS detector evolves with each year of running so that Monte Carlo generated using the detector description for one year cannot be used to correct data gathered in a different year. Therefore, correction factors were obtained from each year's Monte Carlo separately, and data from different years were only combined after the correction procedure had been performed. The following figures were obtained from 1996 ZEUS data and Monte Carlo (unless otherwise stated).

Figure 7.3 shows correction factors to the x_p distributions obtained from 1996 ARIADNE Monte Carlo. The correction factors are approximately flat and vary
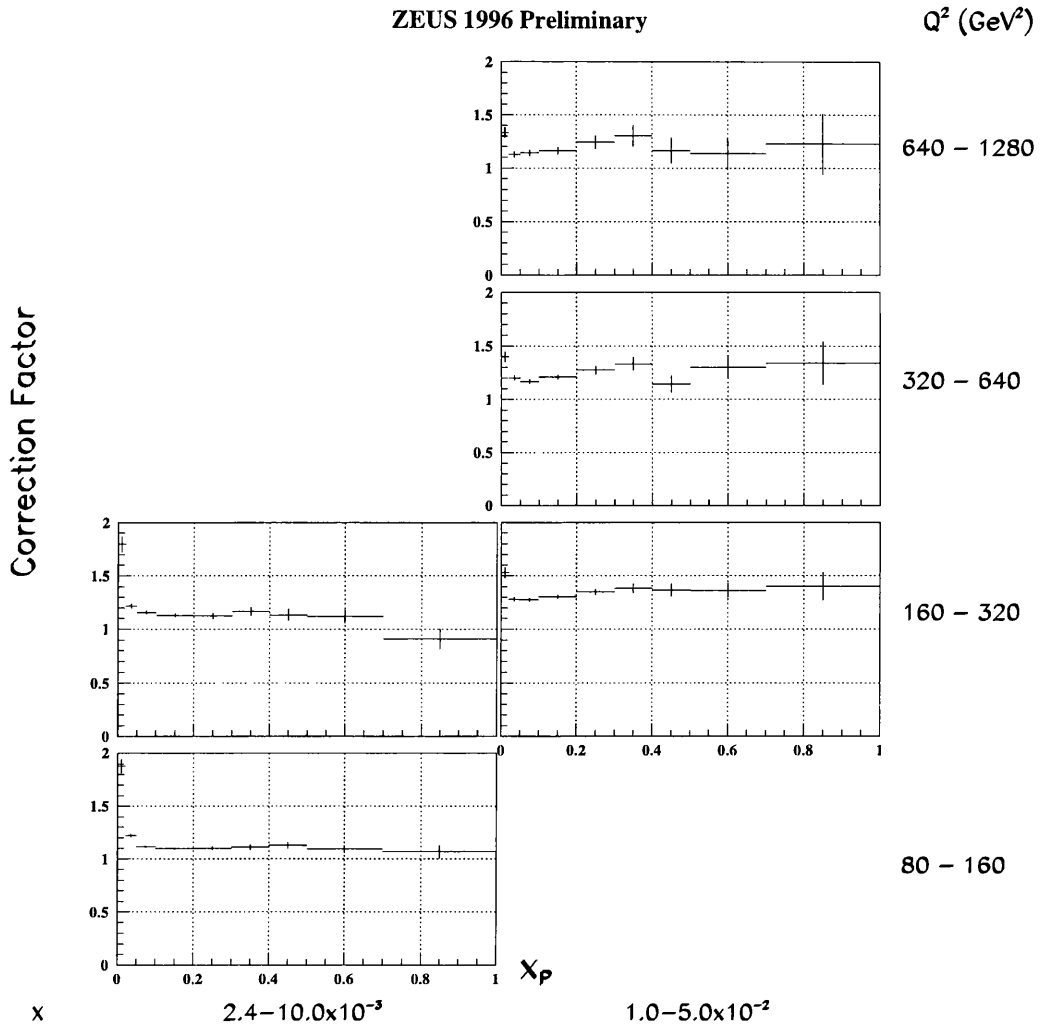
Figure 7.3: Correction factors to the x_p distributions derived from 1996 ARIADNE Monte Carlo.

between about 1.0 and 1.3, except at very low x_p ($x_p < 0.02$) where many low momentum tracks are discarded by the tracking cuts. Figure 7.4 shows the correction factors for the $\ln\left(\frac{1}{x_p}\right)$ distributions. In the region where the peak in the Gaussian occurs, the factors are flat and vary between about 1.0 and 1.5, although they rise sharply in the region of the high $\ln\left(\frac{1}{x_p}\right)$ tails where the acceptance falls due to the track $p_T > 150$ MeV cut. Since the analysis concentrates on the position of the maximum of the distributions - where the bulk of the particle production occurs - these correction factors are satisfactory for the correction of the data.
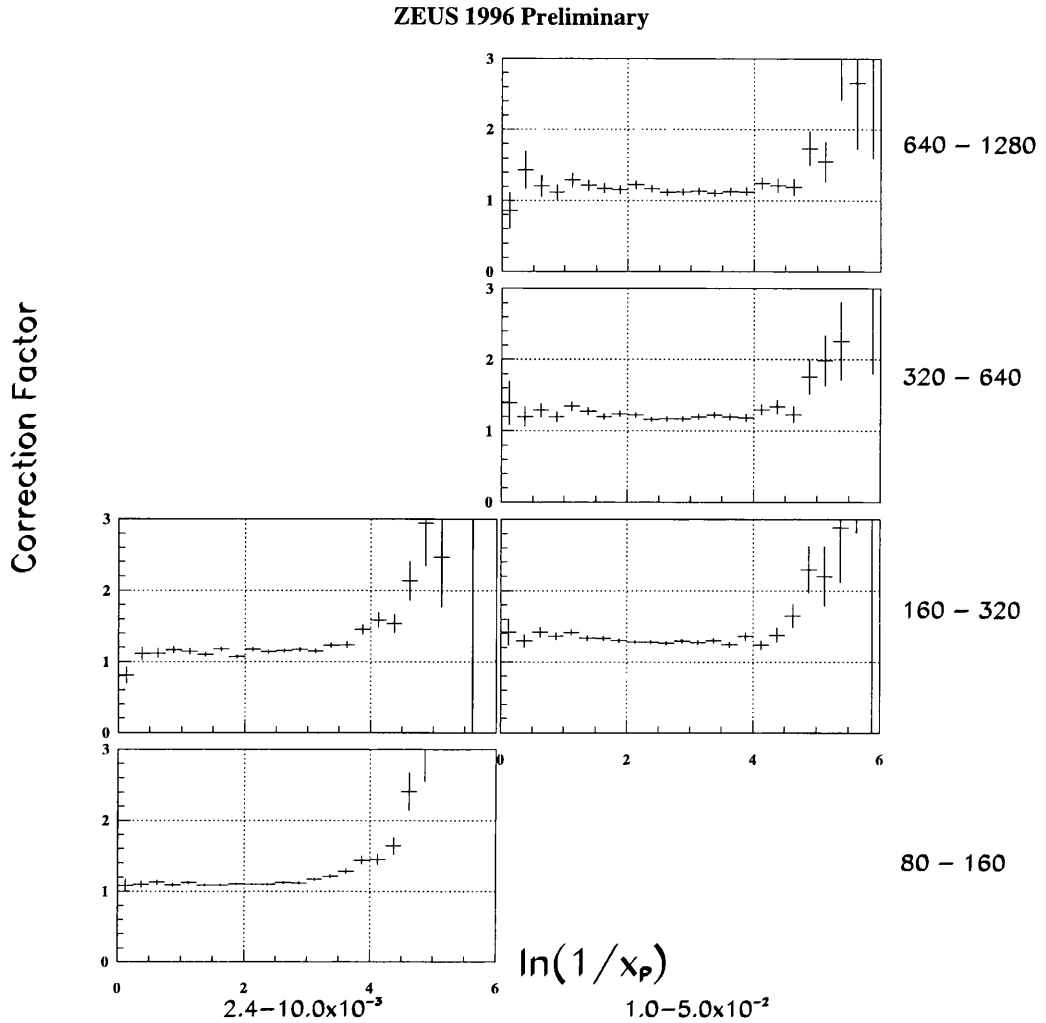
Figure 7.4: Correction factors to the $\ln\left(\frac{1}{x_p}\right)$ distributions derived from 1996 ARIADNE Monte Carlo.

The raw data distributions were multiplied by the correction factors to obtain corrected distributions.

7.3   Corrected Data Distributions

Figures 7.5 and 7.6 show the corrected x_p and $\ln\left(\frac{1}{x_p}\right)$ distributions with statistical errors only. The histograms are the distributions obtained from the generated Monte Carlo, and agree well with the corrected data distributions. The corrected data have
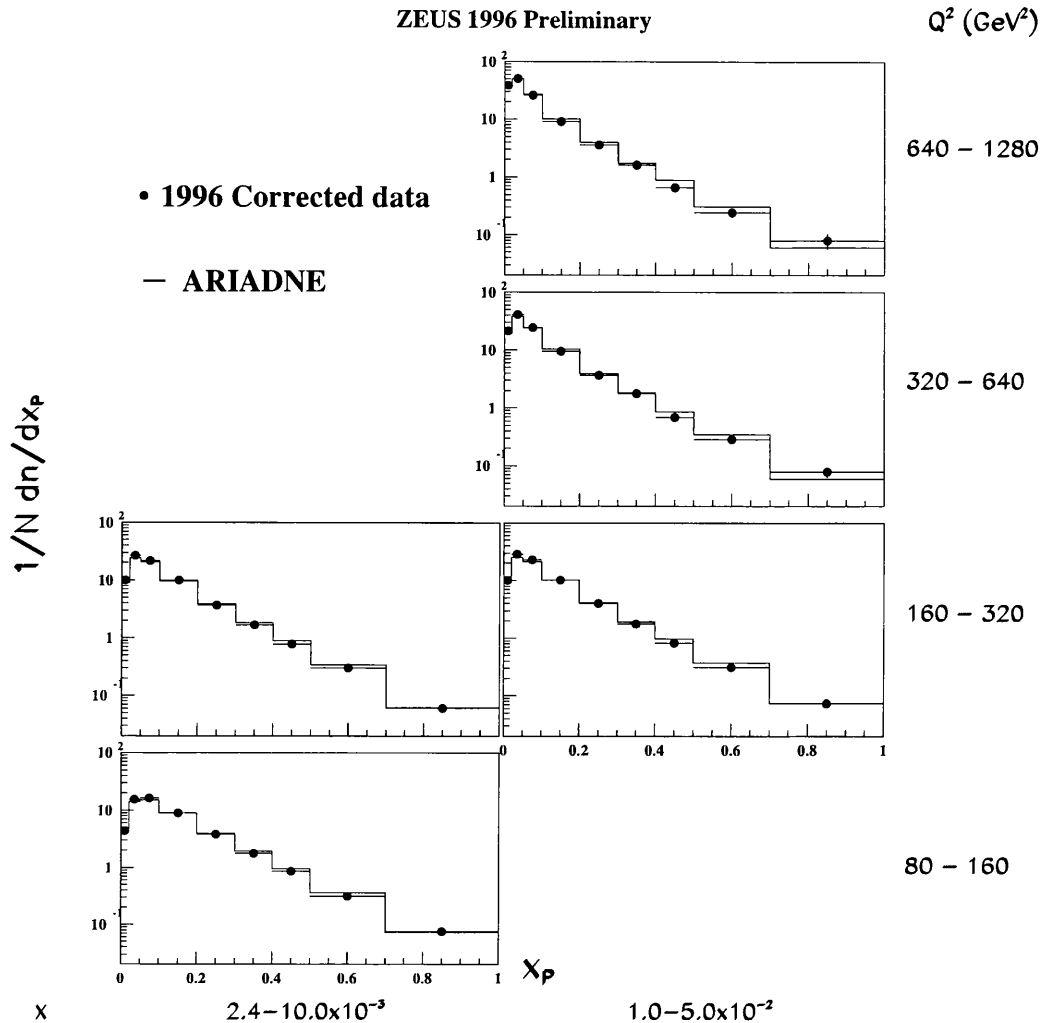
Figure 7.5: Corrected x_p distributions from 1996 ZEUS data.

higher means and multiplicities and do not exhibit the x dependence apparent in the raw data.

As Q^2 increases, the phase space for gluon radiation increases, and so the primary quarks in DIS interactions lose more energy to QCD effects. Hence it is expected that with increasing Q^2 the high x_p region of the scaled momentum spectrum will be depleted, while the radiated gluons will tend increasingly to populate the low x_p region.

The corrected data in figure 7.5 demonstrate the expected inflation in soft particle production with rising Q^2, and a distinct increase can be seen in the steepness of the
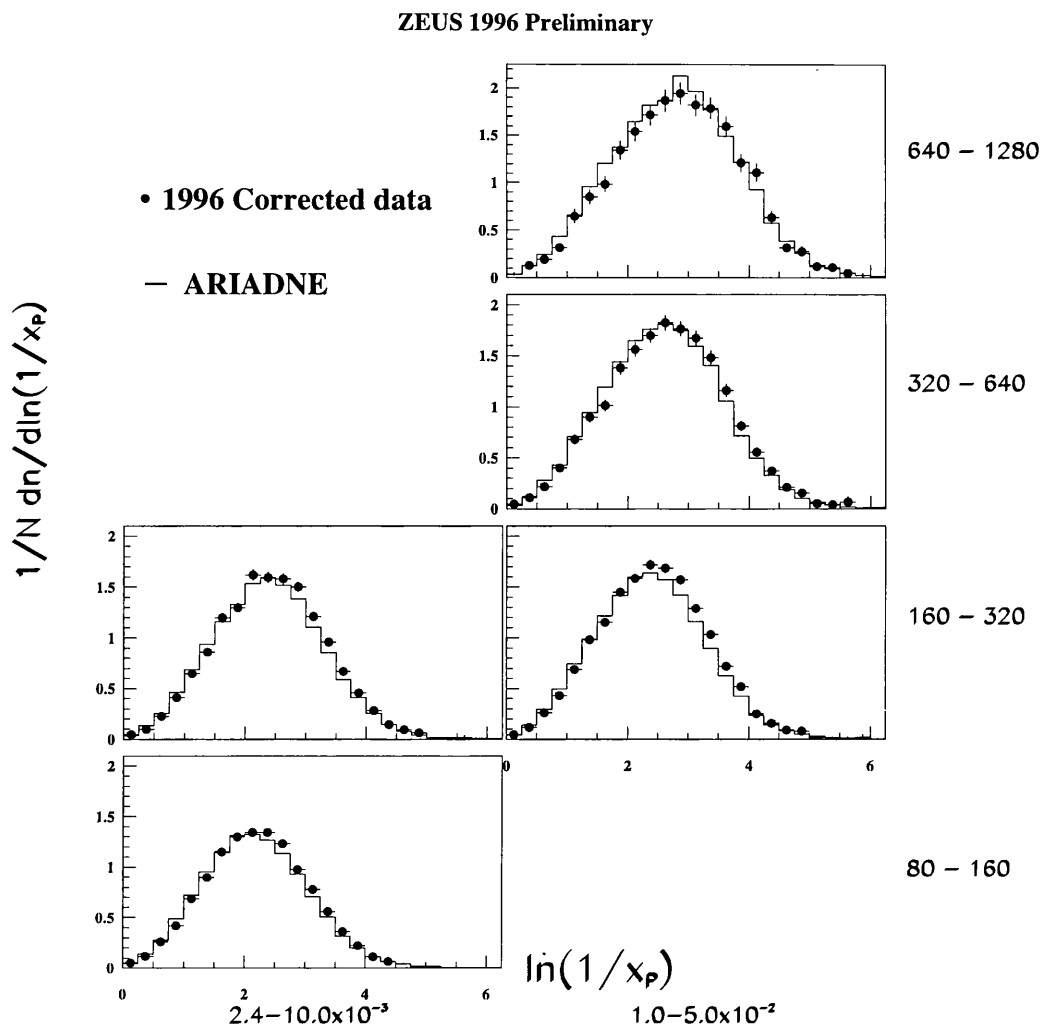
Figure 7.6: Corrected $\ln\left(\frac{1}{x_p}\right)$ distributions from 1996 ZEUS data.

x_p distributions with rising Q^2 in the same x range. The $\ln\left(\frac{1}{x_p}\right)$ distributions in figure 7.6 reveal the theoretically anticipated broad Gaussian shape, and the shift of the peak in the distributions with increasing Q^2 can be discerned clearly.

7.4   Combining the Data Samples

Having obtained corrected x_p and $\ln\left(\frac{1}{x_p}\right)$ distributions from each year's data, the distributions were checked for consistency from year to year by taking ratios of the
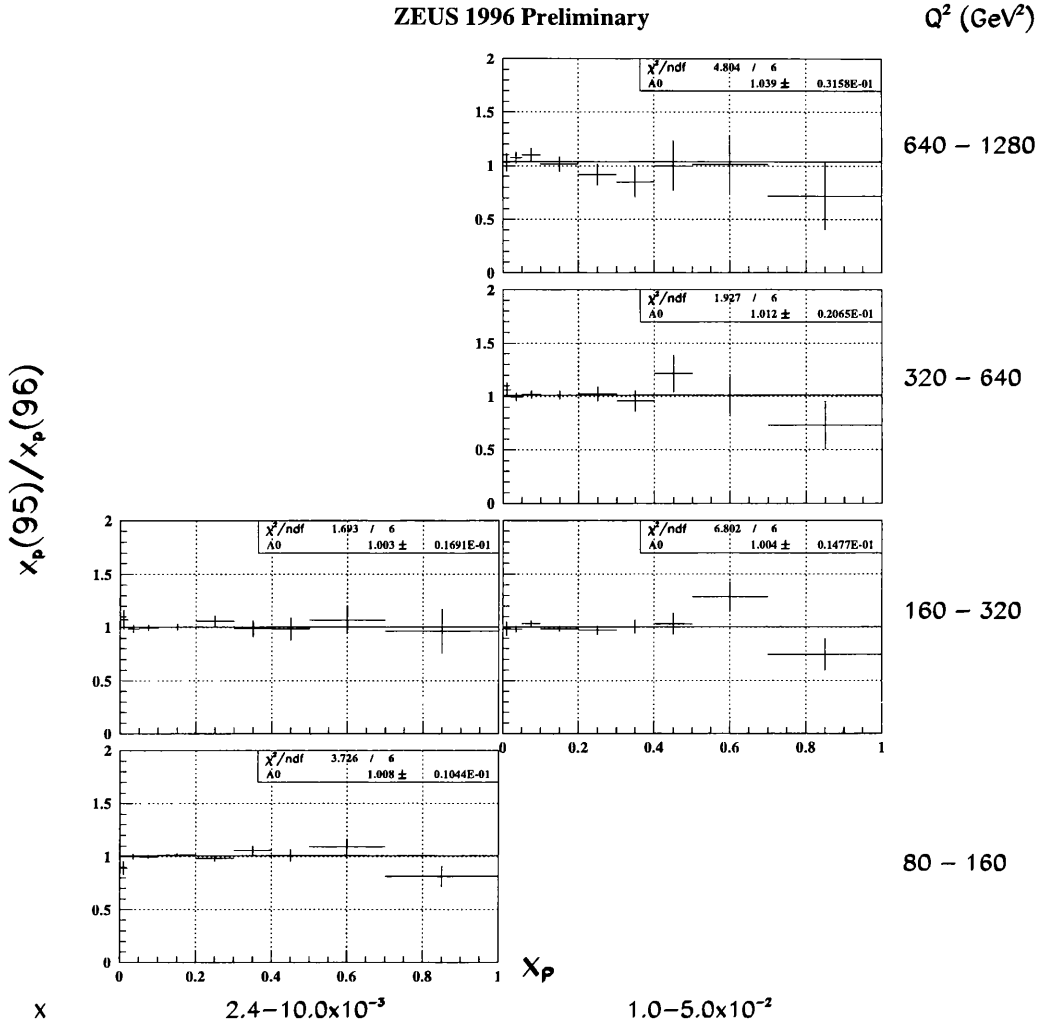
Figure 7.7: Ratios of the x_p distributions measured using 1995 ZEUS data and Monte Carlo to those measured using 1996 ZEUS data and Monte Carlo.

measurements from different years. One such set of plots is shown in figures 7.7 and 7.8. Figure 7.7 contains the ratios of the x_p distributions measured from 1995 ZEUS data to those measured from 1996 ZEUS data in each (x, Q^2) bin. The points between $0.02 < x_p < 0.7$, i.e. the x_p range wherein the measurement is considered to be reliable, were fitted with a straight line: A0 is the intercept obtained from that fit. In each case the ratio is consistent with unity and gives a sensible χ^2. Figure 7.8 contains the same information for the ratios of the $\ln\left(\frac{1}{x_p}\right)$ distributions measured in 1995 and 1996: the

ZEUS 1996 Preliminary
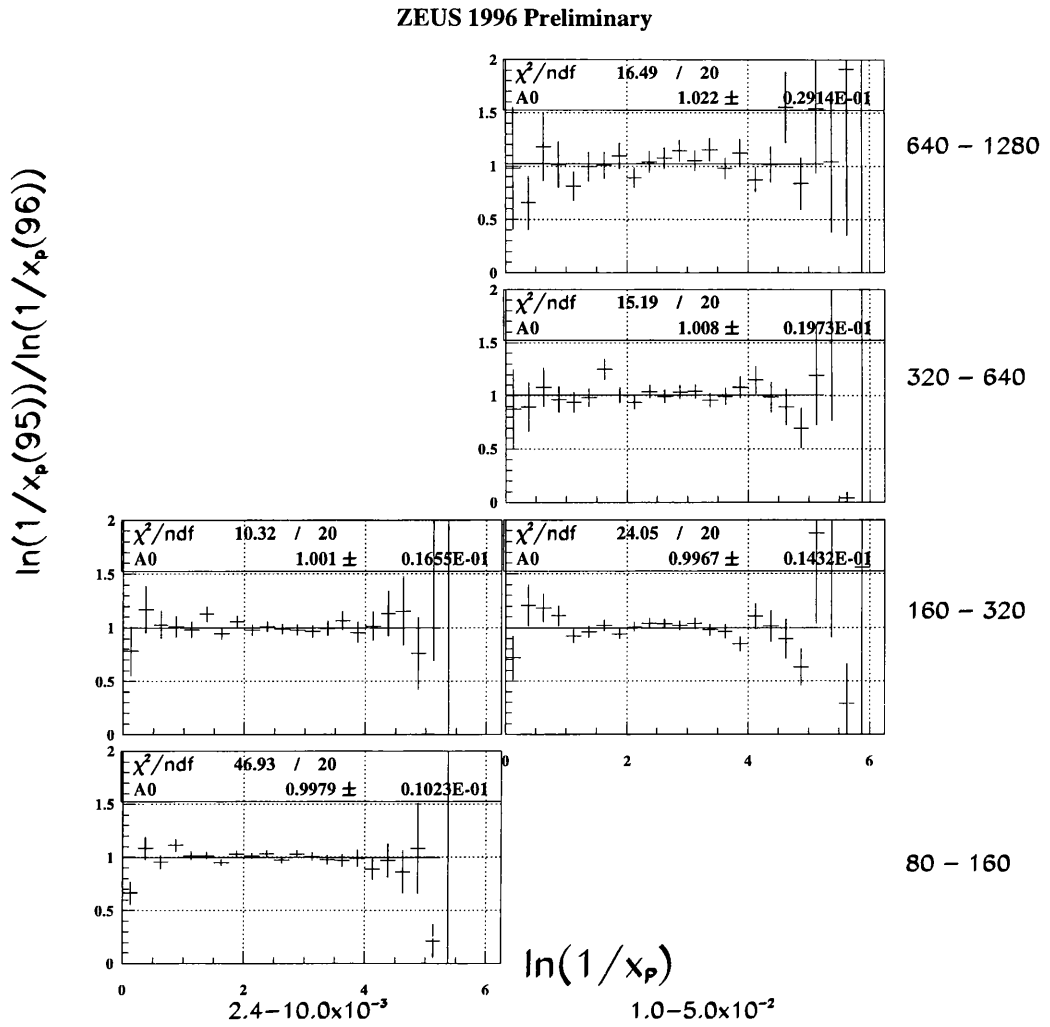
Figure 7.8: Ratios of the $\ln\left(\frac{1}{x_p}\right)$ distributions measured using 1995 ZEUS data and Monte Carlo to those measured using 1996 ZEUS data and Monte Carlo.

fit is performed between $0 < \ln\left(\frac{1}{x_p}\right) < 5.25$, approximately the range of values across which the peaks in the distributions is seen to vary. Again, the fits give ratios consistent with unity and sensible values of χ^2. The corrected annual distributions were combined statistically to obtain a result for the full data sample.

7.5 Systematic Checks

The results obtained using the central method of analysis cannot be taken at face value without checking their sensitivity to the selection cuts and reconstruction methods used. These systematic studies can be divided into three general classes: systematics due to the event reconstruction and selection, due to the track reconstruction and selection, and due to the Monte Carlo model used in the correction procedure. The effects observed from individual systematic checks are described below. The overall final systematic error bars are presented asymmetrically, that is, the positive differences and the negative differences were separately combined in quadrature. Individual checks accounted for different sources of possible uncertainty, however no account was taken of correlations between systematic effects.

7.5.1 Event Reconstruction and Selection

The event selection procedure was tested by tightening individual selection cuts in turn and then proceeding with the remainder of the analysis unchanged. Due to the offline bit selection used in selecting the data, it was not possible to check the effect of loosening the selection cuts. The variations made were :

- The cut on the lowest accepted value of $\delta = E - p_z$ was raised from 35 GeV to 40 GeV, leading to < 1% changes in the measured x_p and $\ln\left(\frac{1}{x_p}\right)$ values.

- The cut on y_e was lowered from 0.95 to 0.8. The change introduced small changes, $\lesssim 2\%$, across the x_p and $\ln\left(\frac{1}{x_p}\right)$ distributions in bins 11, 12 and 13.

- The cut on y_{JB} was increased from 0.04 to 0.05. The values of x_p and $\ln\left(\frac{1}{x_p}\right)$ measured in bins at low y exhibited scattered variations at the level of $\sim 1\%$.

- The analysis was repeated without the use of noise suppression for the calorimeter cells; this increases the sensitivity to low energy hadronic deposits used in the reconstruction of x and Q^2. Removing the suppression altogether is an extreme approach to checking the systematic, but the results reveal that the energy weighted angle γ_h used in the Double Angle reconstruction (see section 4.2.3) is little influenced by any mismatch between the data and Monte Carlo caused

by the modelling of the low energy deposits. Bins 2, 3, 5, 6 and 9 (i.e. the lowest y bins) were the most affected. In these bins there was a reduction in cross-section of about 5% across the x_p spectrum, except for bins 2 and 5 where the multiplicity fell by as much as 10%. The slopes of the distributions were not affected. Similarly, the $\ln\left(\frac{1}{x_p}\right)$ distributions in the affected bins had lower peaks, although there was no influence on the position of the peak.

- A cut was added to test the effect of diffractive events by discarding events possessing a Large Rapidity Gap (LRG). The cut was made by demanding that the most forward energy deposit in the event be found at a pseudorapidity > 1.5. This change in the analysis produced slight random fluctuations in the measurement of the order of $< 2\%$ in the bins with $x < 2.4 \times 10^{-3}$.

- The kinematic variables were reconstructed using the p_T/Σ method, rather than the Double Angle method. This results in one of the largest systematic effects and the resulting spectra are therefore compared with the central results in figure 7.9. As the figure illustrates, bins 7 and 9 show the largest variations: here the slopes of the x_p spectra have become slightly flattened. This is reflected in the influence on the leading slope of the $\ln\left(\frac{1}{x_p}\right)$ distributions evident in figure 7.10.

7.5.2 Track Reconstruction and Selection

- The track p_T cut was lowered from $p_T > 0.2$ GeV to $p_T > 0.15$ GeV and the track η cut was changed from $|\eta| < 1.75$ to $|\eta| < 1.5$. In general, the change produced distributions very little different overall ($< 1\%$), except in the region of low Q^2 and $x_p < 0.05$ ($\sim 5\%$ effect), and in bin 13 where the $x_p > 0.4$ bins showed a $\sim 10\%$ decrease.

- 20% (randomly assigned) of the tracks associated with the primary vertex were reconstructed using kaon mass, producing 2 to 3 % fluctuations in the measured distributions.

- Tracks were no longer required to belong to the primary vertex but were accepted from any vertex with an additional requirement that they begin in Superlayer 1

and end beyond Superlayer 3. The primary vertex cut was required in 1994 in order to reject poorly-reconstructed or false tracks. The tracking improved significantly after 1994 so that this restriction was no longer strictly necessary provided that sufficiently long tracks are used. The distributions showed an overall increase in cross-sections of 5 to 15%, higher in the higher Q^2 bins where the multiplicity is so much larger. The effect was fairly flat across the x_p range. The effects of this systematic change on the distributions are shown in figures 7.11 and 7.12.

7.5.3   Monte Carlo Generator

As noted earlier, ARIADNE provides the best overall description of the data. However, as a systematic check, the data were also corrected using HERWIG. As explained in chapter 5, the HERWIG Monte Carlo sample used was generated without interface to HERACLES so that it contains no initial state or final state QED radiation: thus this systematic check is also sensitive to the effects of QED radiation on the measurement. This proved to be one of the largest systematic effects. The effects on the measured distributions are shown in figures 7.13 and 7.14. At lower Q^2 there appears to be a tendency for points at low x_p to be reconstructed lower when using HERWIG and for points at high x_p to be higher. At higher Q^2 the data are consistent within statistical errors.

7.6   Summary

The method by which the raw data were corrected and combined has been described, and an account has been given of the studies of systematic effects on the measurements. The final corrected data distributions are shown in figures 7.15 and 7.16 with statistical and systematic error bars. The inner error bars denote the statistical errors on the measurement whilst the outer error bars represent the statistical and systematic errors combined in quadrature. The dominant systematics are those arising from using a different Monte Carlo model to correct the data, and from using all tracks rather than restricting the study to those tracks assigned to the primary vertex.

The x_p spectra exhibit a rise in particle production for low values of x_p ($x_p <$ 0.1) with Q^2, and a gradual fall with Q^2 in the production of particles with large x_p ($x_p > 0.4$). The $\ln\left(\frac{1}{x_p}\right)$ distributions also demonstrate the increase in soft particle production with increasing Q^2, and the peaks of the distributions can be seen to evolve with increasing energy.
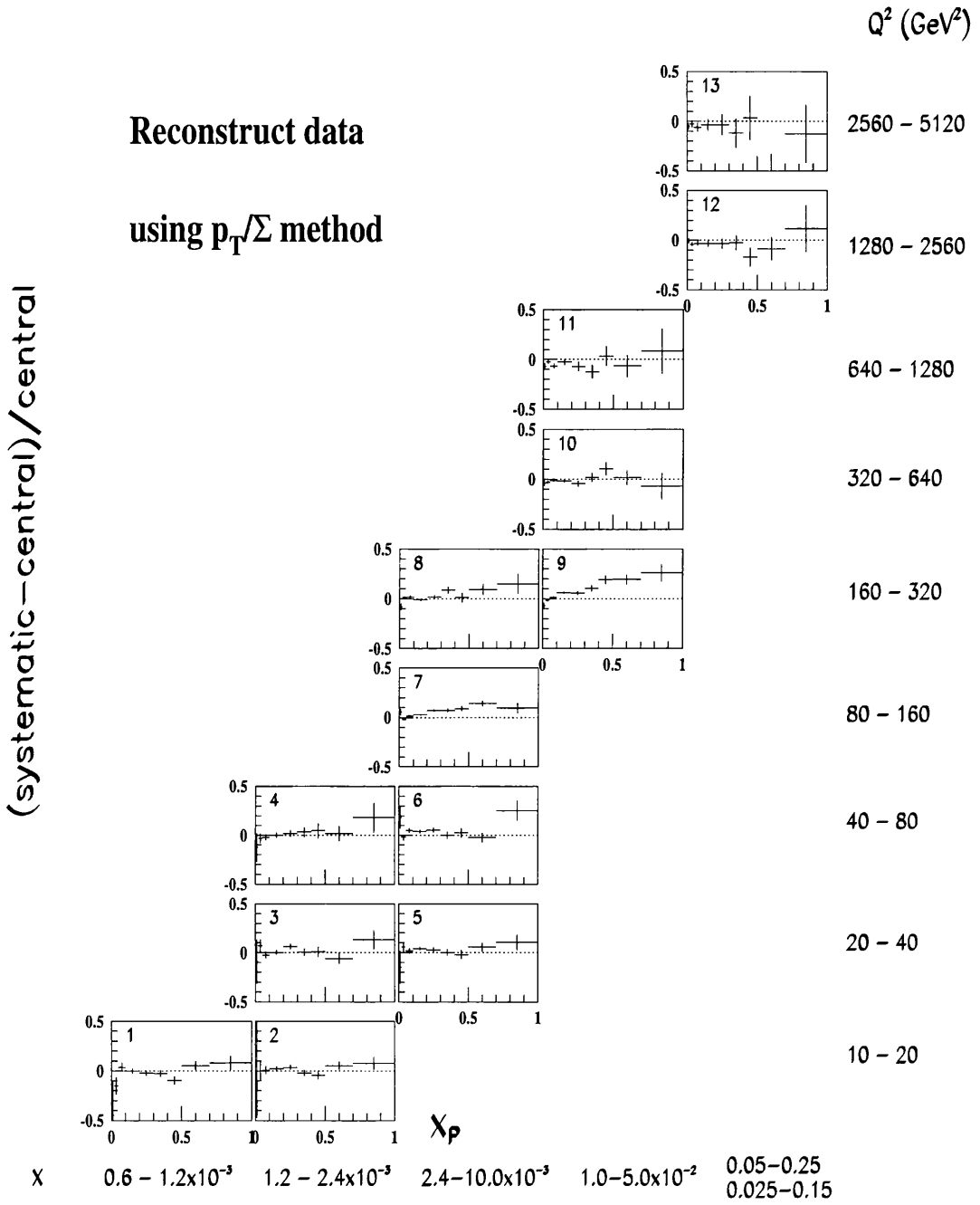
Figure 7.9: The systematic effects on the measured x_p due to using a different reconstruction method for the kinematic variables.
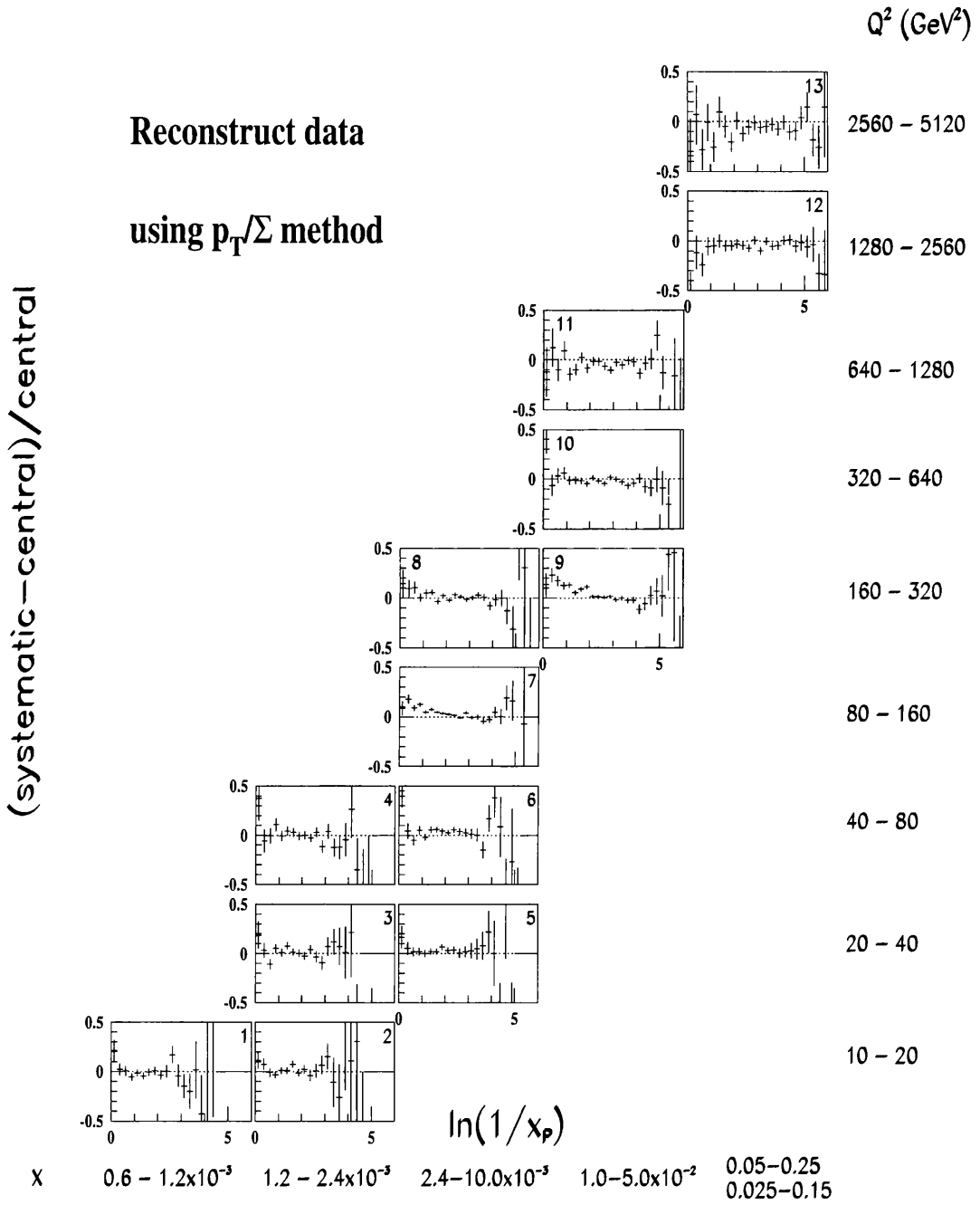
Figure 7.10: The systematic effects on the measured $\ln\left(\frac{1}{x_p}\right)$ due to using a different reconstruction method for the kinematic variables.

Figure 7.11: The systematic effects on the measured x_p due to accepting tracks from any vertex.
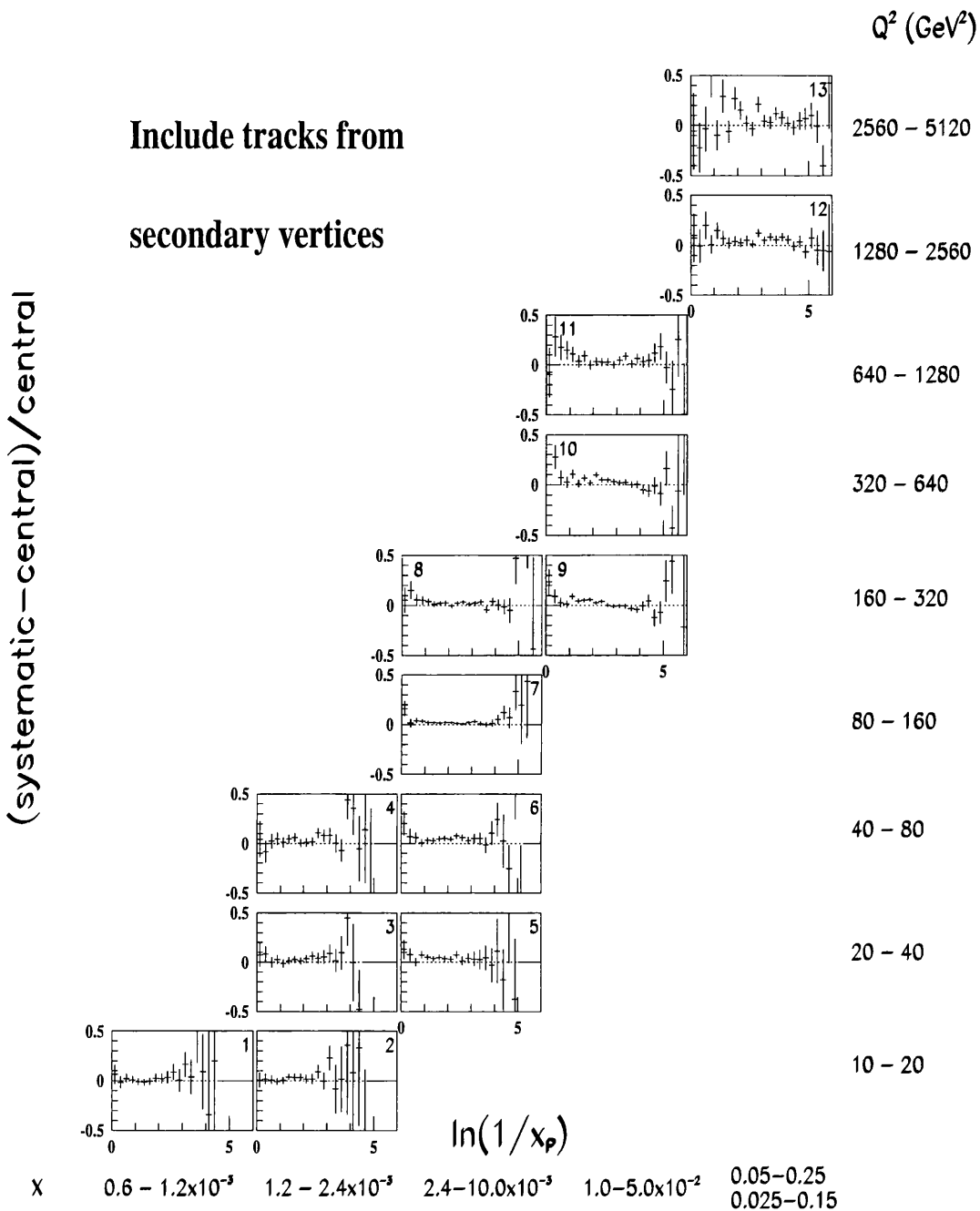
Figure 7.12: The systematic effects on the measured $\ln\left(\frac{1}{x_p}\right)$ due to accepting tracks from any vertex.

Figure 7.13: The systematic effects on the measured x_p due to using a different Monte Carlo model to correct the data.
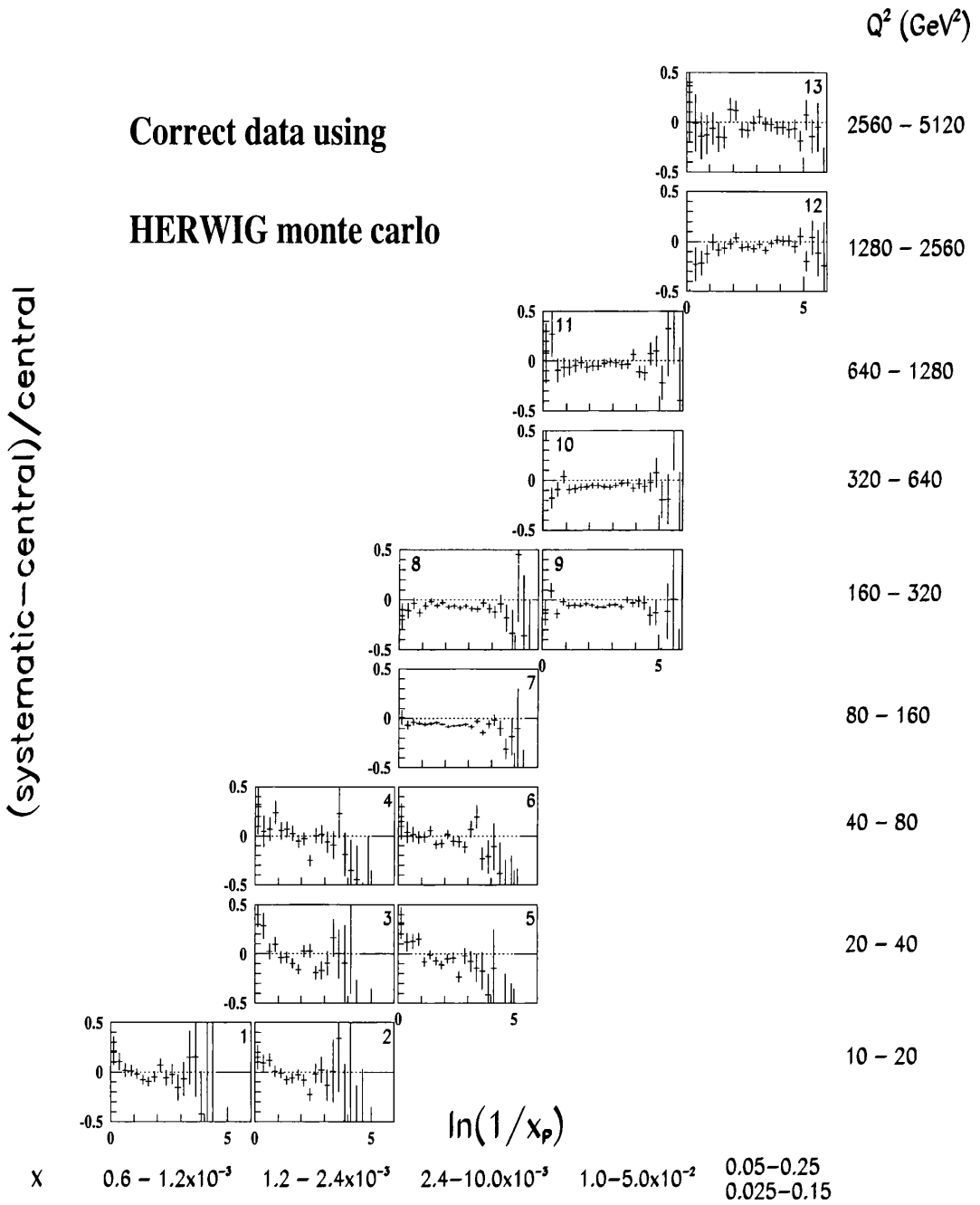
Figure 7.14: The systematic effects on the measured $\ln\left(\frac{1}{x_p}\right)$ due to using a different Monte Carlo model to correct the data.
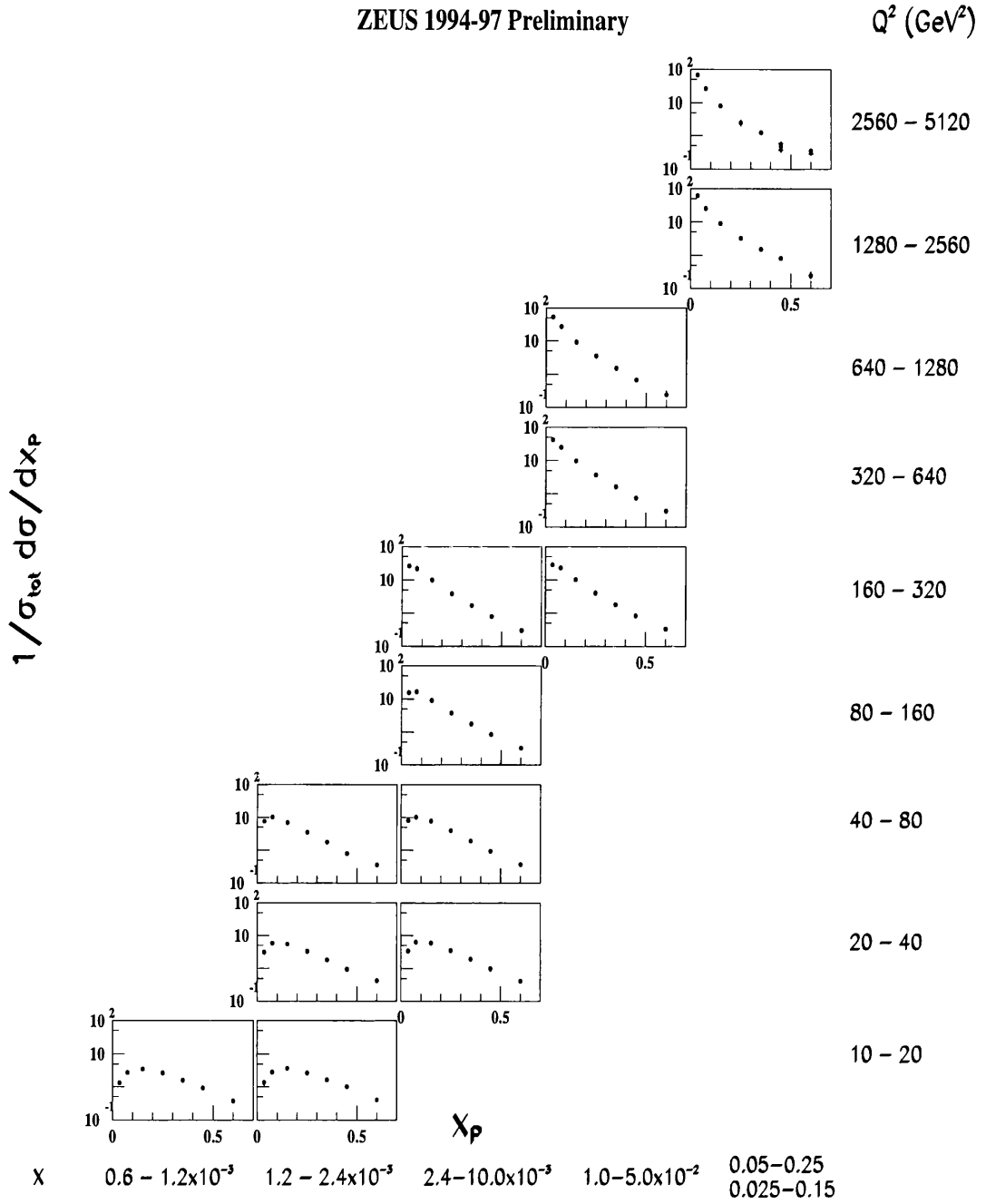
Figure 7.15: The corrected x_p distributions: the inner error bars denote the statistical errors while the outer error bars represent the statistical and systematic errors combined in quadrature.
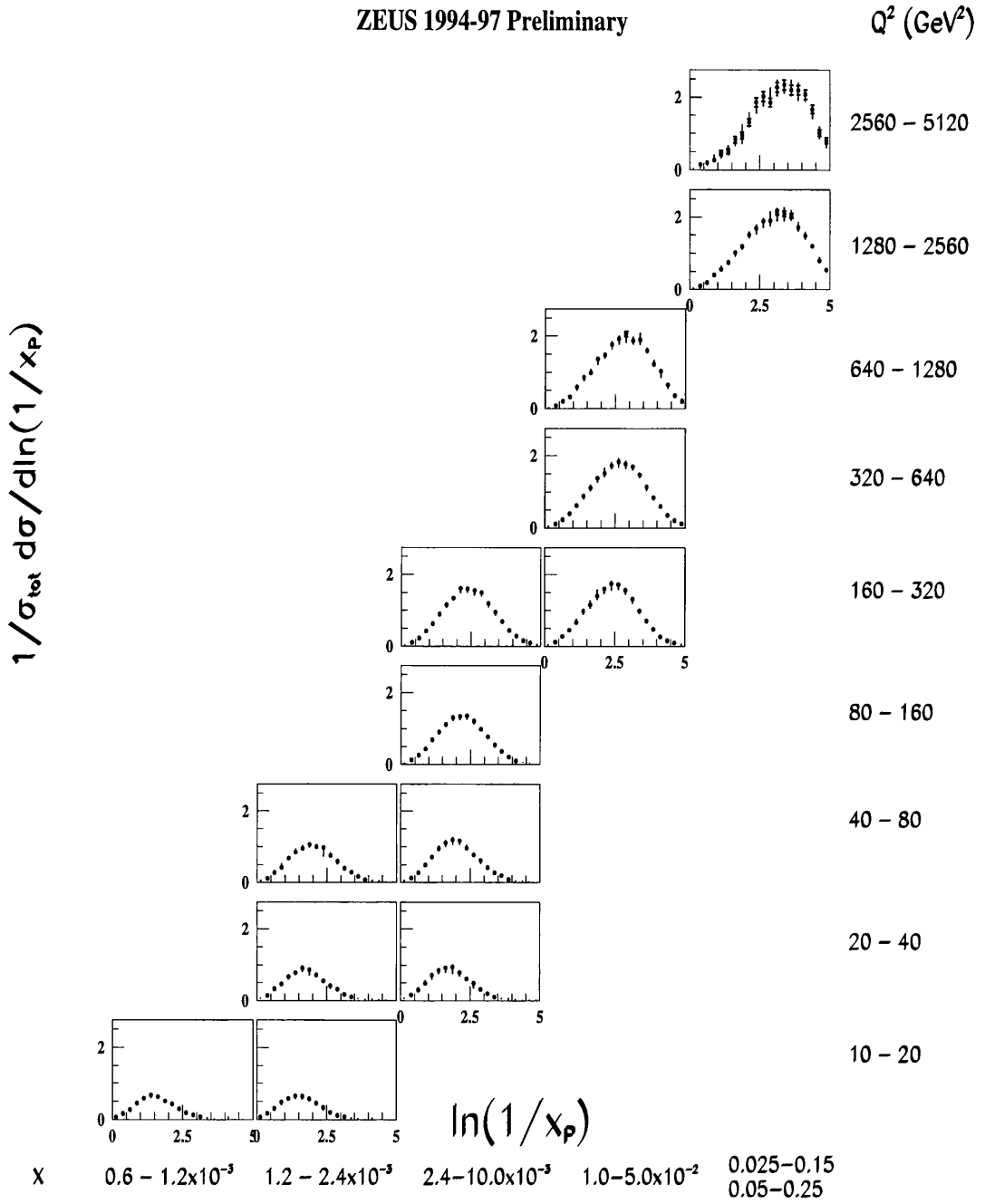
Figure 7.16: The corrected $\ln\left(\frac{1}{x_p}\right)$ distributions: the inner error bars denote the statistical errors while the outer error bars represent the statistical and systematic errors combined in quadrature.

Chapter 8

Comparison with Theory

Once the distributions have been corrected they can be compared with results from other experiments and with theoretical predictions. Inclusive scaled momentum distributions can be modelled using a combination of perturbative calculations and non-perturbative techniques. In this chapter the corrected x_p data are compared with results from e^+e^- annihilation experiments and also with the results of a NLO calculation. The feasibility of extracting a value for α_s by fitting the evolution of the x_p distributions with Q^2 is investigated.

QCD not only predicts the shape of the $\ln\left(\frac{1}{x_p}\right)$ spectra, but also describes their evolution with energy. In this chapter the measured distributions are fitted using an analytical form predicted by the MLLA, and their evolution with Q^2 is studied in comparison with that observed at e^+e^- experiments.

8.1 Fitting the $\ln\left(\frac{1}{x_p}\right)$ distributions

Figure 8.1 shows the corrected $\ln\left(\frac{1}{x_p}\right)$ distributions for charged particles obtained from ZEUS 1994-7 data in the (x,Q^2) bins defined in chapter 4. Where there are two bins with the same Q^2 range, only the bin with the higher x range is shown. The vertical error bars represent statistical errors only; the horizontal error bars indicate the widths of the bins in $\ln\left(\frac{1}{x_p}\right)$. Points are plotted at the bin centres. The mean Q of each (x,Q^2) bin is indicated in the figure. The distributions are roughly Gaussian, whose maxima progressively shift towards higher values of $\ln\left(\frac{1}{x_p}\right)$ as the energy increases.

126

ZEUS 1994-97 Preliminary
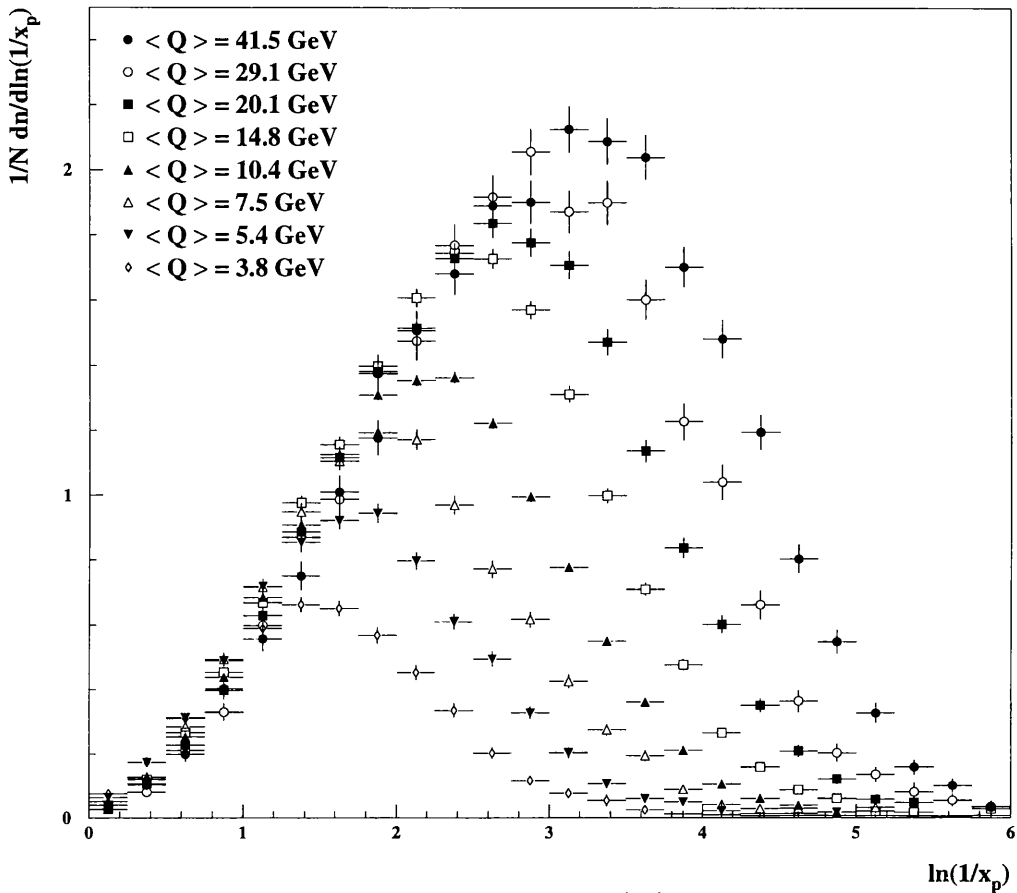
Figure 8.1: Evolution of $\ln\left(\frac{1}{x_p}\right)$ with Q^2.

The gradual growth in the heights of the distributions reflects the rise in multiplicity with Q. The distributions also widen as Q increases, changing by about a factor 2 between the lowest and highest Q bins. The spectra in the lowest Q^2 bins are skew with a tail extending to high $\ln\left(\frac{1}{x_p}\right)$; the tail grows smaller as Q^2 increases and for $< Q > \gtrsim 10$ GeV the distributions appear almost completely symmetrical (see also figure 8.2).

The rising edges of the distributions at low $\ln\left(\frac{1}{x_p}\right)$ are almost concurrent - the small variations mirror the scaling violations observed at high x_p. The distributions are expected to fall to zero for $\ln\left(\frac{1}{x_p}\right) = 0$. That they do not do so is a result of intrinsic p_T in the proton which leads to particles being measured with $x_p > 1$

(i.e. $\ln(1/x_p) < 0$), and hence to increased cross-sections in the high x_p ($x_p > 0.7$) and low $\ln\left(\frac{1}{x_p}\right)$ ($\ln(1/x_p) \lesssim 0.5$) regions. Thus the fits subsequently performed on the distributions disregard $\ln\left(\frac{1}{x_p}\right) < 0.5$.

There are several alternatives by which these distributions can be fitted with theoretical predictions. The modified leading log approximation (MLLA) predicts the shape of the distributions and is available in a form suitable for numerical integration, so that individual spectra can be directly fitted in terms of two free variables, Λ_{eff} and κ. The MLLA also predicts the way in which the spectra are expected to develop with increasing energy, so that measurements at different values of Q can be combined and their evolution fitted with the theoretical description as a cross-check. In the following sections these alternatives are studied to confront the predictions of the MLLA model from different perspectives.

8.1.1 MLLA prediction

The MLLA predicts - for high energies and momenta in the relativistic limit - the form of the scaled momentum distribution of soft gluons radiated by a quark with energy E [23]. Known as the limiting spectrum, the analytical formula (in a form suitable for numerical integration) is given by

$$\bar{\mathcal{D}}^{\text{lim}}\left(\ln\left(\frac{1}{x_p}\right), Y\right) = \frac{4N_c}{b}\Gamma(B)\int_{\frac{-\pi}{2}}^{\frac{\pi}{2}}\frac{d\tau}{\pi}e^{-B\alpha}\left[\frac{\cosh\alpha + (1-2\zeta)\sinh\alpha}{\frac{4N_c}{b}Y\frac{\alpha}{\sinh\alpha}}\right]^{B/2}$$
$$\cdot I_B\left(\sqrt{\frac{16N_c}{b}Y\frac{\alpha}{\sinh\alpha}\left[\cosh\alpha + (1-2\zeta)\sinh\alpha\right]}\right) \quad (8.1)$$

with $Y = \ln(E/2\Lambda_{\text{eff}})$, where Λ_{eff} is an effective scale parameter (only indirectly related to $\Lambda_{\overline{MS}}$, for instance). In the case of DIS in the current fragmentation region of the Breit Frame, $E = Q/2$, while for e^+e^- annihilation $E = \sqrt{s}/2$.

The variable $\alpha = \alpha_0 + i\tau$, and α_0 is determined from $\tanh\alpha_0 = 2\zeta - 1$, ζ being defined as $\zeta = 1 - \ln\left(\frac{1}{x_p}\right)/Y$. Γ denotes the Gamma function and I_B is a modified Bessel function of order B. The remaining constants, N_c, N_f, b, B are based on the numbers of colours and flavours: N_c is the number of colours, and b and B are given by $b = \frac{11}{3}N_c - \frac{2}{3}N_f$ and $B = \left(\frac{11}{3}N_c + \frac{2}{3}N_f/N_c^2\right)/b$, where N_f is the number of active flavours. Since the light quarks are expected to dominate quark pair production in the

gluon cascade, the formula was implemented with $N_f = 3$. For N_f and $N_c = 3$, the constants b and B are 9 and 1.247 respectively.

This limiting spectrum produces the characteristic "hump-backed plateau". Since the above expression models the behaviour of gluons, an additional coefficient factor $C_f/N_c = 4/9$ is applied in order to predict the form of the distribution for quarks. Following LPHD an overall normalisation factor, κ, is used to describe the transformation from partons to hadrons. This is not expected to vary with energy. The only free parameters in equation 8.1 are therefore Λ_{eff} and κ. Fits of this formula performed to data gathered at other experiments have obtained values of κ in the range 1.2 - 1.5 and Λ_{eff} between 200 and 300 MeV [64].

Numerical integration was performed to fit this expression to the inclusive scaled momentum distributions (with the combined statistical and systematic errors) in each (x, Q^2) bin. The form of the MLLA is valid for $p \gtrsim \Lambda_{\text{eff}}$, that is, $\ln\left(\frac{1}{x_p}\right) \lesssim \ln\frac{Q}{2\Lambda_{\text{eff}}}$; accordingly the fits were restricted to data within this region. The resulting curves are presented in figure 8.2, where the inner error bars (these are largely within the scope of the points) indicate the statistical errors and the outer error bars show the statistical and systematic errors combined in quadrature. The data are shown to be well described both around the peak and in the general shape, although in some bins the curves fail to describe the gradient of the falling edge of the distribution. Fitting was found to be difficult in the low Q^2 bins where the $\ln\left(\frac{1}{x_p}\right) < \ln\frac{Q}{2\Lambda_{\text{eff}}}$ restriction left few points available for the fit, and the adding or discarding of points at high $\ln\left(\frac{1}{x_p}\right)$ as Λ_{eff} was varied led to multiple minima in the χ^2/ndf.

The fitted values of κ and Λ_{eff} are given in table 8.1 (with statistical errors only). In the range $80 \lesssim Q^2 \lesssim 1280 \text{ GeV}^2$, the data indicate a consistent picture with $\kappa \sim 1.3$ and $\Lambda_{\text{eff}} \sim 250$ MeV. For $Q^2 \lesssim 80 \text{ GeV}^2$ there were generally insufficient degrees of freedom available in the fit for a reliable result, and the points included barely reach over the peaks of the distributions, so that the fit cannot be expected to obtain a representative picture of the distributions. A comparison of the values given in the table with the curves in figure 8.2 reveals that these are the bins in which the fitted curves fall off more steeply than the data. In the bins for $Q^2 \gtrsim 1000 \text{ GeV}^2$, κ and Λ_{eff} seem to begin to fall off. This may echo a trend for the charged multiplicity to fall below the expected

x range	Q^2 range	$<Q>$	κ	Λ_{eff} (MeV)	χ^2/ndf
$0.6 - 1.2 \ 10^{-3}$	10 - 20	3.8	$0.95 \pm .08$	322 ± 13	0.2/4
$1.2 - 2.4 \ 10^{-3}$	10 - 20	3.8	$0.97 \pm .12$	280 ± 4	2/5
	20 - 40	5.3	$1.12 \pm .10$	291 ± 2	2/5
	40 - 80	7.4	$1.18 \pm .11$	344 ± 8	1/6
$2.4 - 10. \ 10^{-3}$	20 - 40	5.4	$1.19 \pm .17$	335 ± 63	0.4/5
	40 - 80	7.5	$1.30 \pm .12$	301 ± 30	0.3/6
	80 - 160	10.4	$1.29 \pm .03$	258 ± 6	3/8
	160 - 320	14.5	$1.32 \pm .07$	256 ± 4	2/9
$1.0 - 5.0 \ 10^{-2}$	160 - 320	14.8	$1.40 \pm .19$	254 ± 48	2/9
	320 - 640	20.1	$1.33 \pm .11$	253 ± 7	3/10
	640 - 1280	29.1	$1.24 \pm .08$	238 ± 1	4/12
0.025 - 0.15	1280 - 2560	41.5	$1.20 \pm .10$	237 ± 1	7/13
0.05 - 0.25	2560 - 5120	59.1	$1.12 \pm .17$	227 ± 6	4/15

Table 8.1: Results of fitting the analytical form of the MLLA to the fragmentation spectra.

values in this region (see section 8.2). The results represent a fairly consistent account of Λ_{eff} and κ for $Q \gtrsim 10$ GeV, with Λ_{eff} asymptotically ~ 250 MeV and $\kappa \sim 1.3$.

8.1.2 Evolution with energy

For asymptotic energies E and close to the peak in the inclusive momentum spectrum, equation 8.1 can be approximated to a Gaussian distribution thus

$$\frac{1}{\sigma}\frac{d\sigma}{d\ln\left(\frac{1}{x_p}\right)} = \mathcal{N}(Y)\left(\frac{36N_c}{\pi^2 b Y^3}\right)^{1/4}\exp\left[-\sqrt{\frac{36N_c}{b}}\frac{\left(\ln\left(\frac{1}{x_p}\right) - \ln\left(\frac{1}{x_p}\right)_{max}\right)^2}{Y^{3/2}}\right]$$

where Y, b, N_c are defined in the section above and $\mathcal{N}(Y)$ is the average charged particle multiplicity which is predicted by theory. The position of the peak of the distribution, $\ln\left(\frac{1}{x_p}\right)_{max}$, is predicted to evolve with energy as

$$\ln\left(\frac{1}{x_p}\right)_{max} = \frac{1}{2}Y + \sqrt{cY} - c + \mathcal{O}(Y^{-1/2}) \tag{8.2}$$

x range	Q^2 range	$<Q>$	RMS	$\ln\left(\frac{1}{x_p}\right)_{max}$ $\pm$ stat $\pm$ systematic	χ^2/ndf
$0.6 - 1.2 \ 10^{-3}$	10 - 20	3.8	$0.69 \pm .02$	$1.50 \pm .01 \pm .03$	11/6
$1.2 - 2.4 \ 10^{-3}$	10 - 20	3.8	$0.72 \pm .02$	$1.50 \pm .01 \pm .07$	5/6
	20 - 40	5.3	$0.77 \pm .02$	$1.70 \pm .02 \pm .03$	10/6
	40 - 80	7.4	$0.86 \pm .03$	$1.94 \pm .02 \pm .08$	2/6
$2.4 - 10. \ 10^{-3}$	20 - 40	5.4	$0.77 \pm .02$	$1.72 \pm .01 \pm .08$	10/6
	40 - 80	7.5	$0.82 \pm .02$	$1.92 \pm .01 \pm .04$	9/6
	80 - 160	10.4	$0.88 \pm .01$	$2.18 \pm .01 \pm .02$	5/6
	160 - 320	14.5	$0.94 \pm .02$	$2.41 \pm .01 \pm .04$	13/6
$1.0 - 5.0 \ 10^{-2}$	160 - 320	14.8	$0.93 \pm .02$	$2.43 \pm .01 \pm .07$	21/6
	320 - 640	20.1	$1.03 \pm .03$	$2.67 \pm .02 \pm .06$	9/6
	640 - 1280	29.1	$1.07 \pm .04$	$2.88 \pm .03 \pm .11$	11/6
0.025 - 0.15	1280 - 2560	41.5	$1.22 \pm .06$	$3.15 \pm .04 \pm .10$	9/6
0.05 - 0.25	2560 - 5120	59.1	$1.43 \pm .17$	$3.38 \pm .07 \pm .08$	8/6

Table 8.2: Positions of the maxima in the inclusive momentum spectra obtained using a restricted Gaussian fit.

where $c = \frac{11}{48}\frac{(1+2N_f/11N_c^3)^2}{1-2N_f/11N_c} = 0.29 \ (0.35)$ for $N_f = 3 \ (5)$ and $\mathcal{O}(Y^{-1/2})$ represents higher order corrections. Thus the evolution with Q of the peak in the inclusive momentum distribution depends - higher order terms apart - solely on the parameter Λ_{eff}.

The $\ln\left(\frac{1}{x_p}\right)$ distributions were fitted with a Gaussian over a range of $\pm\sigma_{\text{RMS}}$ around the arithmetic means of the distributions (where σ_{RMS} is the RMS of the distribution) in order to find the peak positions. The data were refitted for each of the systematic checks noted in section 7.5. In addition, the dependence of the Gaussian fit on the chosen fit range was examined: the range was increased and decreased by one bin on either side of the mean and the change that gave the largest difference in the position of the peak was incorporated into the systematic error. The final errors combined the positive and negative deviations in quadrature.

The positions of the maxima of the distributions are plotted as a function of $<Q>$ in figure 8.3; also shown in this figure are results from other DIS experiments and e^+e^-

annihilation experiments fitted in the same way. The agreement is good - all points lie on the same line of evolution. The dashed line (with a slope of 1) in figure 8.3 indicates the predicted evolution of the maximum in the momentum spectrum for incoherent parton showering, that is, if soft gluons in the parton shower were allowed to radiate anywhere within a cylindrical phase space and with no consideration of interference terms. Fitting equation 8.2, where the higher order term is neglected, to the data (including only the statistical contributions to the errors) yields $\Lambda_{eff} = 247 \pm 2 \pm 9$ MeV with $\chi^2/\text{ndf} = 38/11$. The stated systematic error accounts only for experimental uncertainties; no estimate of the theoretical uncertainty has been made. This value of Λ_{eff} concurs well with that found by fitting the analytical formula to the distributions.

8.1.3 Skewed Gaussian fits

The $\ln\left(\frac{1}{x_p}\right)$ distributions in figure 8.1 are clearly not symmetrical in some (x,Q^2) bins - particularly for $Q^2 < 100$ GeV^2, where the spectra are positively skewed[1] - so that fitting them with a Gaussian runs the danger of obtaining a value for the peak which has been pulled by the skewness of the curve. An alternative approach is to use an approximation to the MLLA prediction given in the form of a distorted Gaussian [65]:

$$\frac{1}{\sigma}\frac{d\sigma}{d\ln(x)} \approx \frac{N(Y)}{\sigma\sqrt{2\pi}} \times exp\left[\frac{1}{8}k - \frac{1}{2}s\delta - \frac{1}{4}(2+k)\delta^2 + \frac{1}{6}s\delta^3 + \frac{1}{24}k\delta^4\right] \qquad (8.3)$$

where $\delta = \left[\ln(1/x) - \overline{\ln(1/x)}\right]/\sigma$, and the coefficients $N(Y)$, σ, s and k are the average multiplicity, the width, skewness and kurtosis of the Gaussian-like momentum spectrum and are calculated to next-to-leading order (with s and k small). Table 8.3 contains the peak positions found by fitting the distributions over approximately 1 unit around the mean with this form, compared with the results from the Gaussian fits. The numbers given in brackets are the values of χ^2/ndf. Given the bin-sizes in $\ln\left(\frac{1}{x_p}\right)$ and the narrowness of the distributions in comparison with those at higher energies, there were difficulties with fitting an expression with so many degrees of freedom with confidence. Since the kurtosis was found to be consistent with zero within statistical errors, the data were fitted with a skewed Gaussian with no kurtosis.

---

[1] where skewness $s \equiv \overline{(x-\bar{x})^3}/\sigma^3$.

The values found for the maxima in the distributions agree reasonably well with the results of the symmetrical Gaussian fit within statistical errors for $Q \gtrsim 10$ GeV, but diverge at lower Q values where the data are positively skew. When the distributions from e^+e^- experiments are treated in the same way, the resulting maxima do not vary beyond the bounds of the statistical error. The maxima from the skew fit (shown in figure 8.4) lie only approximately on a straight line: fitting the MLLA prediction for the evolution of the peak with energy to these data gave a similar value of Λ_{eff} to the symmetrical fit ($\Lambda_{\mathrm{eff}} = 242 \pm 2$ MeV), but with $\chi^2/\mathrm{ndf} = 109/11$.

The skewness is positive at low values of Q, goes through zero as Q increases, and tends towards negative values at high Q. The MLLA predicts uniformly negatively skewed distributions: the positive skewness seen in the data at low values of Q may be the result of higher order effects [66].

$< Q >$	Gaussian fit		Skewed Gaussian fit			
	$\ln\left(\frac{1}{x_p}\right)_{max}$	(χ^2/ndf)	$\ln\left(\frac{1}{x_p}\right)_{max}$	(χ^2/ndf)	skewness	σ
3.8	$1.50 \pm .01$	$(11/6)$	$1.43 \pm .03$	$(3/5)$	$.55 \pm .25$	$.70 \pm .03$
3.8	$1.50 \pm .01$	$(5/6)$	$1.46 \pm .03$	$(3/5)$	$.27 \pm .20$	$.72 \pm .02$
5.3	$1.70 \pm .02$	$(10/6)$	$1.63 \pm .03$	$(4/5)$	$.64 \pm .39$	$.79 \pm .05$
7.4	$1.94 \pm .02$	$(2/6)$	$1.97 \pm .05$	$(2/5)$	$-.22 \pm .37$	$.88 \pm .06$
5.4	$1.72 \pm .01$	$(10/6)$	$1.67 \pm .03$	$(5/5)$	$.41 \pm .20$	$.77 \pm .02$
7.5	$1.92 \pm .01$	$(9/6)$	$1.88 \pm .02$	$(4/5)$	$.40 \pm .20$	$.81 \pm .02$
10.4	$2.18 \pm .01$	$(5/6)$	$2.19 \pm .01$	$(5/5)$	$-.08 \pm .10$	$.88 \pm .01$
14.5	$2.41 \pm .01$	$(13/6)$	$2.42 \pm .03$	$(12/5)$	$-.10 \pm .20$	$.94 \pm .02$
14.8	$2.43 \pm .01$	$(21/6)$	$2.49 \pm .02$	$(6/5)$	$-.63 \pm .21$	$1.00 \pm .05$
20.1	$2.67 \pm .02$	$(9/6)$	$2.73 \pm .02$	$(4/7)$	$-.64 \pm .26$	$1.09 \pm .06$
29.1	$2.88 \pm .02$	$(11/6)$	$2.91 \pm .04$	$(11/7)$	$-.17 \pm .26$	$1.07 \pm .03$
41.5	$3.15 \pm .03$	$(9/6)$	$3.21 \pm .04$	$(7/8)$	$-.54 \pm .34$	$1.25 \pm .07$
59.1	$3.38 \pm .07$	$(8/6)$	$3.43 \pm .05$	$(19/10)$	$-.58 \pm .32$	$1.16 \pm .07$

Table 8.3: Positions of the maxima in the inclusive momentum spectra from restricted Gaussian and skewed Gaussian fits. The errors shown are statistical only. The numbers in brackets indicate the values of χ^2/ndf obtained from the fit.
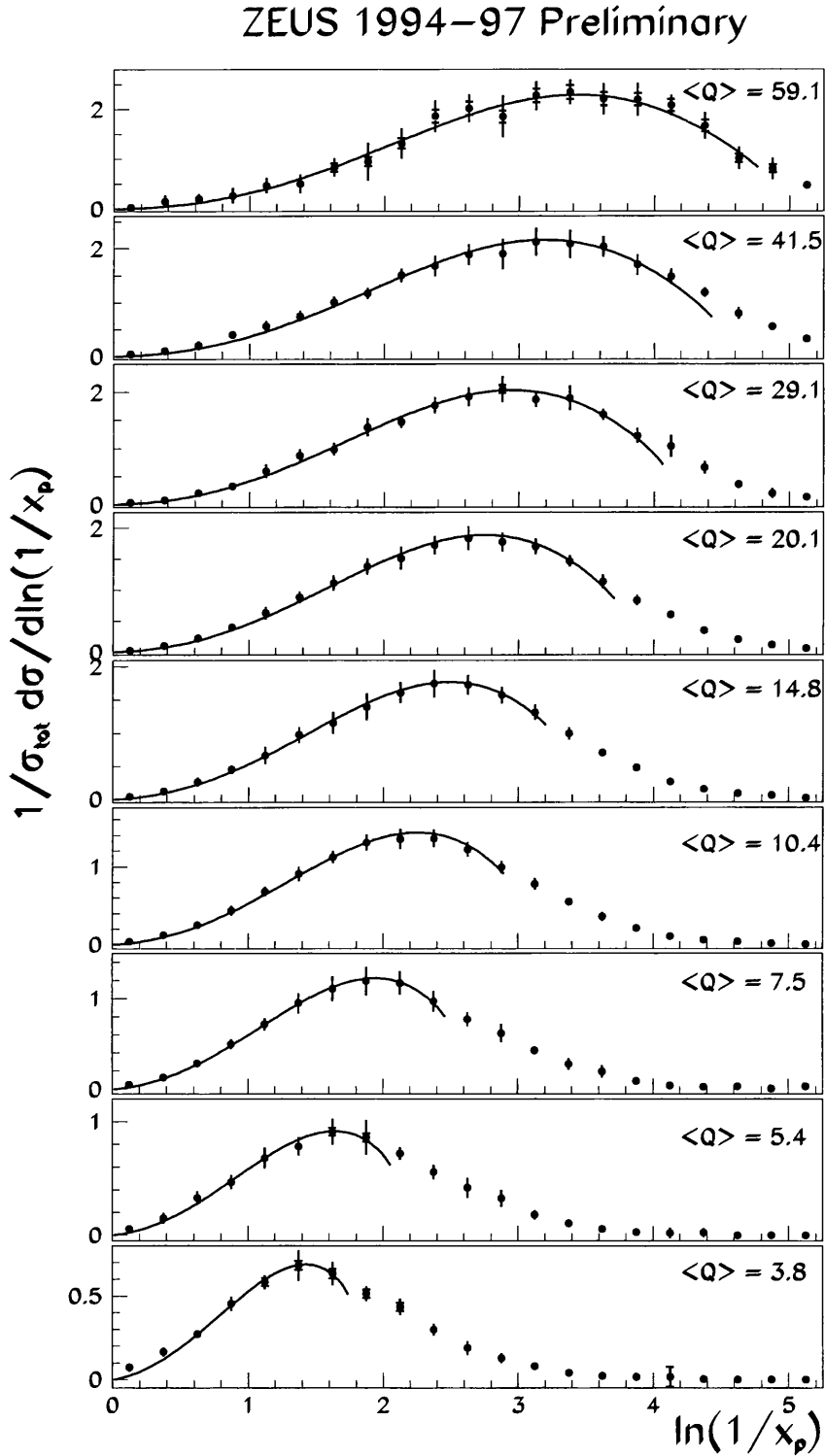
Figure 8.2: Fits of the analytical form of the MLLA to the fragmentation spectra. The inner error bars indicate the statistical errors (these are often hidden by the points), and the outer error bars show the statistical and systematic errors combined in quadrature.
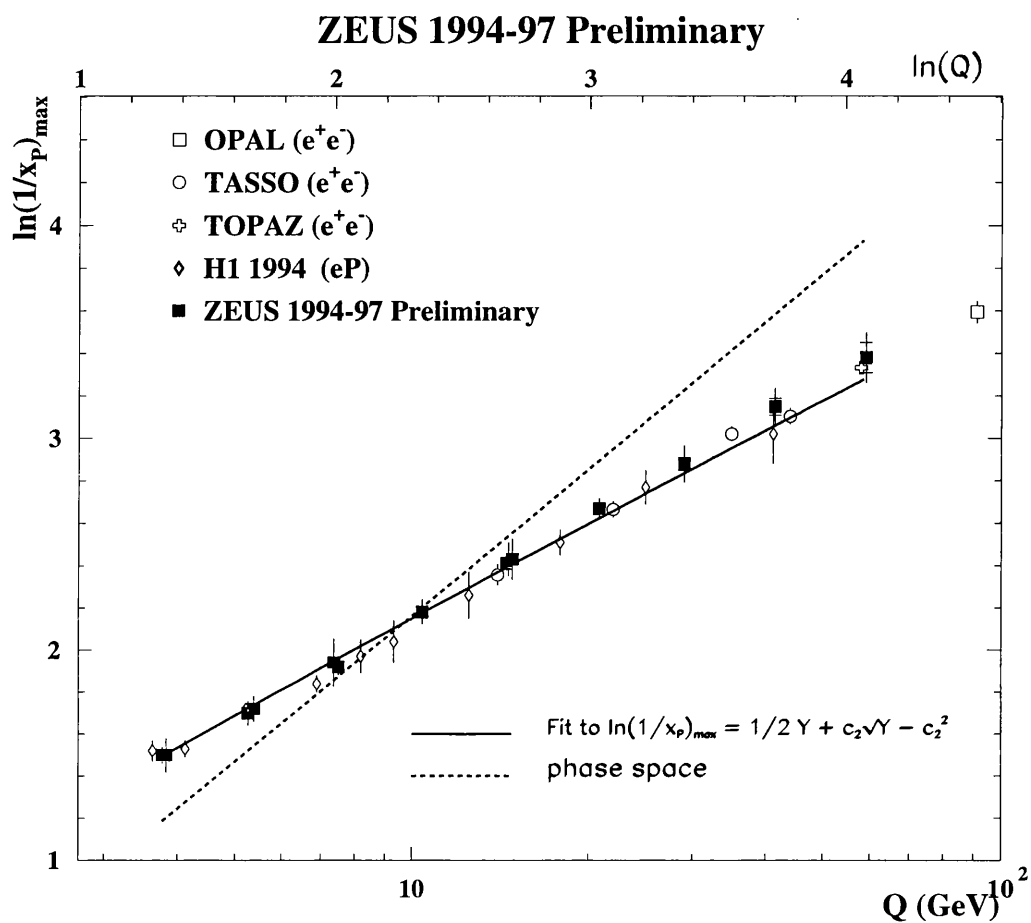
Figure 8.3: Evolution of $\ln\left(\frac{1}{x_p}\right)_{max}$ with Q^2, compared with results from H1 and e^+e^- results. The ZEUS data have been fitted with the MLLA prediction for the form of the evolution with energy.
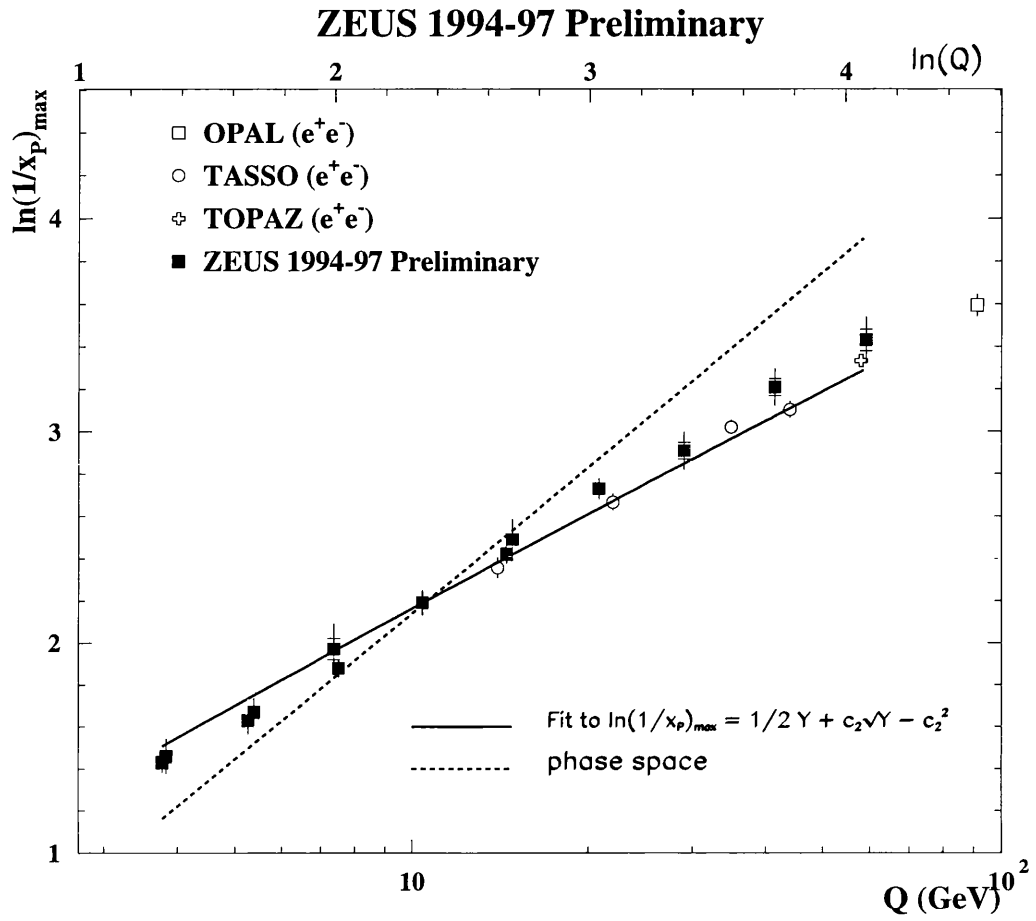
Figure 8.4: Evolution with energy of $\ln\left(\frac{1}{x_p}\right)_{max}$ found using a skewed Gaussian fit. The line indicates the result of fitting the MLLA prediction of the form of the energy evolution to the ZEUS data.

8.2 Evolution of the Mean Charged Multiplicity

The mean charged multiplicity in the current fragmentation region was found for each (x,Q^2) bin from the integral under the corrected $\ln\left(\frac{1}{x_p}\right)$ distributions. The results are shown in table 8.4. Over the range of Q^2 measured in the analysis, the multiplicity increases by a factor of about 6. The mean multiplicities measured in different x bins in the same Q^2 range are consistent within errors.

$< Q^2 >$	$< n > \pm$ stat $^{+\text{up systematic}}_{-\text{down systematic}}$
14.0	$1.16 \pm .01^{+.02}_{-.06}$
14.1	$1.21 \pm .01^{+.04}_{-.13}$
27.9	$1.67 \pm .02^{+.05}_{-.09}$
55.3	$2.19 \pm .03^{+.09}_{-.05}$
28.0	$1.80 \pm .02^{+.10}_{-.24}$
55.9	$2.39 \pm .02^{+.13}_{-.18}$
110.	$2.99 \pm .02^{+.11}_{-.20}$
216.	$3.75 \pm .04^{+.08}_{-.25}$
221.	$3.96 \pm .03^{+.16}_{-.33}$
443.	$4.54 \pm .04^{+.17}_{-.29}$
863.	$5.22 \pm .06^{+.23}_{-.31}$
1766.	$5.97 \pm .12^{+.30}_{-.35}$
3507.	$6.62 \pm .24^{+.38}_{-.57}$

Table 8.4: Mean multiplicity for charged particles

The results (scaled by a factor 2) were compared directly with inclusive mean multiplicity data from e^+e^- annihilation experiments at different values of $\sqrt{s}$, published in references [67, 68, 69, 70][2] and with fixed target data [71]. The data are compared in figure 8.5: the ZEUS and H1 mean charged multiplicities agree well, and in the region of overlap the DIS results are generally in good agreement with the e^+e^- results. The multiplicities from FNAL and MARK I (in the region $Q^2 \lesssim 50$ GeV^2) are somewhat

---

[2]These results excluded the products of K^0_S and Λ decays

higher than the HERA multiplicity points. This difference arises from the effects of massive kinematics at such low values of Q^2 leading to a depopulation of the current region, and reflects in particular the prevalence of the BGF diagram in DIS at low x, since BGF is not present in e^+e^- annihilation and the fixed target DIS experiments were carried out at values of x approximately two orders of magnitude higher than those accessible at HERA in this region of Q^2. As discussed in section 1.5, BGF tends to produce pairs of partons with a high invariant mass, $\hat{s}$, and when $\hat{s} \gtrsim Q^2$ this leads to depopulation of the current region via kinematic effects not seen in the massless approximation of the QPM. Thus there is a shortfall in the mean charged multiplicity measured in DIS at HERA with respect to charged multiplicities measured in DIS at higher x or in e^+e^- annihilation.

The two highest Q^2 points are observed to be $\gtrsim 1\sigma$ low with respect to the e^+e^- data. However, as can be seen in figure 8.6 - which compares the evolution in the charged multiplicity seen in the data with LO DIS Monte Carlos - these points are well described by ARIADNE. HERWIG agrees with the data at low Q but increases more quickly towards higher Q. LEPTO6.1 produces a charged multiplicity which is slightly higher than the data at low Q^2 and has a higher rate of increase in multiplicity with Q^2 towards high Q^2. LEPTO6.5 describes the data well at low Q^2 but then shows much too high a rate of increase with Q^2. The figure also shows the effect of generating Monte Carlo with no angular ordering in the parton shower and with independent fragmentation: the data clearly evolve along a shallower path than the incoherent prediction.

ZEUS 1994-97 Preliminary
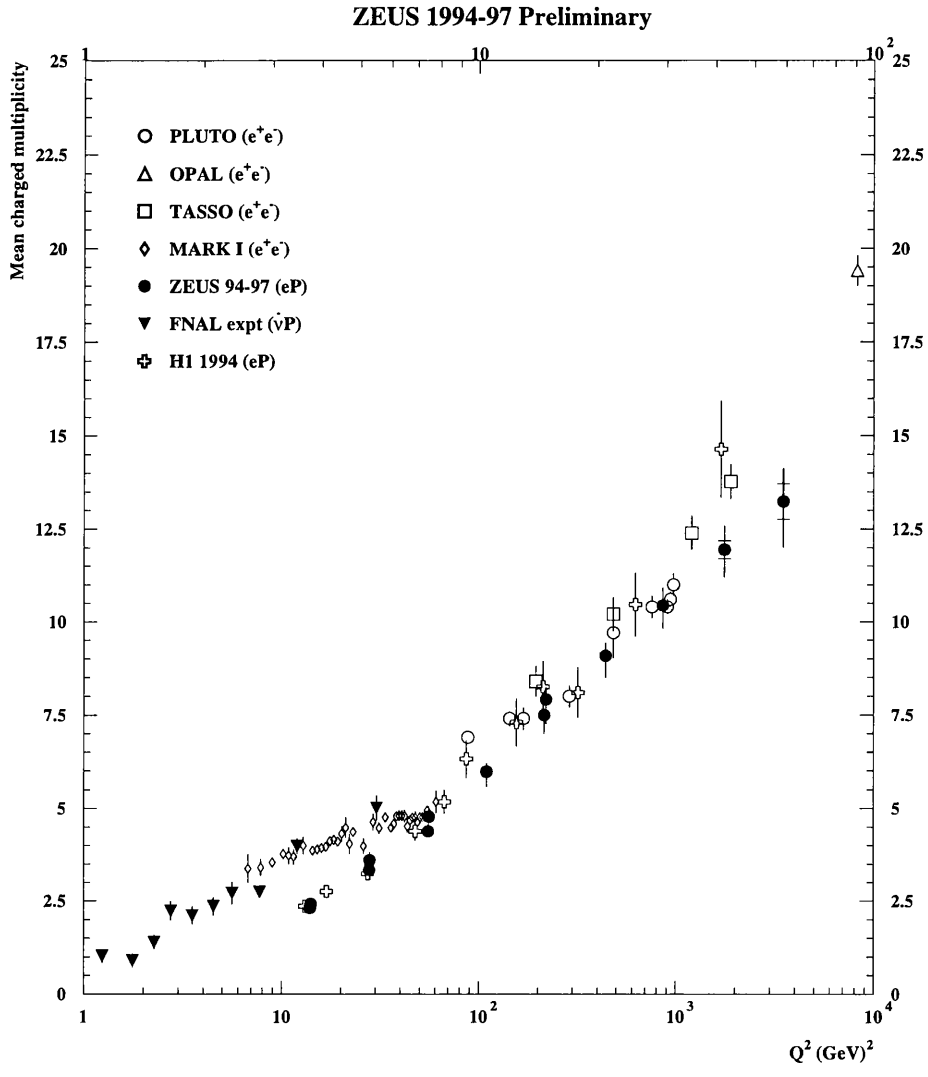
Figure 8.5: Evolution of the mean charged multiplicity with Q^2.

ZEUS 1994-97 Preliminary
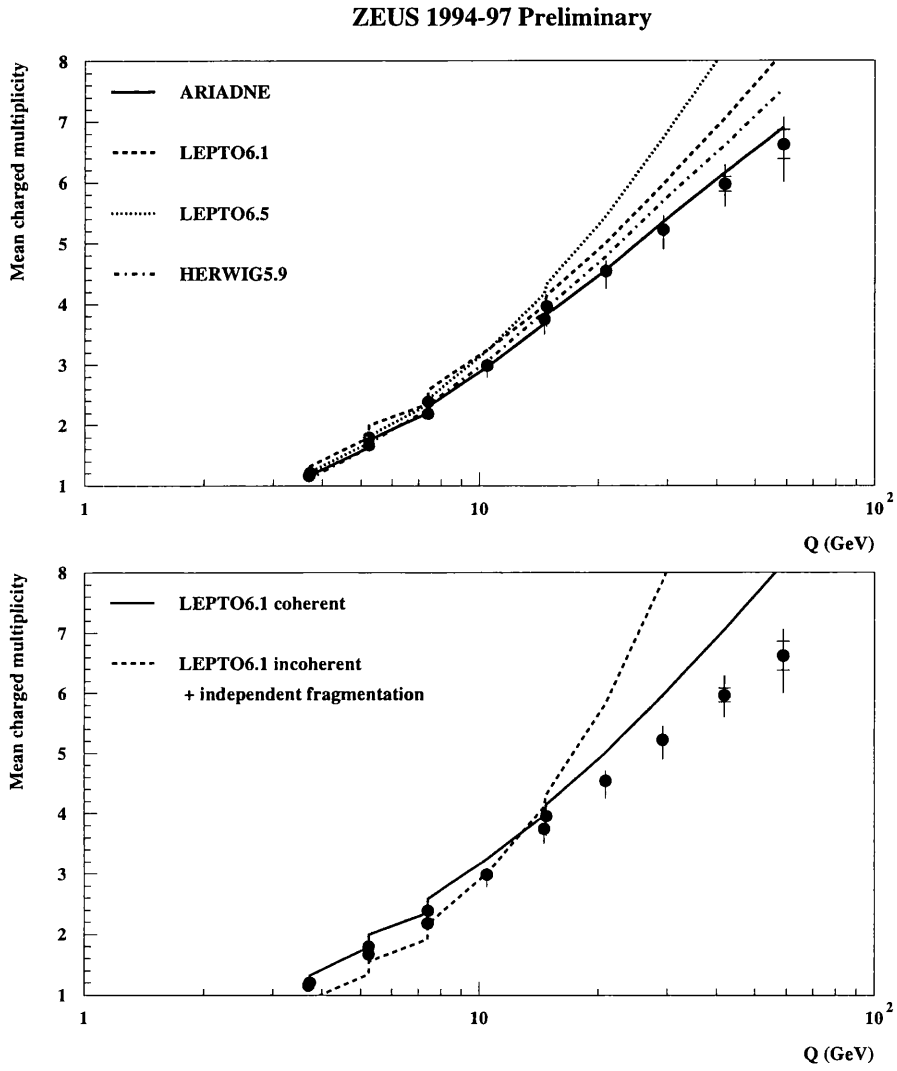
Figure 8.6: Evolution of the mean charged multiplicity with Q^2 compared with LO Monte Carlos.

8.3   Modelling the x_p evolution

The inclusive distribution $1/\sigma_{tot}\ d\sigma/dx_p$, where σ_{tot} is the DIS cross-section in the chosen (x,Q^2) bin, for charged particles measured from data taken by ZEUS in the 1994-97 data-taking periods are shown as a function of Q^2 in figure 8.7. The data are normalised to the number of events in the (x,Q^2) bin and to the binwidth in x_p. The inner thick error bars (where these are not visible they lie within the extent of the marker) denote the statistical errors on the points, while the outer thin error bars show the statistical and systematic errors combined in quadrature.

According to QCD the phase space for gluon radiation increases, and α_s runs, as Q^2 increases. Hence quarks at higher energies tend to emit more gluons, depopulating the high scaled momentum region whilst the soft gluons populate the low x_p area. This effect materializes in scaling violations when points of constant x_p are plotted as a function of Q^2.

The predicted scaling violations are revealed in figure 8.7: for $Q^2 \gtrsim 80$ GeV^2 the cross-section for low x_p ($x_p < 0.1$) rises with increasing Q^2, whilst that for large x_p values ($x_p > 0.5$) falls with increasing Q^2. For $Q^2 \lesssim 80$ GeV^2 the low x_p data turn over and fall with decreasing Q^2. In a similar way to the shortfall in the mean charged multiplicity in this region, this behaviour is attributable to mass effects becoming important at low Q^2, exacerbated by the presence of interactions which do not contribute to e^+e^- annihilation and particularly to the BGF process which dominates DIS at low x.

Bins in the same Q^2 range but different x coincide within errors, although the bin with the lower x range systematically lies below that at higher x. This is consistent with the observation that the boson-gluon fusion interaction, whose cross-section falls with increasing x, leads to a lower final state charged multiplicity in the current region than the other interactions which contribute to the DIS cross-section. Henceforth, for clarity, where there are bins defined with the same range in Q but different ranges in x, only the bin for the higher x range will be shown.

ZEUS 1994-97 Preliminary
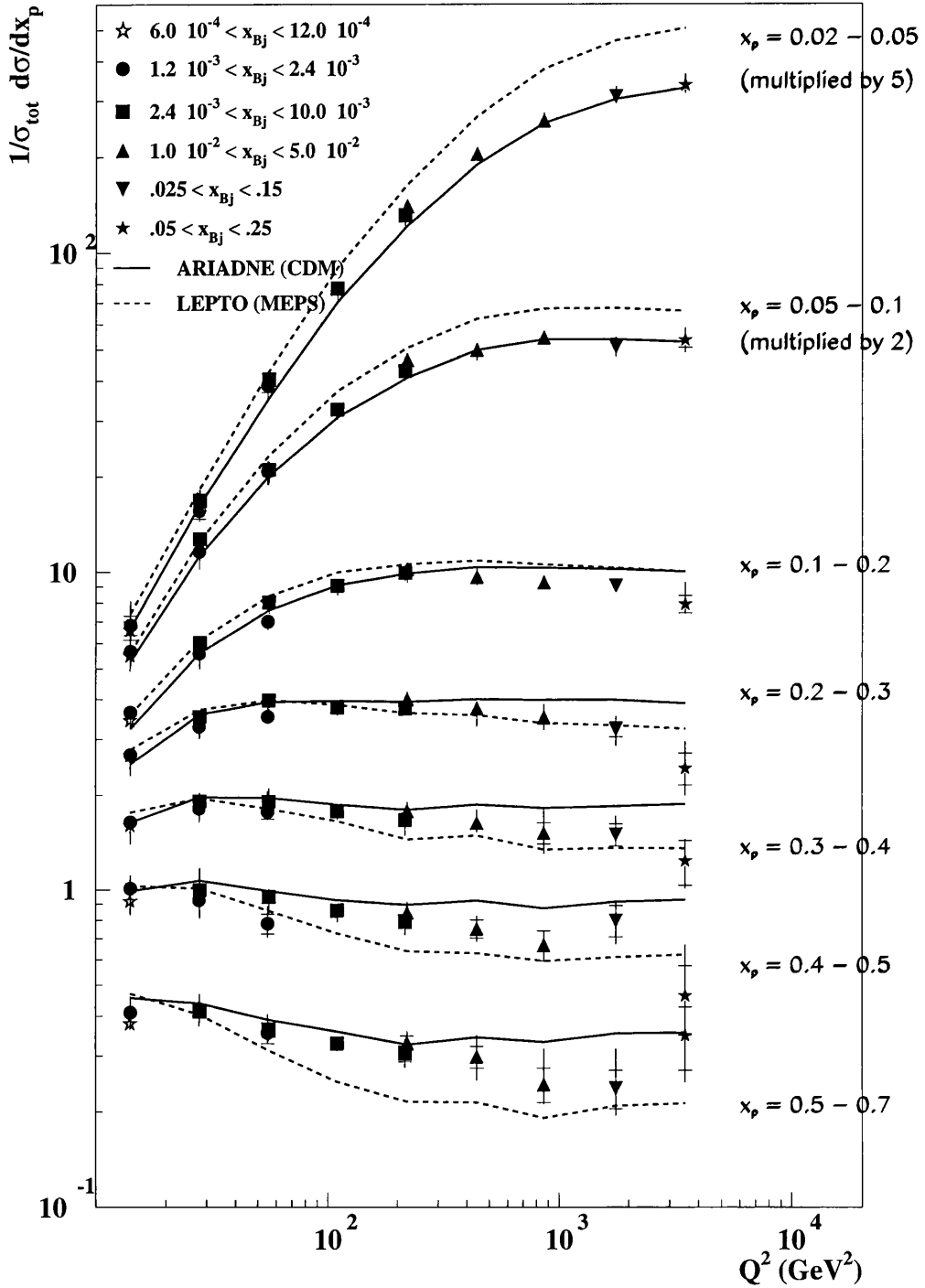
Figure 8.7: The single particle inclusive cross-section, $1/\sigma_{tot} d\sigma/dx_p$, as a function of Q^2. The inner error bars denote the statistical errors, the outer error bars show the statistical and systematic errors combined in quadrature.

The data are also compared with two leading order Monte Carlos: ARIADNE and LEPTO. No tuning of parameters to improve the agreement with the data was performed. ARIADNE describes the ZEUS data well over the full range of x and Q^2, whereas LEPTO overestimates the low x_p contribution and underestimates the high x_p cross-section. Neither Monte Carlo models the Q^2 dependence at large x_p accurately.

In order to highlight the scaling violation effect, figure 8.8 shows the ratios of x_p distributions measured at successively increasing values of $< Q^2 >$ (bins 6, 7, 8, 9, 10) to the distribution in bin 5 ($< Q^2 > = 28$ GeV^2). The ratio takes values between ≥ 1 for $x_p < 0.2$, and $\lesssim 0.8$ for $x_p > 0.5$. This deviation from the horizontal is to first order proportional to α_s, so that each data point yields an independent measurement of α_s. The data clearly establish negative scaling violations at large x_p.
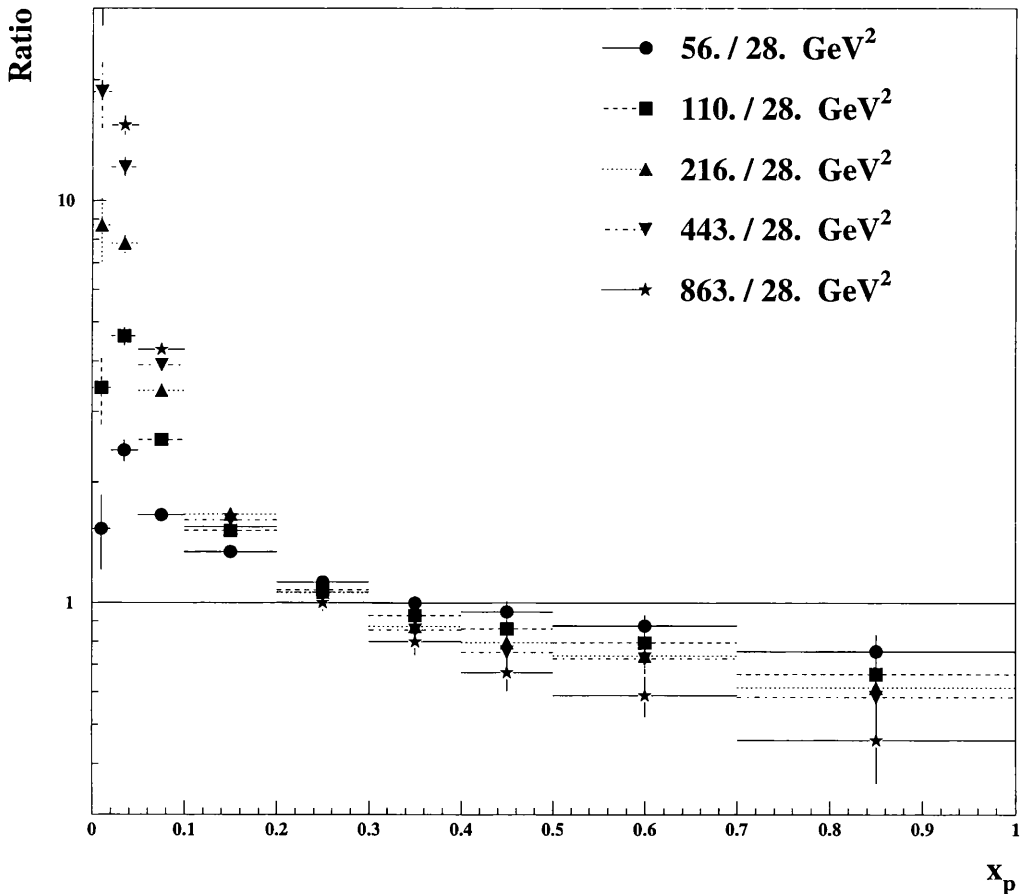
Figure 8.8: Ratios of x_p distributions in successively increasing Q^2 bins.

Figure 8.9 compares the ZEUS inclusive scaled momentum cross-section with data published by e^+e^- annihilation experiments at $Q^2 = s_{e^+e^-}$. The e^+e^- data included the decay products of K_S^0 and Λ particles; the points shown in these figures have been corrected for such decay products using JETSET 7.3 Monte Carlo tuned to DELPHI data, where the correction was generally of the order of 8%. The e^+e^- data have also been scaled by 1/2, since such interactions produce a q and a $\bar{q}$, compared with a single scattered quark in DIS. The ZEUS data have been measured over a range of Q^2 that overlaps well into the higher Q^2 region measured by these other experiments. There is good agreement between the data for $Q^2 \gtrsim 80$ GeV^2 and $x_p \gtrsim 0.3$. The ZEUS data lie beneath the e^+e^- data for $x_p \lesssim 0.3$.

It has been suggested [72] that this discrepancy is a result of the differing flavour contributions to the fragmentation processes, and particularly points to sensitivity to the strange quark contribution to the fragmentation. Flavour production in e^+e^- annihilation above threshold is democratic, whereas DIS is naturally biased towards the light quarks (u, d) found in the proton. The production of strange quarks in DIS is suppressed by ~ 0.2 with respect to that of light quarks. Parametrisations of the pion fragmentation functions for different flavours are compared in figure 8.10: the parametrisation for s quarks is significantly softer for $x_p \lesssim 0.3$ than that for u, d quarks.
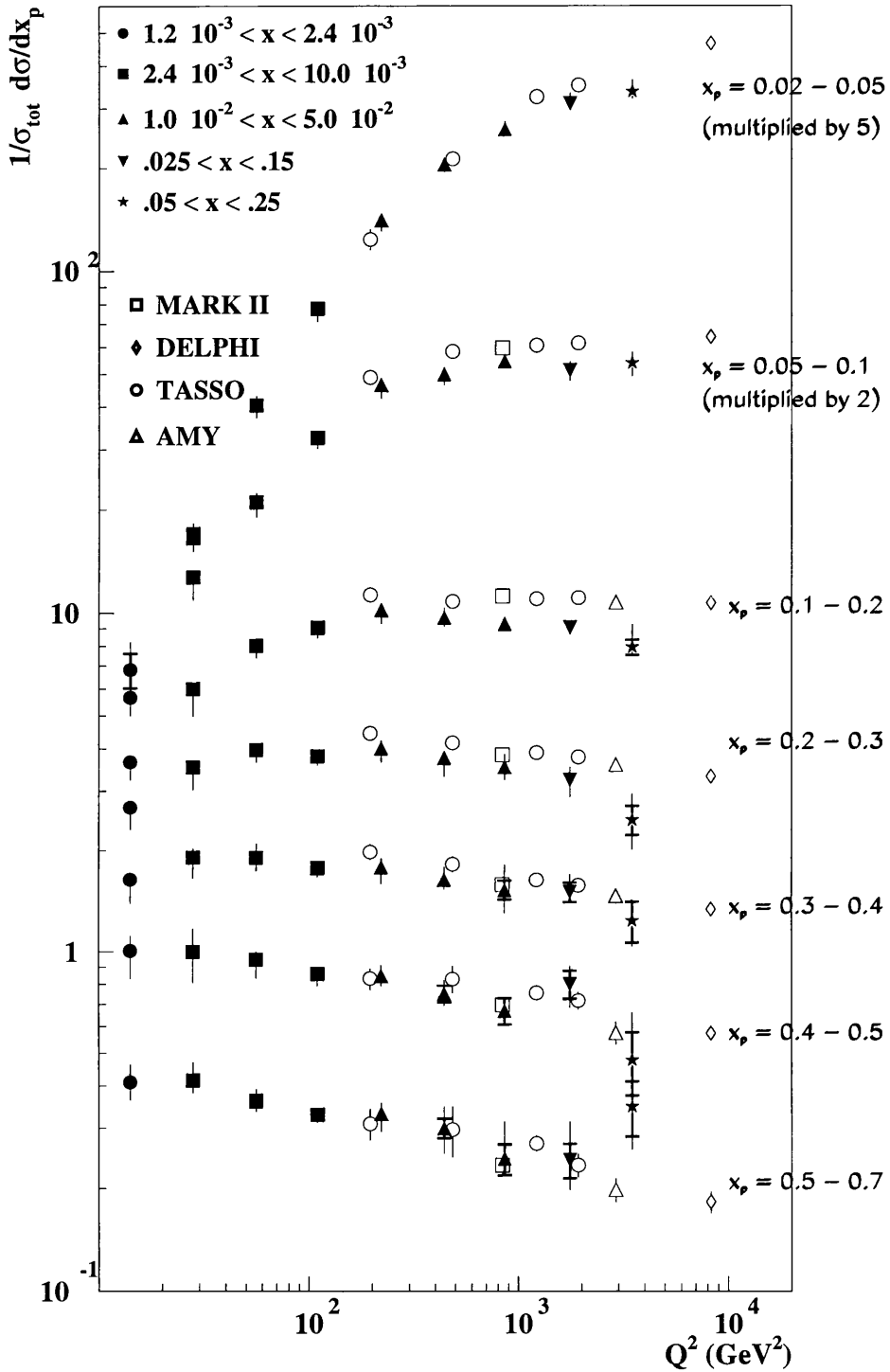
Figure 8.9: $1/\sigma_{tot}\,d\sigma/dx_p$ measured in the current region of the Breit frame in DIS at HERA, compared with data from e^+e^- annihilation experiments.
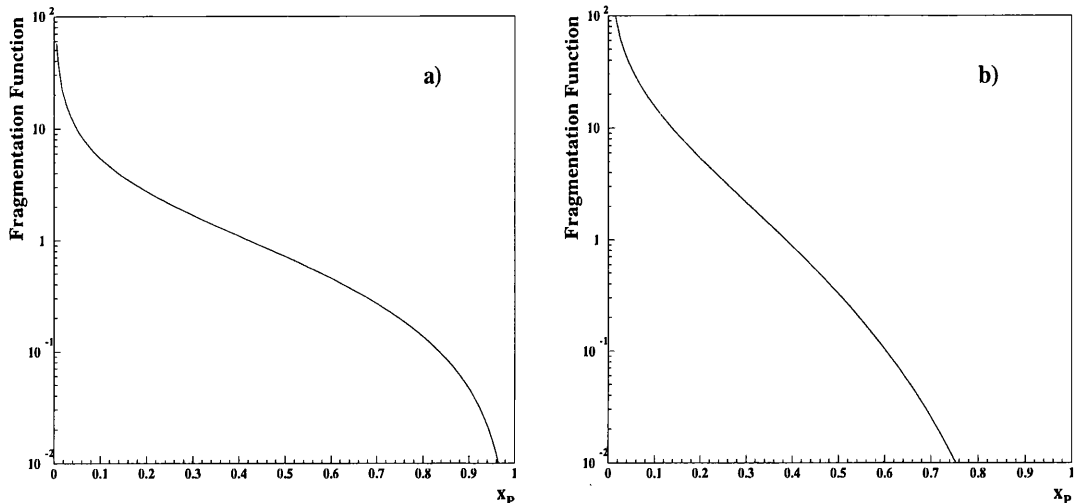
Figure 8.10: NLO parametrisations of the charged pion fragmentation functions: a) NLO parametrisation of the fragmentation function for $u, d \rightarrow \pi^{\pm}$; b) NLO parametrisation of the fragmentation function for $s \rightarrow \pi^{\pm}$.

8.3.1 Comparison with NLO Theory

In order to make a Next-to-Leading order prescription for the inclusive momentum cross-section $1/\sigma_{tot} \, d\sigma/dx_p$, each component of the convolution $\sigma \; = \; f \; \otimes \; \hat{\sigma} \; \otimes \; \mathcal{D}$ must be known to NLO level. A recent recalculation of the one-particle inclusive process in deep inelastic lepton-nucleon scattering has been implemented in the program CYCLOPS [21]. The program was used in conjunction with the MRS A$'$ parton density functions and NLO fragmentation functions fitted to e^+e^- data in references [17, 18] (with $\Lambda^4_{\overline{MS}} \approx 350$ MeV) to obtain a fully NLO calculation of the inclusive charged particle cross-section.

In figure 8.11 the ZEUS data are compared with the results of this calculation in the region $Q^2 > 80$ GeV^2 and $x_p > 0.1$ - where the theory is expected to be trustworthy. The calculation describes the data exceedingly well. Since the NLO theory uses fragmentation functions obtained from e^+e^- data, this agreement gives convincing support to the concept of the universality of fragmentation functions. Discontinuities in the lines arise from different results for different x bins at the same Q^2.
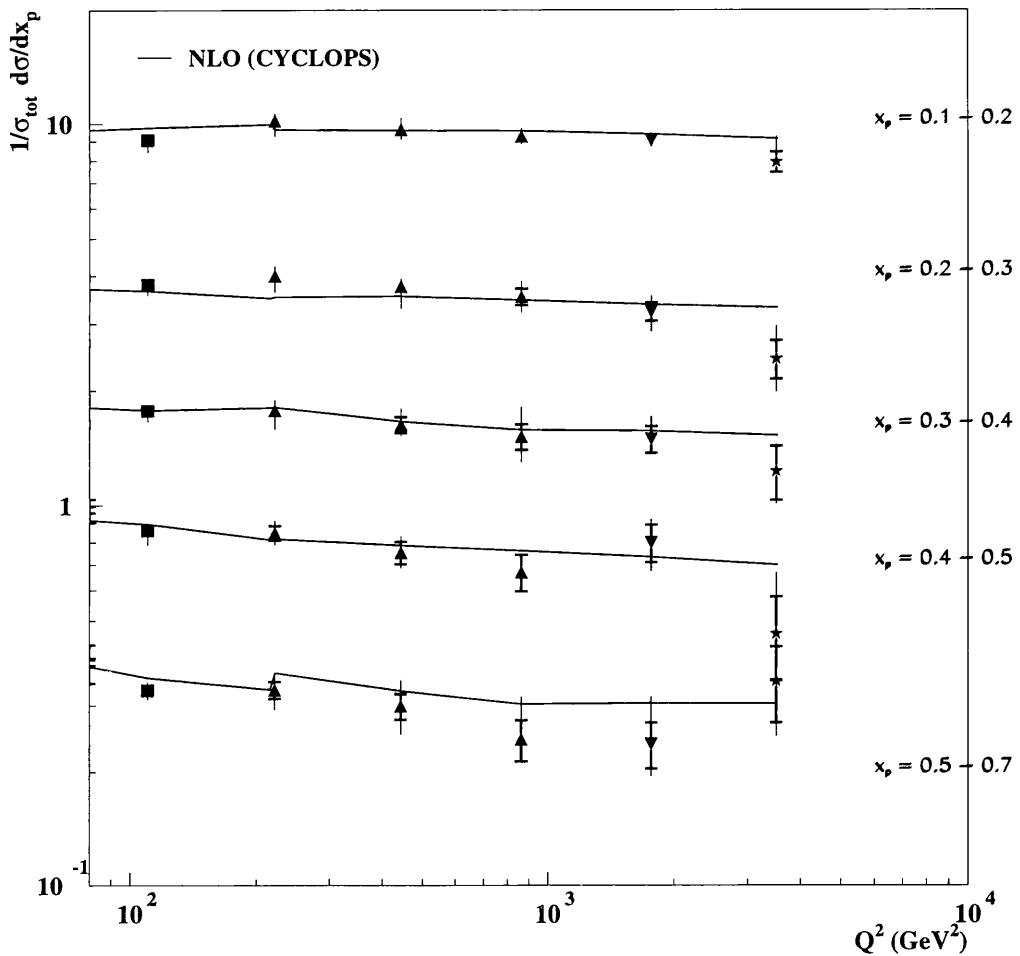
Figure 8.11: x_p distributions compared with NLO theory for $Q^2 > 80$ GeV^2.

Figure 8.12 shows the data and NLO calculation across the entire Q^2 and x_p range. The limitations of the theoretical calculation are immediately obvious: at low x_p and low Q^2 the NLO calculation over-estimates the data. This effect can be seen as a result of the failure of the fragmentation function formalism for hadrons produced at large rapidity with respect to the parent parton. If one considers the leading-order process, where a single parton fragments into the hadronic final state, the fragmentation function picture is only valid if the hadron is produced close in rapidity to the parent parton. This can be translated into a lower bound on x_p as a function of Q^2, which describes well the region in figure 8.12 where the theory diverges from the data (see reference

[73] for a more detailed exposition).

In principle, implementing CYCLOPS with PDFs and sets of fragmentation functions derived at a range of different values of $\Lambda_{\overline{MS}}^4$ - and consistent values of $\Lambda_{\overline{MS}}^4$ throughout the calculation - would provide sufficient data to interpolate and extract the value of $\Lambda_{\overline{MS}}^4$ which gave the best description of the data.

New fragmentation functions were fitted to e^+e^- data over a range of values of $\Lambda_{\overline{MS}}^4$ between 150 MeV and 400 MeV [19]. Figure 8.13 shows the results obtained by implementing CYCLOPS with the newly fitted fragmentation functions over the full range of $\Lambda_{\overline{MS}}^4$. It is apparent that the new calculation fails to reproduce the data successfully. The discrepancies arise from a series of changes which were adopted in the approach to fitting the data for these new fits. Where references [17, 18] presented results obtained by performing fits to exclusive $K^\pm$ and $\pi^\pm$ distributions and the results were combined within CYCLOPS to predict the inclusive final hadronic state, the more recent fits presented in [19] had instead been carried out over inclusive charged particle distributions (thus including the fragmentation functions for, for instance, p ($\bar{p}$) as well). This update to fitting over all charged hadrons entailed an alteration in the treatment of the light quarks, since separate constraints could no longer be employed in the treatments of u, d quarks and of s quarks. Thus no attempt was made in the new set of fragmentation functions to distinguish between the u, d and s contributions.

The changes in the approach to fitting the fragmentation functions have led to an increase in the level of the new fragmentation functions relative to the old version, so that the new calculations cannot be used directly to test the sensitivity of the data to α_s. However, the difference between the two lines for $\Lambda_{\overline{MS}}^4 = 250$ and 400 MeV can be taken to indicate the level of sensitivity required in order to determine α_s. Although the requirement that a calculation at a particular value of $\Lambda_{\overline{MS}}^4$ must be consistent with all (x, Q^2, x_p) points is a helpful constraint, it is clear from the figure that a high level of accuracy will be required from the data if they are to discriminate between NLO predictions at different values of $\Lambda_{\overline{MS}}^4$.

8.4 Summary

Fragmentation functions have been measured for DIS in the Breit frame of reference at HERA. The data are well modelled by LO Monte Carlos. There is good agreement with NLO calculations within the region of validity of the theory. When the data are compared with results from e^+e^- annihilation experiments, discrepancies are seen for $x_p \lesssim 0.3$.

Measurements have been made of the fragmentation variable $\ln\left(\frac{1}{x_p}\right)$. The distributions are well described by the MLLA - supporting the concept of coherence in QCD cascades - and reveal similar evolution with energy as that shown by results from e^+e^- experiments.

ZEUS 1994-97 Preliminary
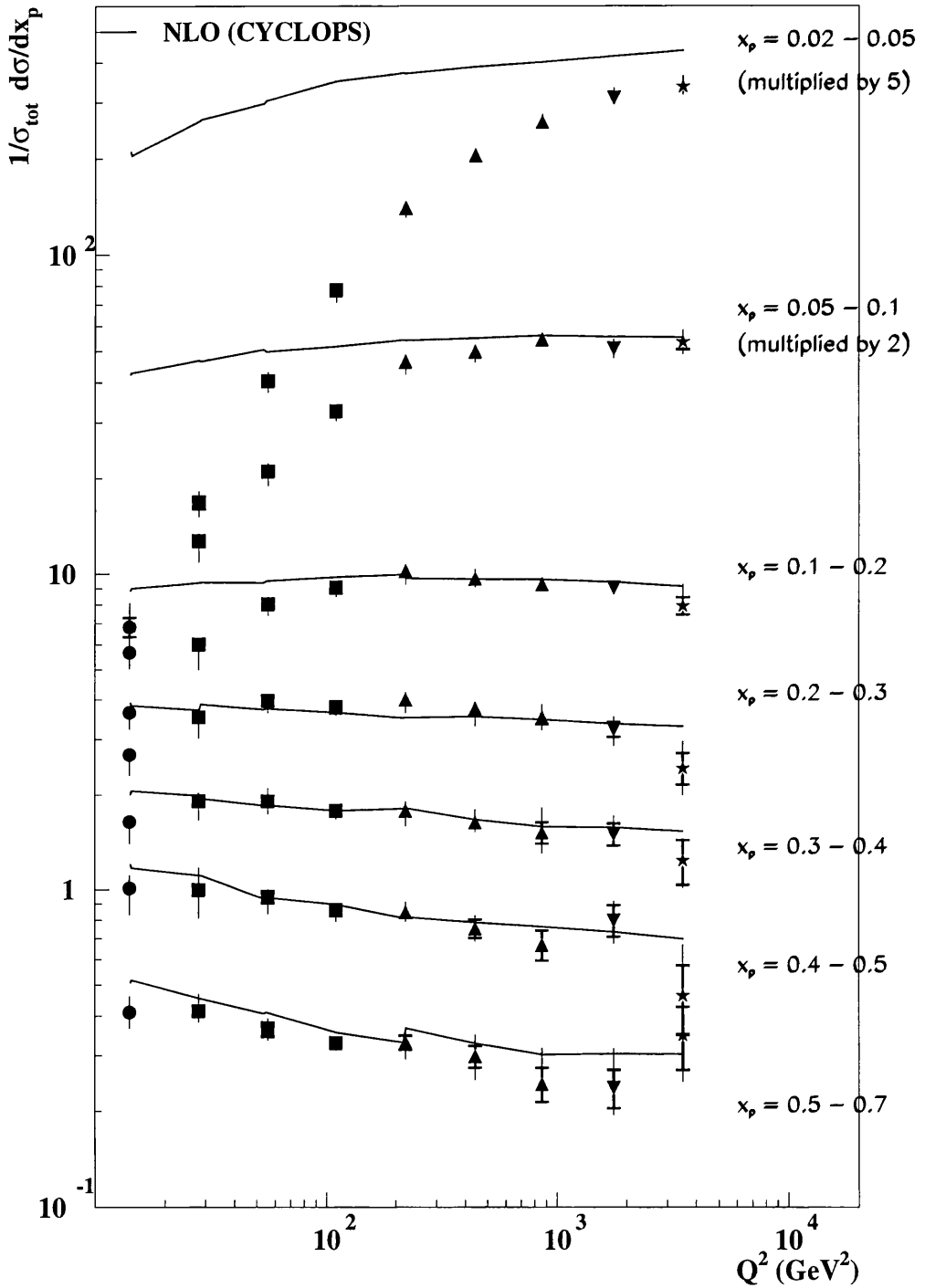
Figure 8.12: x_p distributions compared with NLO theory across the full kinematic range.
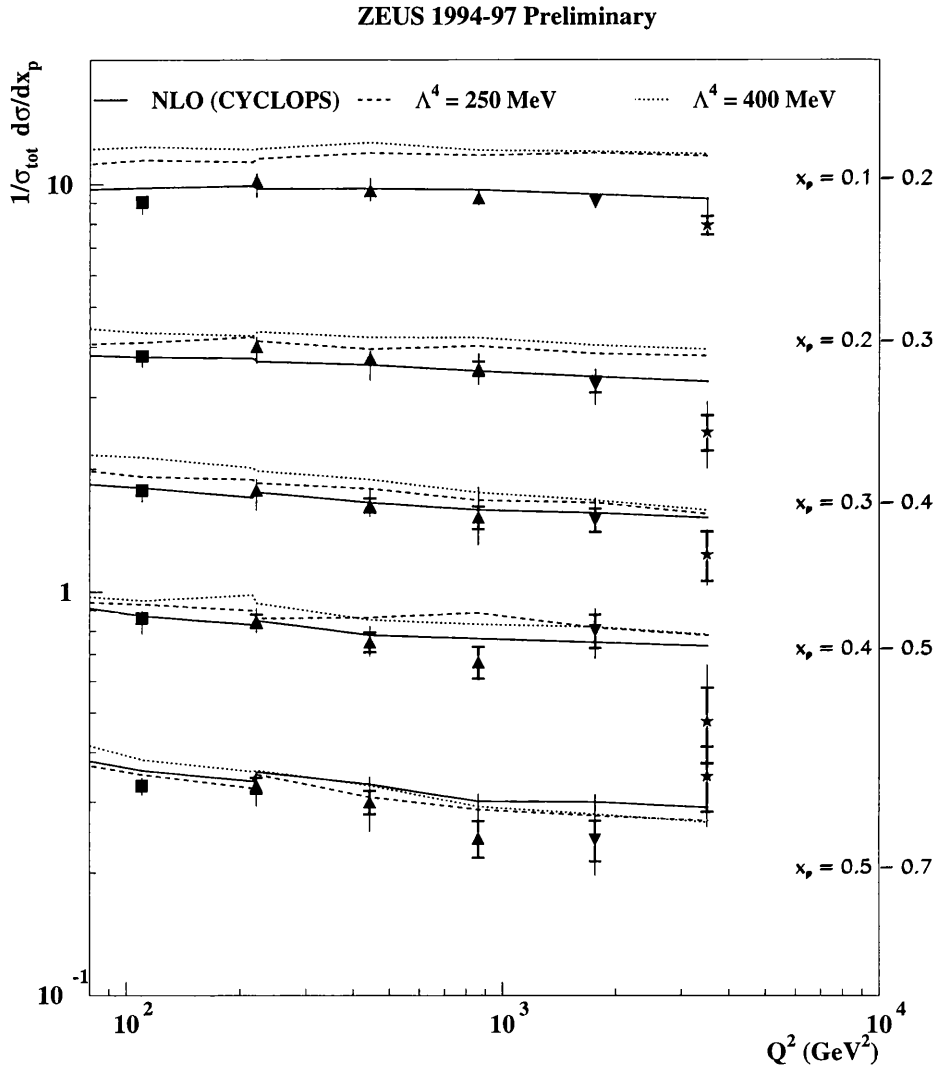
Figure 8.13: x_p distributions compared with new NLO calculation at different values of Λ. The full line denotes the calculation with the original fragmentation function, while the dashed and dotted lines represent the reuslts of implementing the new fragmentation functions at $\Lambda^4_{\overline{MS}} = 250$ and 400 MeV, respectively.

Chapter 9

Conclusions

The fragmentation of quarks and gluons into charged particles has been studied in the current region of the Breit frame in DIS. The fragmentation variables x_p and $\ln\left(\frac{1}{x_p}\right)$ have been measured - incorporating data taken during four years of ZEUS running - as a function of Q^2 and x in the ranges $10 < Q^2 < 5120$ GeV^2, $0.6 \ 10^{-3} < x < 0.25$ and $0.02 < x_p < 0.7$.

The $\ln\left(\frac{1}{x_p}\right)$ spectra have been shown to be well described by the Modified Leading Log Approximation. The evolution with Q^2 of the distributions has been investigated and the results agree broadly with e^+e^- data and with the predictions of the MLLA. There are discrepancies in the form of the evolution which may indicate the effects of higher order corrections at low Q^2.

The development of the charged multiplicity with Q^2 has been examined and compared with e^+e^- data and with LO Monte Carlos. The ZEUS data agree well with e^+e^- results for $50 \lesssim Q^2 \lesssim 1000$ GeV^2.

Evidence has been found for scaling violations in the single particle inclusive distributions, $\frac{1}{\sigma_{tot}}\frac{d\sigma}{dx_p}$, as a function of Q^2. The values of Q^2 measured overlap with the centre-of-mass energies used in e^+e^- annihilation experiments: within this region of overlap the data agree well for $x_p \gtrsim 0.3$. For $x_p \lesssim 0.3$ the ZEUS data fall under the e^+e^- data. This is believed to be the result of sensitivity to strangeness production and fragmentation. The data have been successfully described by NLO QCD calculations, and provide convincing support for the concept of the universality of fragmentation.

Appendix A

Data Preselection

The Third Level Trigger has a loose selection procedure to separate interesting events from events regarded as background, such as interactions resulting from beam-gas or cosmic rays. Events selected by the TLT are written to a Data Summary Tape (DST) and passed to offline reconstruction where they must pass even stricter filters. The events used in this analysis were chosen to satisfy a specific DST bit, bit 18, which required:

scattered positron found by

SINISTRA with $E'_e > 10$ GeV

vertex found with $z < 100$ cm

boxcut at 13 cm   number of tracks ≥ 1

$E'_e > 5$ GeV   .or. $|t_R| < 4$

$y_{JB} > 0.$ $y_{JB} > 0.04$

$y_e > 0.95$

$Q^2_{DA} > 10$ GeV^2

boxcut in the calorimeter at 16 cm.

Also, algorithms were applied to discard events due to halo muons, QED Comptons and cosmic muons, and events in which there were sparks in calorimeter cells.

The 1997 data - which were used to supplement the high Q^2 data sample - were preselected using a high Q^2 DIS DST bit, bit 12, defined as:

$Q^2_{DA} > 80$ GeV^2 .and. $y_e < 0.95$

.and. scattered positron found with $E'_e > 5$ GeV

Appendix B

Treatment of statistical errors

In order to correct the raw data distributions, bin-by-bin correction factors were defined, for instance, for each x_p bin in a (x, Q^2) bin using distributions obtained from Monte Carlo simulations as:

$$F(x_p) = \frac{1}{N_{\text{gen}}} \left(\frac{dn}{dx_p}\right)_{\text{gen}} \bigg/ \frac{1}{N_{\text{obs}}} \left(\frac{dn}{dx_p}\right)_{\text{obs}}$$

where $\left(\frac{dn}{dx_p}\right)_{\text{gen(obs)}}$ was the number of Monte Carlo events generated (observed) in a particular bin of x_p, x and Q^2; and N_{gen} (N_{obs}) was the number of generated (observed) Monte Carlo events falling into the particular (x, Q^2) interval.

The (x_p, x, Q^2) bin in which a particle is reconstructed is not independent of the bin in which it was generated, so the errors in the expression for the correction factor cannot be calculated as though for two statistically independent distributions.

If the correction factor is expressed as $F = \frac{a_i}{b_i}$, and it is assumed that the number of events generated in a particular (x_p, x, Q^2) bin i is a result of the combination of two *STATISTICALLY INDEPENDENT* distributions, so that

1. the generated distribution can be written as $a_i = C + D$, where C is the number of events generated *and* reconstructed in bin i, and D is the number of events generated in bin i which after reconstruction are found in bin j, and

2. the number of events reconstructed in bin i is a convolution of the number of events generated and reconstructed in bin i (C) with the number of events

154

generated in bin j but reconstructed in bin i (E), so that the observed distribution can be written as $b_i = C + E$.

With these assumptions and C,D,E statistically independent, the error in the correction factor $F = \frac{C+D}{C+E}$ can be shown to be :

$$\Delta(F) = \sqrt{\frac{E^2(C+D) + D^2(C+E) + C^2(D+E) + 2CDE}{(E+C)^4}}$$

If we consider the limit of this expression as $D \rightarrow 0$ then it gives the normal binomial result expected from a straightforward efficiency. In the limit as $C \rightarrow 0$, the expression for the error becomes that expected from a ratio of statistically independent numbers. If the binning is done properly then D and E should always be small and the binomial error is a very good approximation.

Appendix C

Contribution to Chicago DIS97 Conference

Fragmentation Functions at ZEUS

Jane Bromley

on behalf of the ZEUS collaboration

The scaled momentum spectra of final state charged hadrons produced in Deep Inelastic Scattering in the ranges $10 < Q^2 < 1280$ GeV^2 and $6 . 10^{-4} < x_{\mathrm{Bjorken}} < 5 . 10^{-2}$ have been measured in the current region of the Breit frame using the ZEUS detector. The evolution with Q^2 of the scaled momentum, $x_p = 2p^{\mathrm{Breit}}/Q$, has been investigated and preliminary results are presented which show evidence for scaling violations and support for the universality of quark fragmentation.

Introduction

Studies of scaling violations in structure functions in Deep Inelastic Scattering (DIS) have helped to establish Quantum Chromodynamics (QCD) as the theory of strong interactions and have led to measurements of the strong coupling constant, α_s. Similar scaling violations are predicted in the fragmentation functions of quarks and gluons [1].

156

The fragmentation function $D^h(x_p, Q^2)$ for a parton represents the probability that it fragments to form a hadron h carrying a fraction x_p of the parton's momentum. As with structure functions, they cannot be calculated in perturbative QCD but can be evolved as a function of the appropriate energy scale.

In DIS and e^+e^- annihilation hadroproduction experiments, as the energy scale increases, α_s decreases and the phase space for gluon radiation increases, so that the primary quarks in an interaction will tend to lose more of their energy. Therefore we expect the x_p spectrum, where $x_p = 2p/\sqrt{s}$ and $\sqrt{s}$ is the centre-of-mass energy, to change: the high momentum end will be depopulated and the radiated gluons will tend to populate the low x_p region. Thus, if x_p is measured as a function of centre-of-mass energy, we expect to see a scaling violation due to QCD effects.

Such studies have been performed at LEP [2, 3] where, by combining lower energy data from PETRA, scaling violations in the density of single particles, $\frac{1}{\sigma_{tot}}\frac{d\sigma}{dx_p}$ have been fitted as a function of $\sqrt{s}$, to extract a value of α_s. In DIS the single particle density is a convolution of the hard scattering cross-section with a parton density and a fragmentation function: $\sigma = \sigma_{\text{hard}} \otimes f \otimes D$. The strong coupling constant enters through each of these components.

C.1   The Breit Frame

The intention of this analysis is to compare fragmentation functions measured in DIS at HERA with those measured by e^+e^- experiments: in order to do so it is necessary to boost and rotate DIS events to the Breit frame. The Breit frame [26] is defined as the frame in which the exchanged boson is completely spacelike. Its velocity with respect to the laboratory frame is given by $\vec{\beta} = (\vec{q} + 2x\vec{P})/(q_0 + 2xP_0)$, where $(q_0, \vec{q})$ and $(P_0, \vec{P})$ are the 4-momenta of the exchanged boson and the incident proton beam respectively. DIS events are boosted and then rotated so that the virtual photon is along the negative z axis and the plane of the incoming and outgoing positron contains the $\phi = 0$ direction - this maximises the separation of the outgoing parton from the incoming parton and the proton remnant. The region of $z < 0$ in this frame, containing the outgoing quark, is defined as the current region while the target region, defined as the region $z > 0$,

contains the scattered positron and proton remnant. In the Quark Parton Model the outgoing struck quark carries momentum $Q/2$, compared with e^+e^- annihilation where there are two outgoing quarks, each with momentum $Q/2 \equiv \sqrt{s}/2$. Hence the current region of the Breit frame can be taken to be analogous to one hemisphere of an e^+e^- annihilation event.

C.2 The Data

The data presented here were taken with the ZEUS detector at HERA in 1994, during which period HERA operated with bunches of 820 GeV protons and 27.5 GeV positrons. The ZEUS detector has been described elsewhere [31]. DIS data were selected. The kinematic variables x, Q^2 and $\vec{\beta}$ were reconstructed using the Double Angle method [44].

The sizes of the bins in x and Q^2 were consistent with the measured resolutions and restricted to regions of high acceptance for tracks in the current region. They were based on the bins chosen in [48]. Tracks associated with the primary vertex and satisfying $p_T > 150$ MeV and $|\eta| < 1.75$, where η is the pseudorapidity measured relative to the proton beam direction, were selected and boosted to the Breit frame. The scaled momentum, $x_p = 2p^{\text{Breit}}/Q$, of those reconstructed in the current region was then measured.

The data were corrected for the effects of the trigger and event selection cuts; event migration between (x, Q^2) bins; QED radiative effects; track reconstruction efficiency; track selection cuts in p_T and η; track migration between current and target regions; and for the decay products of K_S^0 and Λ decays being misassigned to the primary vertex. The most significant contribution to the resolution on the measurement of x_p was found to be from uncertainty in the reconstruction of the boost vector, $\vec{\beta}$.

C.3 Results

The corrected scaled momentum distributions (with statistical errors only) are shown in figure C.1, overlaid with the distributions from the ARIADNE Monte Carlo [57].

The Monte Carlo reproduces the data well in all bins of x, Q^2 and x_p.

In the region of low x and Q^2 the distributions peak at $x_p \approx 0.15$; as Q^2 increases this peak disappears and the data fall off sharply from $x_p = 0.02$. Scaling violations can be seen, as predicted, in the gradual steepening of the gradients of the distributions as Q^2 increases. To show this more clearly, in figure C.2 the data are plotted in fixed bins of x_p as a function of Q^2. Scaling violations appear at high Q^2 and high x_p as a negative slope with increasing Q^2. The turnover observed in the ZEUS data at low x_p and low Q^2 can be attributed to depopulation of the current region by processes not present in e^+e^- interactions (e.g. boson-gluon fusion). The ZEUS data are compared with data from e^+e^- experiments (divided by a factor 2) and with a next-to-leading-order calculation, CYCLOPS [21]. The e^+e^- data points are taken from the aforementioned LEP study of scaling violations in fragmentation functions and have been corrected for the decays of K_S^0 and Λ. There is good agreement with the ZEUS data. The NLO calculation combines a full next-to-leading order matrix element with the MRSA' parton densities [51] and NLO fragmentation functions derived by Binnewies et al. from fits to e^+e^- data [17]. There is good agreement with the ZEUS data for $Q^2 \gtrsim 80$ GeV^2; below this value there are large theoretical uncertainties.

C.4   Conclusions

The scaled momentum distributions of final state charged hadrons have been measured in the current region of the Breit frame over a wide range of values of Q^2. The ZEUS data are consistent with the predictions of scaling violations at high Q^2 and high x_p. The results are in good agreement with results from e^+e^- experiments and also with a NLO calculation using input fragmentation functions from e^+e^- data, indicating strong support for the concept of the universality of quark fragmentation.

Acknowledgments
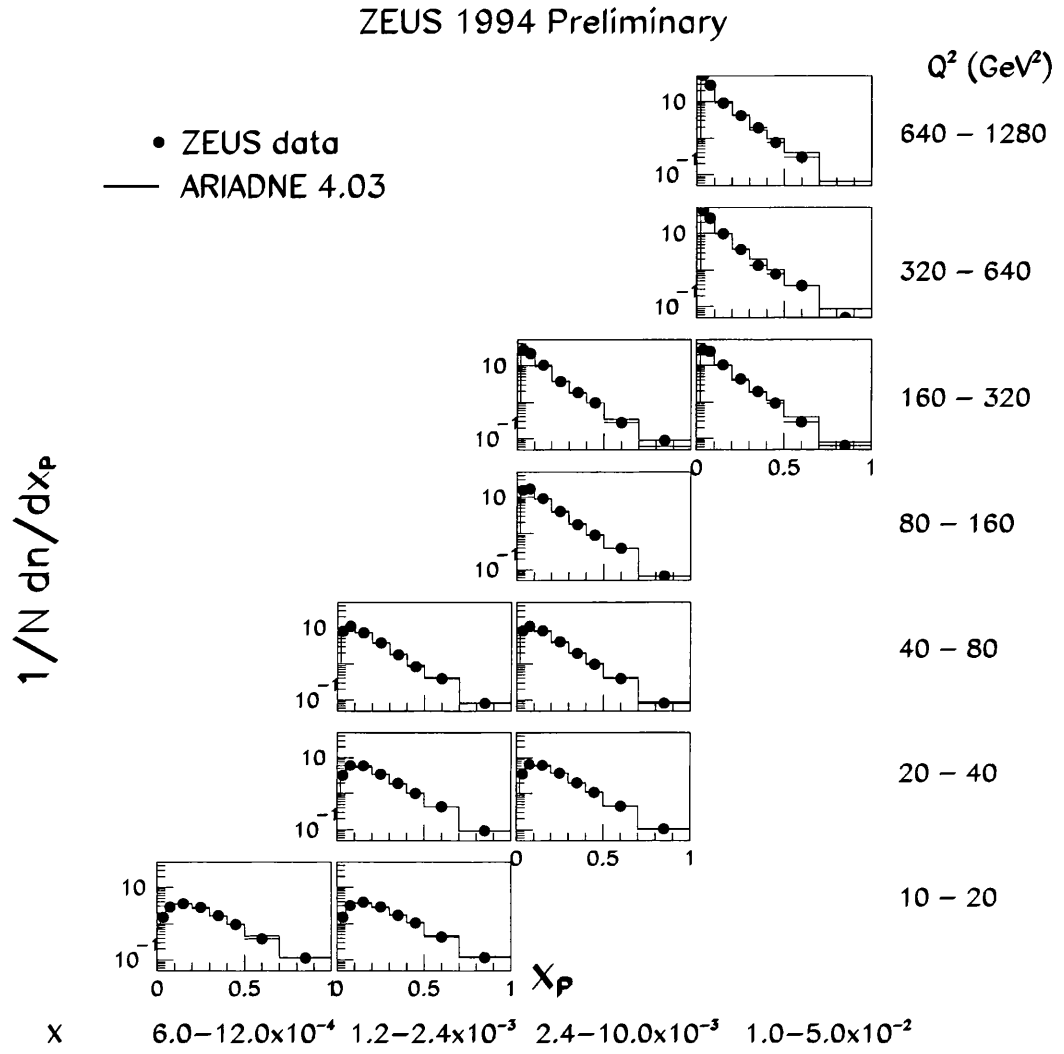
Figure C.1: The corrected scaled momentum distributions from ZEUS 1994 data compared with the generated distributions from the Monte Carlo (ARIADNE 4.03). Statistical errors only are shown.
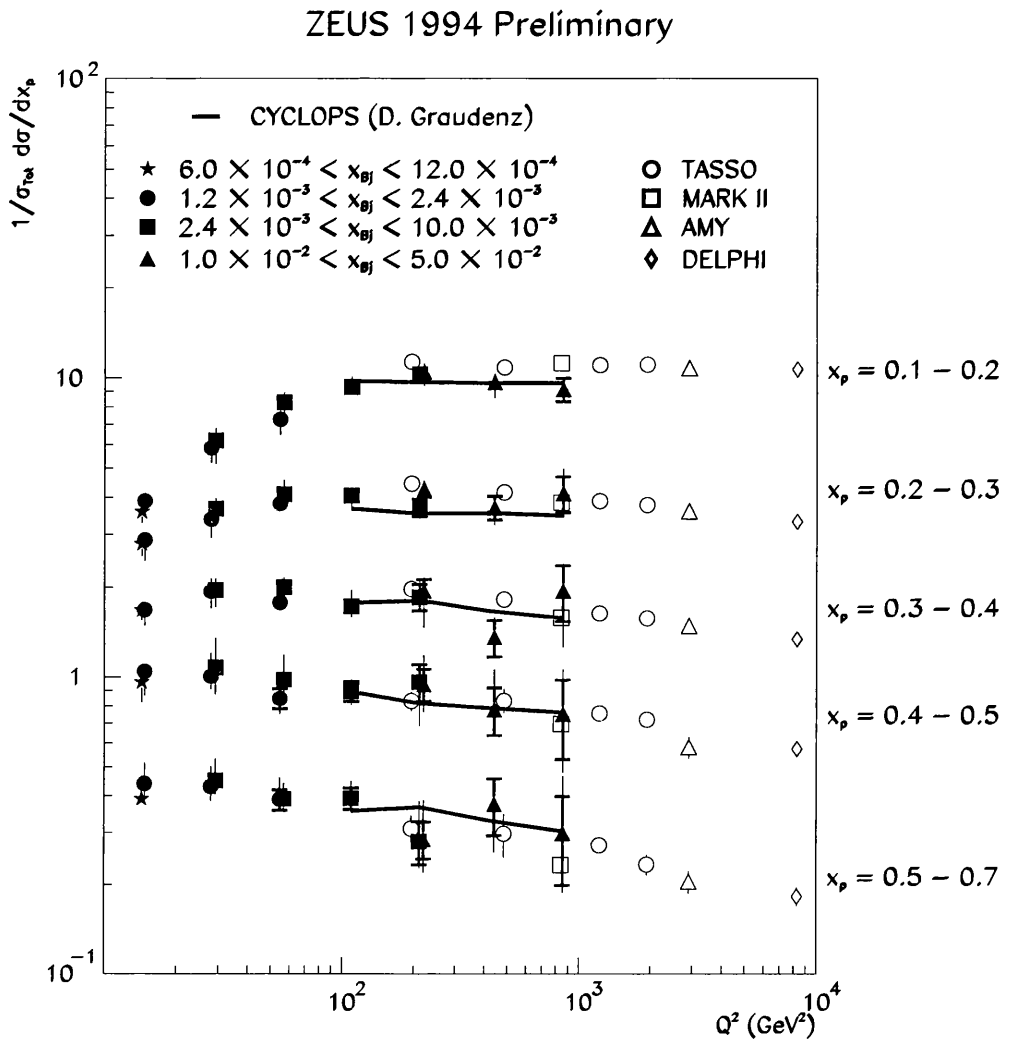
Figure C.2: The inclusive charged particle distribution, $1/\sigma_{tot}\, d\sigma/dx_p$, in the current region of the Breit frame. The filled points are ZEUS data, and the statistical (thick error bars) and combined statistical and systematic (thin error bars) errors are shown. The open points represent the data from e^+e^- experiments corrected for contributions from K_S^0 and Λ decays. The lines show the NLO predictions.

References

[1] P. Nason and B. Webber, *Nucl. Phys.* **B 421** (1994) 473.

[2] ALEPH Collaboration, *Phys. Lett.* **B 357** (1995) 487.

[3] DELPHI Collaboration, *Phys. Lett.* **B 311** (1993) 408.

[4] DELPHI Collaboration, CERN–PPE/96–185.

[5] ZEUS Collaboration, *Phys. Lett.* **B 414** (1997) 428.

[6] F. Halzen and A.D. Martin, *Quarks and Leptons*, Wiley, 1984.

[7] S. L. Glashow, *Nucl. Phys.* (1961) 579.

[8] A. Salam, *Weak and electromagnetic interactions*, Proceedings of the Nobel Symposium held 1968 at Lerum.

[9] S. Weinberg, *Phys. Rev. Lett.* **19** (1967) 1264.

[10] Friedman, Kendal and Taylor, *Rev. Mod. Phys.* **3** (1991) 63.

[11] F. Lehner, *Measurement and QCD Analysis of the Proton Structure Function*, Talk given at the Lake Louise Winter Institute, 15 - 21 Feb. 1998.

[12] Yu. Dokshitzer, *Sov. Phys. JETP* **46** (1977) 641;
V.N. Gribov and L.N. Lipatov, *Sov. J. Nucl. Phys.* **15** (1972) 438, 675;
L.N. Lipatov, *Sov. J. Nucl. Phys.* **20** (1975) 95.

[13] G. Altarelli and G. Parisi, *Nucl. Phys.* **B 126** (1977) 298.

[14] A.M. Cooper-Sarkar, R.C.E Devenish and A. De Roeck, DESY 97–226.

[15] R.K Ellis, W.J Stirling and B.R. Webber, *QCD and Collider Physics*, C.U.P., 1996.

[16] J.C. Collins, D. E. Soper and G. Sterman, *Nucl. Phys.* **B 162** (1985) 104.

[17] J. Binnewies, B.A. Kniehl and G. Kramer, *Zeit. Phys.* **C 65** (1995) 471.

[18] J. Binnewies, B.A. Kniehl and G. Kramer, *Phys. Rev.* **D 52** (1995) 4947.

[19] J. Binnewies, *Fragmentation Functions in Next-To-Leading Order QCD*, PhD thesis, University of Hamburg, 1997.

[20] R. Baier, J. Engels and B. Petersson, *Zeit. Phys.* **C 2** (1979) 265.

[21] D. Graudenz, CERN–TH/96–52.

[22] A.E. Chudakov, *Izv. Akad. Nauk. SSSR, Ser. Fiz.* **19** (1955) 650.

[23] Yu.L. Dokshitzer, V.A. Khoze, A.H. Mueller, S.I. Troyan, *Basics of Perturbative QCD*, Editions Frontières, 1991.

[24] Yu. L. Dokshitzer and S. I. Troyan, *Proceedings of the 19th Winter School of the LNPI*, Volume 1 (1984) 144;
Ya. I. Azimov, Yu. L. Dokshitzer, V. A. Khoze and S. I. Troyan, *Zeit. Phys.* **C 27** (1985) 65;
Ya. I. Azimov, Yu. L. Dokshitzer, V. A. Khoze and S. I. Troyan, *Zeit. Phys.* **C 31** (1986) 213.

[25] V.A Khoze and W. Ochs, *Int. J. Mod. Phys.* **A 12** (1997) 2949.

[26] R.P. Feynman, *Photon-Hadron Interactions*, Benjamin N.Y., 1972.

[27] L.V.Gribov, Yu. L. Dokshitzer, S.I.Troyan and V. A. Khoze, *Sov. Phys. JETP* **68** (1988) 1303.

[28] S. V. Chekanov, ZEUS 98–024.

[29] J.G. Koerner, E. Mirkes and G.A. Schuler, *Int. J. Mod. Phys.* **A 4** (1989) 1781.

[30] ZEUS Collaboration, *Zeit. Phys.* **C 67** (1995) 81.

[31] ZEUS Collaboration, *The ZEUS Detector Status Report 1993*, DESY 1993.

[32] G.F. Hartner et al., *VCTRAK (3.06/20): Offline Output Information*, ZEUS–Note–96–013.

[33] P. Billoir and S. Qian, *Nucl. Instr. Meth.* **A 311** (1992) 139.

[34] H. Abramowicz, A. Caldwell and R. Sinkus, *Nucl. Instr. Meth.* **A 364** (1995) 508.

[35] Allan S. Wilson, *A Study of Neutral Kaons and Charged Particles in Photoproduced Jets at HERA*, PhD thesis, University of Glasgow, 1997.

[36] G. Blair, J.C. Giddings, A. Prinias, K. Prytz and K. Long, *Calibration of the CTD using the 1992 Autumn Data*, ZEUS–Note–92–122.

[37] K. Kleinknecht, *Detectors for Particle Detection.*

[38] S. Mengel, J.B. Lane and F. Corriveau, *The Magnetic Field in the ZEUS Central Tracking Region*, ZEUS–Note–92–098.

[39] J.B. Lane, private communication.

[40] R. Seifert, *Noise94 Routine*, ZEUS Phantom Library.

[41] S.M. Wang, *Study of Calorimeter Noise in the '95 Data*, ZEUS–Note–96–121.

[42] A. Savin, *Study of Calorimeter Noise in the 1996 Data*, ZEUS–Note–98–007.

[43] F. Jacquet and A. Blondel, *Proceedings of the Study of an ep facility for Europe*, Volume 79/48 (1979) 391.

[44] S. Bentvelsen and J. Engelen and P. Kooijman, *Proceedings of the 1991 Workshop on Physics at HERA*, Volume 1 (1991) 23.

[45] U. Bassler and G. Bernadi, *Nucl. Instr. Meth.* **A 361** (1995) 197.

[46] H1 Collaboration, *Nucl. Phys.* **B 407** (1993) 515.

[47] H1 Collaboration, *Nucl. Phys.* **B 439** (1995) 471.

[48] ZEUS Collaboration, *Measurement of Multiplicity and Momentum Spectra in the Current Region of the Breit Frame, Zeit. Phys.* **C 67** (1995) 93.

[49] V.A. Jamieson, *Measurement of Scaled Momentum Distributions in the Breit Frame at HERA using the ZEUS detector*, PhD thesis, University of Glasgow, 1994.

[50] A.D. Martin, R.G. Roberts and W.J. Stirling, *Phys. Rev.* **D 50** (1994) 6734.

[51] A.D. Martin, R.G. Roberts and W.J. Stirling, *Phys. Lett.* **B 354** (1995) 155.

[52] ZEUS Collaboration, *Zeit. Phys.* **C 65** (1995) 379.

[53] H1 Collaboration, *Nucl. Phys.* **B 407** (1993) 231.

[54] G. Ingelman, *Proceedings of the 1991 Workshop on Physics at HERA*, Volume 3 (1992) 1366.

[55] K. Charchuła, G. Schuler and H. Speisberger, *Computer Phys. Comm.* **81** (1994) 381.

[56] A. Kwiatkowski, H. Spiesberger and H.-J. Möhring, *Proceedings of the 1991 Workshop on Physics at HERA*, Volume 3 (1992) 1294.

[57] L. Lönnblad, *ARIADNE version 4.03 program and manual, Computer Phys. Comm.* **71** (1992) 15.

[58] ZEUS Collaboration, *Zeit. Phys.* **C 59** (1993) 231.

[59] ZEUS Collaboration, *Phys. Lett.* **B 338** (1994) 483.

[60] H. Jung, DESY 93–182.

[61] G. Marchesini et al., *Computer Phys. Comm.* **67** (1992) 465.

[62] R. Brun et al., *GEANT3*, CERN DD/EE/84-1 (1987).

[63] I.O. Skillicorn and N.H. Brook, ZEUS–Note–98-044.

[64] OPAL Collaboration, *Phys. Lett.* **B 247** (1990) 617.

[65] C.P. Fong and B.R. Webber, *Phys. Lett.* **B 229** (1989) 289.

[66] B. Webber, private communication.

[67] TASSO Collaboration, *Zeit. Phys.* **C 45** (1989) 193.

[68] PLUTO Collaboration, *Phys. Lett.* **B 95** (1980) 313.

[69] OPAL Collaboration, *Zeit. Phys.* **C 53** (1992) 539.

[70] MARK1 Collaboration, *Phys. Rev.* **D 26** (1986) 969.

[71] M. Derrick et al., *Phys. Lett.* **B 91** (1986) 470.

[72] G. Kramer, private communication.

[73] D. Graudenz, PSI–PR/97–20.